DISSERTATION

SUPER-RESOLUTION IMAGING AND MODELING OF MURINE SPERM DURING CAPACITATION PROCESS

Submitted by

Xinran Xu

Department of Electrical and Computer Engineering

In partial fulfillment of the requirements

For the Degree of Doctor of Philosophy

Colorado State University

Fort Collins, Colorado

Summer 2019

Doctoral Committee:

Advisor: Diego Krapf

Ali Pezeshki
Brian Munsky
Michael Tamkun

Copyright by Xinran Xu 2019

All Rights Reserved

ABSTRACT

SUPER-RESOLUTION IMAGING AND MODELING OF MURINE SPERM DURING CAPACITATION PROCESS

The effort to achieve better spatial resolution beyond the diffraction limit has been dedicated for many years. In the past decade, super-resolution microscopy methods have successfully advanced into extremely powerful tools to reveal hidden three dimensional structures and properties in various biological complex systems. Here we use single-molecule localization based three dimensional super-resolution microscopy to study the mouse sperm capacitation process, a critical step in gaining the fertilization ability. On top of that, we have constructed a model to represent this signaling pathway in order to be able to predict the cellular event within the capacitation.

The major subjects we are interested in can be categorized into two parts: actin-based cytoskeleton and capacitation-associated signaling proteins. In the midpiece, we discovered that F-actin forms a highly specialized double helical structure in the midpiece but this helical structure disappears in the pricipal piece, which is the very first observation among species. Similarly, the distinctive compartments regarding actin-binding proteins have also been visualized in the mouse sperm tail.

Additionally, the structure as well as localization of capacitation central mediator, protein kinase A, have been investigated to address the significance of spatial positioning during the capacitation event. As the capacitation end point reporter, tyrosine phosphorylation localization has been studied to help identify its real upstream kinase among other candidates. As in many regulating processes, second messenger Ca^{2+} plays a vital role in the capacitation process, which needs to be conveyed by the sperm specific calcium channel CatSper. We show the structural relation of a small GTPase Cdc42 to CatSper, implying its key role in transporting Ca^{2+}.

Considering that major critical signaling molecules are well characterized in the complex capacitation network, we choose a different method–stochastic modeling, other than experimental studies, surpassing the need for probing the behavior of a large number of individual cells over time, to describe capacitation process and furthermore to predict the behavior of sperm. With the known pathways of those signaling molecules in hand, we are able to build a model by utilizing chemical master equations. A couple sets of experimental measurements are used to assist in quantifying the model.

ACKNOWLEDGEMENTS

Throughout the past five years of my doctoral studies, I have been fortunate enough to have been surrounded by an incredible and invaluable supporting squad. In some way, their contribution to this thesis is way beyond my own.

I would like to extend my uttermost appreciation and gratitude to my advisor Dr. Diego Krapf for playing the role of sage guide and supportive mentor. Without his belief in me and providing professional and academic support, I would never reach this extremely important life milestone. I extend my deepest thanks for everything he has contributed to my work.

To my lab mates: Sanaz Sadegh guided me through my formative years. Kanti Nepal had been a great supportive colleague. They were both champions and critics whenever necessary. To my friends: Nasim Pica, Bret Pica, Michael May, Mohammad Tanhaemami, Anthony Nicholson, Xiaohui Ye, Yajing Liu, Ye Zhao, Youyang Gao, Lan Chen, Xueyang Hu, Xiang Sun, Wei Zhan, Wen Zhang, Jian Zhang, Jiaojun Ke, When life hits low, they were always there for me. Thanks for having my back when I fell and lifting me up. To my collaborators: Adal Sabri, María Gracia Gervasi, Guillermina M. Luque, Dr. Mariano Buffone and Dr. Dario Krapf, it has been a wonderful journey working along all of you. Besides the prolific accomplishments we have built together, it is the friendships that make this journey even more meaningful.

Great thanks are also due to Leif Anderson and other maintainers for building this LaTeX document class, allowing me to meet the graduate school formatting requirements with no effort on my part.

Last but not the least, I would like to thank my parents for loving and supporting me unconditionally, especially my mom. This success is just a small token of appreciation for my parents. They are worth my eternal gratitude, as always.

DEDICATION

I would like to dedicate this thesis to my family.

TABLE OF CONTENTS

LIST OF TABLES

LIST OF FIGURES

Chapter 1

Introduction

Reproduction is a fundamental feature of all known life and important for species continuum. In mammals, this process heavily relies on specialized cells: sperm and oocyte. Simply speaking, individual sperm cells need to swim in search of the egg and fuse with the egg to develop into a zygote. In order to achieve this goal, sperm need to go through a complex biochemical process known as capacitation, which is driven by molecular changes in the sperm after ejaculation and happens when sperm reside in the female reproductive tract including a series of major biochemical transformations [1,2]. The first capacitation was discovered by Chang and Austin independently in the 1950s, which holds a crucial role for future development of *in vitro* fertilization techniques [3, 4]. At the biological level, two critical events occur during capacitation: a switch from progressive motility to hyperactivation characterized by high amplitude and asymmetrical beating pattern of the sperm tail that enables sperm to travel to the egg [5]; and the preparation for an exocytosis event, known as acrosome reaction, to facilitate the fusion between sperm and egg [6].

Filamentous actin is a key factor in exocytosis in many cell types. It has been shown that F-actin holds together the molecular players of secretory pathway, determines the precise site for ganule exocytosis and shapes the exocytotic responses in secretory cells. In addition, stabilization of the actin network inhibits exocytosis, whereas depolymerization of this network increases the number ofr docked scretory granules and enhances the exocytotic response [7–10]. As in somatic cells, the actin cytoskeleton of mammalian sperm is dynamic. While during sperm capacitation, polymerization is predominant [11, 12], during the acrosome reaction, actin depolymerization occurs [13]. Previous studies regarding actin polymerization/depolymerization were exclusively performed in fixed capacitaed sperm or by means of using isolated membranes that had either been exposed or not to acrosome reaction inducers [11, 12]. In addtion, most studies evaluating filamentous actin in mamalian sperm were performed using phalloidin conjugated fluorophores, which is toxic and not capable of crossing the cell plasma membrane of live cells [14–16]. This becomes challenging

to study the actin dynamics in real time using live cells. But even with fixed cell, the sub-cellular localization and arrangment of actin cytoskeleton have never been studied.

At the molecular level, it all starts with the exposure of sperm to the high bicarbonate HCO_3^- concentrations in either the seminal fluid or in *in vitro* capacitation media. Besides, Ca^{2+} serves as a complementary role for the initiation of the capacitation process. The main target for HCO_3^- in this context is the SACY (soluble adenylyl cyclase), which becomes activated upon the HCO_3^- binding, which results in the elevation of intracellular concentration of cAMP (cyclic adenosine monophosphate) and the rapid activation of PKA (Protein Kinase A) [17, 18]. This cascade of signaling events occurs very fast, around 1 min. Multiple evidence have suggested that the activation of PKA is the upstream of the most known capacitation associated events, which makes the PKA as the essential central mediator, mediating a wide range of downstream reactions [19]. Those capacitation associated events include but not limited to actin remodeling [12], a modification of plasma membrane components [20], changes in intracellular pH [21], an increase Ca^{2+}, a change in the membrane potential as well as phosphorylation of tyrosine residues through PKA [22, 23]. Even though each of these events during capacitation are known, the coupled mechanisms underlying changes through which sperm acquire the capacity to fertilize are still poorly understood.

Tremendous efforts have been put into the study of the sperm capacitation signaling pathway. It is known that the capacitation event only occurs at the right time within proper environment. Various proteins are also spatially regulated and confined to ensure its occurrence. In the last few decades, the revolutionary development of fluorescent proteins and other genetically encoded fluorescent labels have allowed us to visualize specific proteins in both fixed and live cells. However, the diffraction limited resolution of conventional fluorescence microscopy hinders us from studying the mechanism from the subcellular level at the nanoscale, which approximately yields a PSF (point spread function) with a lateral size of $\sim$ 250 nm and axial size of $\sim$ 500nm as formulated in Eq. ([1.1-1.2]) [24],

$$\triangle x, y = \frac{\lambda}{2NA} \tag{1.1}$$

$$\triangle z = \frac{2n\lambda}{NA^2} \tag{1.2}$$

where λ is the optical wavelength, n is the refraction index and NA is the numerical aperture of the objective.

In addition, mature sperm are transcriptionally silent, meaning there are no transcriptions from DNA to RNA and no translations into new proteins. Thus post-translational modifications of proteins are essential for functional or physiological changes including the capacitation process [25]. Nevertheless, the nanoscale sub-cellular architectures of proteins in sperm, one of the key ingredients to determine the mechanical properties of cells, are still lacking. Meanwhile, quantitative models of the capacitation pathway are missing in general. Stochastic modeling has never been attempted to integrate the key players involved in the capacitation process for quantitative understanding as well as predicting the molecule states and concentration fluctuations.

Given the fact that cytoskeleton holds a crucial position in arranging the subcellular organelles spatial localization, integrating the cell shape, coordinating the cell dynamic and motility [26], it is intriguing to see how the actin cytoskeleton appears to be in the sperm as well as other signaling proteins that structurally orchestrate capacitation process via a stochastic PKA-dependent pathway, since the structure is intimately linked with the function. The fertilization competence acquisition only happens after the capacitation. Changes in the subcellular architecture are expected to take place within this delicate process. With that being said, we've applied the super-resolution imaging technique to investigate the arrangement of the actin cytoskeleton as well as other regulating proteins.

The presented work here answers following key questions: how is actin cytoskeleton organized in the sperm? Does this organization maintain or change during the evolution of the capacitation? How do different components of the signaling pathway spatially localize in the sperm? Does the inhibition of the PKA-dependent pathway spatially affect the capacitation process? Can this process be modeled with a stochastic framework?

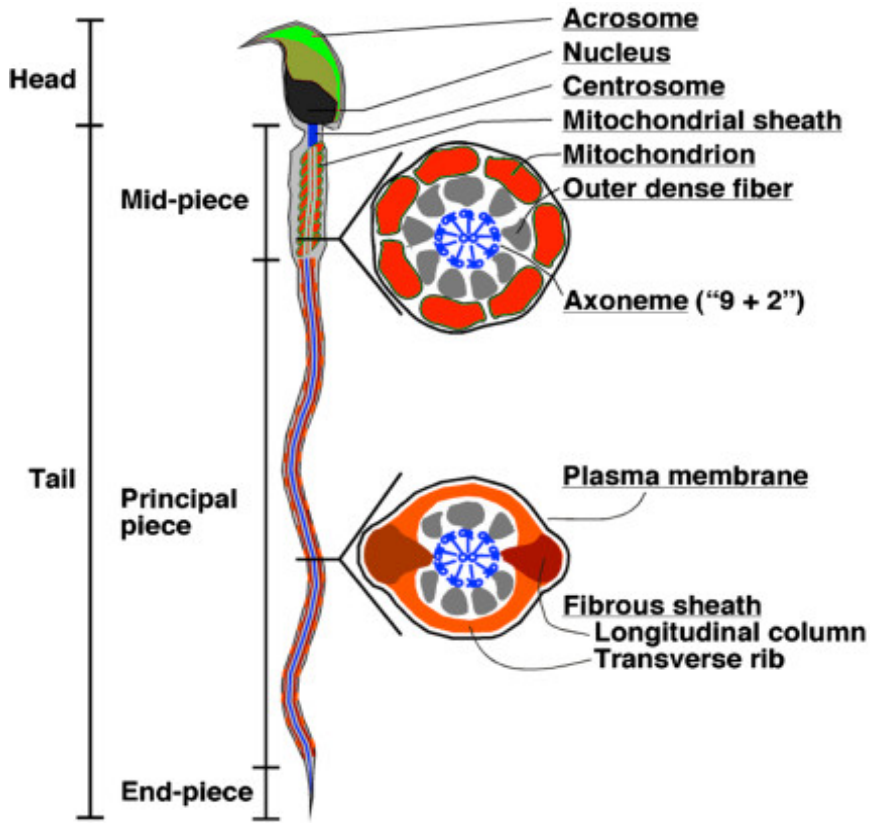

Figure 1.1: Diagram of the mammalian sperm cell [28].

1.1 Spermatozoa structure

Not surprisingly, the signaling molecules in spermatozoa are tightly regulated and spatially confined to function well. The mammalian sperm are highly polarized, having a very unique morphology: a head and a tail. Fertilizing an egg is the ultimate well-defined purpose for sperm [27]. For better understanding, the sperm structure in detail is shown in Fig. 1.1 [28]. The nucleus with highly condensed DNA is stored in the sperm head. Another important compartment is called acrosome, which contains enzymes to assist the fusion between the sperm and the egg. The sperm tail and head are joined by a connecting piece, a septin-rich ring structure annulus, and are further organized into different compartments with specific functions in motility, ATP generation, exocytosis and sperm-egg fusion [29]. Longitudinally, the sperm tail is categorized into the midpiece, the principal piece and the end piece. Radially, these compartments are organized around the "9+2" arrangement axoneme, which consists of a central pair surrounded by nine peripheral microtubule

doublets [30]. In both the midpiece and the principal piece, the axoneme is surrounded by ODFs (outer dense fibers). In the midpiece, the ODFs are wrapped in mitochondria organized in an end-to-end touching configuration that forms a double helical structure [31]. In a similar manner, the principal piece ODFs are surrounded by a fibrous sheath [30].

The aforementioned capability of sperm cells to fertilize is one of the most fundamental aspects of mammalian reproduction. Infertility and subfertility resulting from the incapability is today a huge burden on some couples. About 12% or 7.3 million women aged 15-44 have fertilization problems, while 9.3% for men aged 25-44 in 2006-2010 [32]. In order to enable new treatments, an understanding of the fertilization process is imperative.

1.2 Super-resolution imaging for subcellular structure with ada -ptive optic system

Since the nanoscale precision of the single fluorescent molecule could be determined as high as 1 nm [33], the high resolution of image is very likely anticipated as long as two fluorescent emitters are not closely spaced so that they can be optically distinguishable. The single molecule localization based super resolution imaging approach indeed successfully adopts this fundamental theory to overcome the Abbe's diffraction limit, in which an object imaged by an optical system has a minimum resolvable distance that is approximately half the wavelength of imaging light source [34,35]. Specifically, the super-resolution imaging technique we implemented on our home-built microscope is named STORM (stochastic optical reconstruction microscopy) [34]. The key ingredient in this approach is the photoswichable fluorescent probes, which can alternate between a non-fluorescent state and fluorescent state for multiple switching cycles with the proper excitation. Fig. 1.2 illustrates the principle of STORM: in one single frame, only a sparse subset of fluorophores are activated, which avoids the overlapping and enables the high precision localization of molecules. Over sequentially imaging, the superposition of those sparsely distributed fluorophores localizations give rise to the high resolution reconstruction.

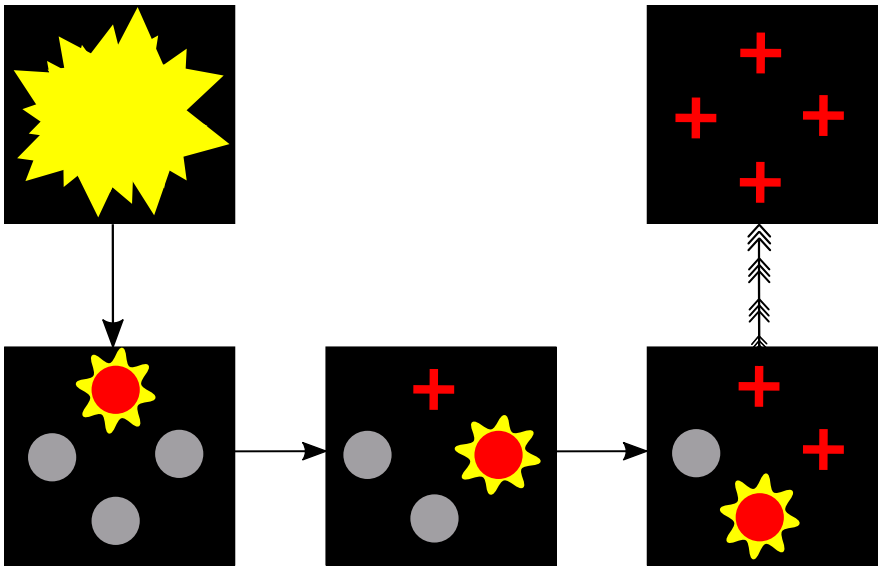

Figure 1.2: Sketch of the principle of STORM. Instead of exciting all molecule at one time, STORM only excites part of molecules that are not closely spaced so that the localization of those molecules can be differentiated. The accumulation of each individual localization builds up the super-resolution reconstruction.

Given the fact that all the cells and proteins are three dimensional objects, the study of 3D structure to collect more complete information becomes more meaningful than the 2D investigation. With the utilization of astigmatism, where the light rays propogate in two perpendicular planes have different foci within the optical system, STORM can be extended from 2D to 3D [34]. The astigmatism leads to two different focal planes which reshape the PSF with different degree of ellipticity [34]. By fitting a 2D elliptical Gaussian function to those elongated PSF, the z location can be quantitatively resolved. The relation between the ellipticity and the z localization is calibrated before the imaging and it is represented by calibration curve which tells the z location with certain ellipticity.

However, the challenge still exists. We used the cylindrical lens to induce the astigmatism at the beginning phase of the project. Unfortunately, the astigmatism suffers from the lack of control of the optical distortion and the significant optical aberration introduced by both the existing optical setup and the cylindrical lens, which deforms the PSF symmetry. In order to solve this PSF distortion issue, we employed MicAO adaptive optics system, which consists of a 52-actuator deformable mirror that can be controlled in a reversible manner, and wavefront sensor to correct

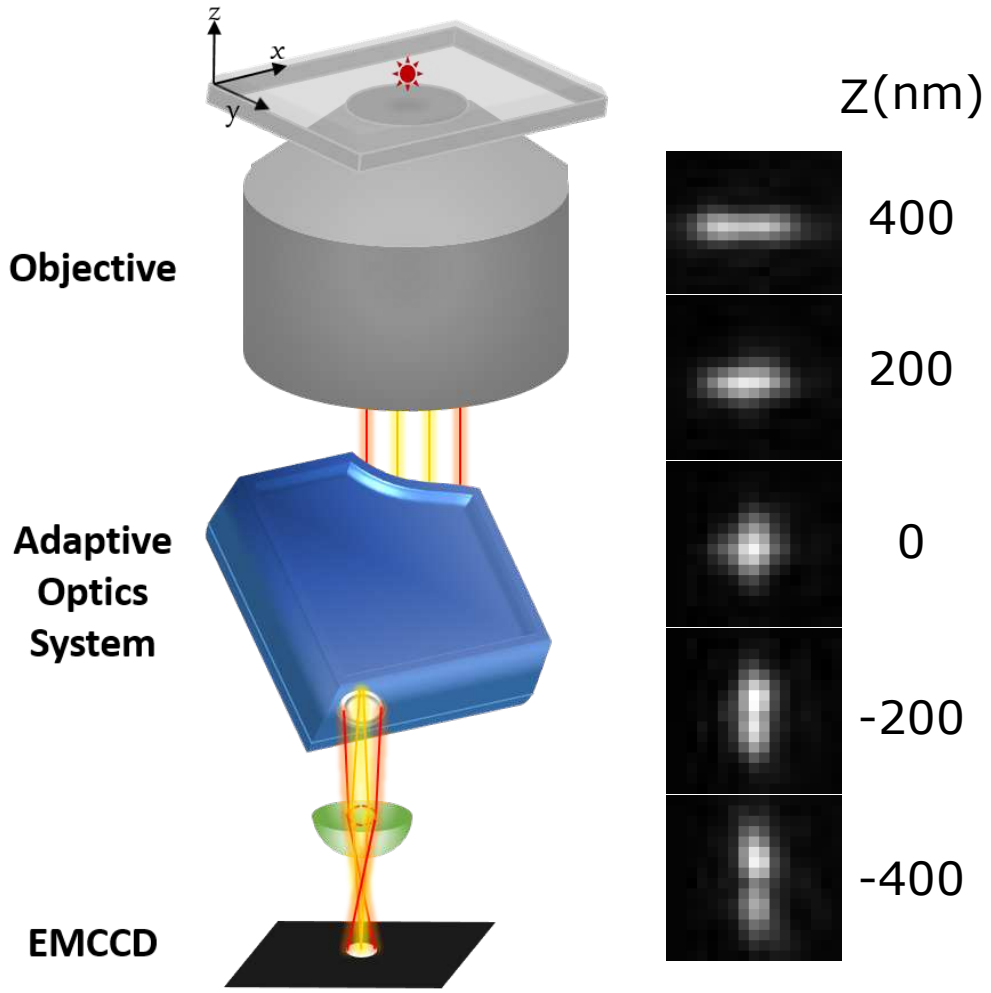

Figure 1.3: Experiment optical setup illustration and representative single bead PSF with astigmatism. Emission emitted from samples comes through the adaptive optics system for optical aberration correction and astigmatism manipulation, then gets collected by the camera (Left side). A single fluorescent bead PSF shows two different orientations at different z height due to two focal planes introduced by astigmatism (Right side).

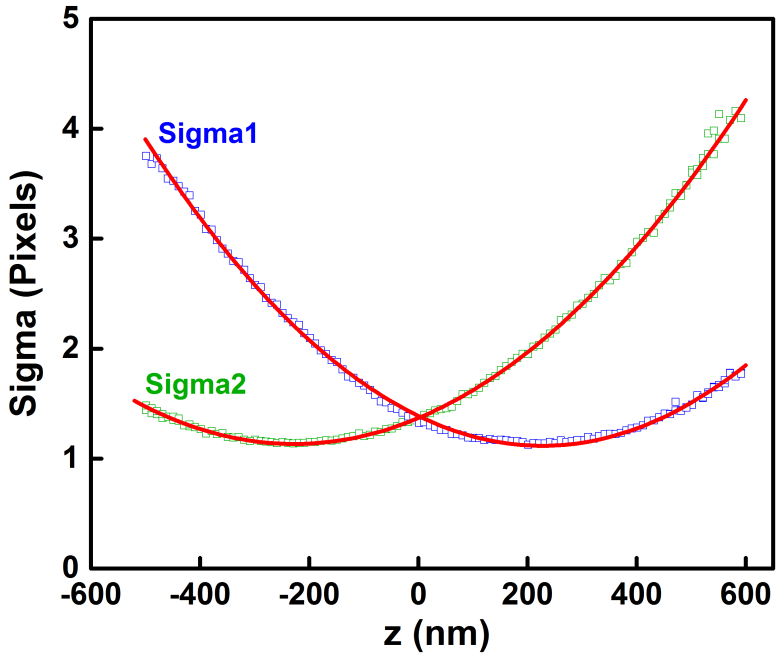

Figure 1.4: Representative calibration curve. This calibration curve is generated from z stack with equal step size n=10nm up to 2 μm for a single 100 nm size TetraSpeck fluorescent bead (Thermo Fisher, T7279).

the optical aberrations [36]. A single 100 nm diameter fluorescent bead is selected in the field of view to complete the PSF optimization procedure. Wavefront sensor measures the wavefront of the given point source with high precision and any optical aberrations are immediately corrected by the deformable mirrors with built-in algorithm [37]. Afterwards, a user-defined degree of astigmatism can be introduced by tweaking the deformable mirrors at no cost of aberrations. The fluorescence emission path with MicAO adaptive optics system and the corrected single bead PSF with astigmatism are shown in Fig. 1.3. One good example of achieved z calibration is shown in Fig. 1.4, generated by using ThunderSTORM plugin in FIJI [38].

1.3 Overview of this dissertation

In the second chapter we image the actin-based cytoskeleton, including actin, spectrin and adducin in the sperm flagellum with 3D STORM. The super-resolution reconstructions from images display different structural behaviors among compartments. Here we report a novel filamentous

actin structure observed in the sperm midpiece, which is associated with the distribution of mitochondria. At the same time, the newly found F-actin localizations in the sperm head are also discussed.

In the third chapter we quantify the spatial dynamics of PKA before and after capacitation. As the downstream PKA substrate responsible for pY (tyrosine phosphorylation), the tyrosine kinas, FER's identity has been corroborated through the structural analysis, in comparison to the localization of pY.

The fourth chapter shows that Cdc42 also has a four-column structure resembling the structure of CatSper channel. This unique structure got abrogated once the gene of CatSper gets knocked out, which suggests the tight regulation between these two proteins in the context of Ca^{2+}.

In the last chapter, we have modeled the ensemble stochastic capacitation signal pathway. A model characterized by ODE (ordinary differential equations) featuring the temporal evolution of cAMP and pY has been derived and solved at discrete Ca^{2+} concentrations.

Chapter 2

The actin cytoskeleton exhibits structural diversity in different compartments of the mouse sperm

2.1 Introduction

[1] Mammalian sperm are highly polarized and specialized cells composed of a head and a tail, and they have a single well-defined goal: to fertilize an oocyte [27]. This specific functionality is granted by a tightly organized cellular structure. The sperm tail and head are joined by a connecting piece, and are further organized into different compartments with specific functions in motility, ATP generation, exocytosis and sperm-egg fusion [41]. Some of these subdivisions are membrane-enclosed and others are separated by diffusion barriers that segregate proteins and metabolites. Longitudinally, the sperm tail is divided into the midpiece, the principal piece and the end piece. The midpiece and the principal piece are separated by the annulus, a septin-rich ring structure. Radially, these compartments are arranged around the axoneme, which consists of a central microtubule pair surrounded by nine peripheral microtubule doublets [30]. In both the midpiece and the principal piece, the axoneme is surrounded by ODFs. In the midpiece, the

[1]The work presented in this chapter has two parts. The first part has been performed in collaboration with Blanca Carbajal-Gonzalez (Science Center Microscopy Facility, Mount Holyoke College, South Hadley), Dr. María Gracia Gervasi, Prof. Pablo Visconti (University of Massachusetts, Amherst) and Prof. Mariano Buffone (Instituto de Biología y Medicina Experimental, Buenos Aires, Argentina) , while second part is in collaboration with Dr. Ana Romarowski, Dr. Guillermina M. Luque, Prof. Marinao Buffone (Instituto de Biología y Medicina Experimental, Buenos Aires, Argentina), Ángel G. Velasco Félix, Prof. Adán Guerrero (Laboratorio Nacional de MicroscopÄśá Avanzada, Instituto de BiotecnologÄśá , Universidad Nacional Autónoma de México (UNAM), Cuernavaca, Morelos, México), Paulina Torres Rodríguez, Castón Contreras-Jiménez, Claudia Sánchez-Cárdenas, Héctor V. Ramírez-Gǿmez, Prof. Alberto Darszon (Departamento de Genética del Desarrollo y FisiologÄśá Molecular, Instituto de BiotecnologÄśá , Universidad Nacional Autónoma de México (UNAM), Cuernavaca, Morelos, México), Dr. María Gracia Gervasi, Prof. Pablo Visconti (University of Massachusetts, Amherst) and Prof. Dario Krapf (Instituto de Biología Molecular y Celular de Rosario, Rosario, Argentina). In part one, I ran all the super-resolution imaging experiments and analysis. Dr. María Gracia Gervasi contributed equally with the experiments and materials preperations. Western blotting, SIM and IF experiments were performed by Dr. María Gracia Gervasi. TEM was performed at the ARBL Morphological Services Facility at CSU in consultation with Dr. D. N. Rao Veeramachaneni. In part two, we contributed the work with super-resolution imaging of actin in the sperm head with Phalloidin. This chapter has been published in Journal of Cell Science [39, 40].

ODFs are wrapped in mitochondria organized in an end-to-end touching configuration that forms a double helical structure [31]. By contrast, the principal piece ODFs are surrounded by a fibrous sheath [30]. The midpiece and principal piece structural organizations are essential for sperm function. Sperm presenting defective structures in either the mitochondrial sheath, the fibrous sheath or the ODFs have abnormal morphology as well as impaired motility and fertility [42–46].

The scaffolding framework that maintains the organization of the sperm flagellum cytoskeleton and its differentiated structures is poorly understood. In addition to the axoneme, actin and actin associated proteins have been documented in sperm from many species [47]. Actin is an abundant and highly conserved protein among eukaryotes, and is essential for diverse cellular functions, such as cell shape maintenance, motility, membrane organization [48] and cytokinesis [49]. Diverse proteins interact with actin filaments and form complex cytoskeletal structures that ensure cell functionality. In erythrocytes, polymerized actin, together with spectrin and adducin, form a subcortical meshwork that gives the cell membrane the elasticity required to survive in the circulatory system [50]. In neurons, short F-actin filaments capped by adducin are organized as periodic rings interconnected by spectrin along the axon [51]. In HEK (human embryonic kidney) cells, a cortical actin meshwork forms a fractal structure that organizes the plasma membrane [52, 53]. The presence of actin has been reported in different compartments of mammalian sperm including the tail [54, 55], and actin dynamics have been proposed to play a role in sperm motility and the acrosome reaction [11, 56, 57]. However, despite the importance of actin organization and dynamics, little is known about the structure, function and regulation of actin in sperm.

In this chapter, we use 3D STORM to uncover the actin based cytoskeleton in the sperm flagellum. We find that the sperm midpiece and principal piece have specialized actin structures. In the midpiece, polymerized actin forms a double-helix that follows the mitochondrial sheath, a type of filamentous actin structure that had not been previously observed. By contrast, actin in the principal piece is radially distributed from the axoneme to the plasma membrane. Furthermore, the distributions of F-actin in the sperm head has been confirmed. In addition, the actin-associated proteins spectrin and adducin, which are involved in shaping the actin cytoskeleton in other cell

types, are also organized differentially in both sperm tail compartments. These results suggest a role of polymerized actin in the molecular organization of flagellar structures involved in motility regulation and sperm function.

2.2 Results

2.2.1 F-actin localization and structure in mouse sperm midpiece

The localization of F-actin in mouse sperm was initially determined by immunofluorescence using two different approaches: (1) labeling with fluorescent phalloidin, and (2) using a transgenic mouse line that expresses LifeAct-GFP (Green Fluorescence Protein), a 17-amino-acid small peptide that stains F-actin without altering its dynamics, in all cell types [58]. In both cases, F-actin was observed in the sperm head and throughout the tail, with higher intensity in the midpiece (Fig. 2.1(A),(B)). This localization is in line with previous reports of F-actin in sperm [12, 42, 59]; however, the narrow shape of the sperm flagellum, together with the limitations in resolution of widefield microscopy, did not allow us to observe details of the actin structure. To investigate the organization of F-actin in the flagellum in detail, we imaged AF (Alexa Fluor) 647 phalloidin-stained sperm by using 3D STORM [60], a super-resolution technique that has been previously employed successfully to evaluate the localization of different proteins in mouse sperm [61, 62]. Consistent with results obtained using widefield immunofluorescence imaging (Fig. 2.1(A),(B)), STORM showed a high density of F-actin in the tail. In addition, STORM revealed two different structures in the midpiece and the principal piece (Fig. 2.1(C)). Note that Fig. 2.1(C) also includes z-axis information with the depth color coded. While in the midpiece F-actin forms a periodical structure, in the principal piece, actin is uniformly distributed along the flagellar length. Fig. 2.1(D) shows a magnification of the periodical arrangement of F-actin found in the sperm midpiece. The cross-section of the midpiece showed that F-actin is completely absent from the central axoneme (Fig. 2.1(E)). It is worth noting that, besides the prevalent helical structure observed in the midpiece, short F-actin bundles are found spread along the circumference of the flagellum (Fig. 2.1(F),(G)). In order to exploit the cylindrical symmetry of the flagellum, we converted the

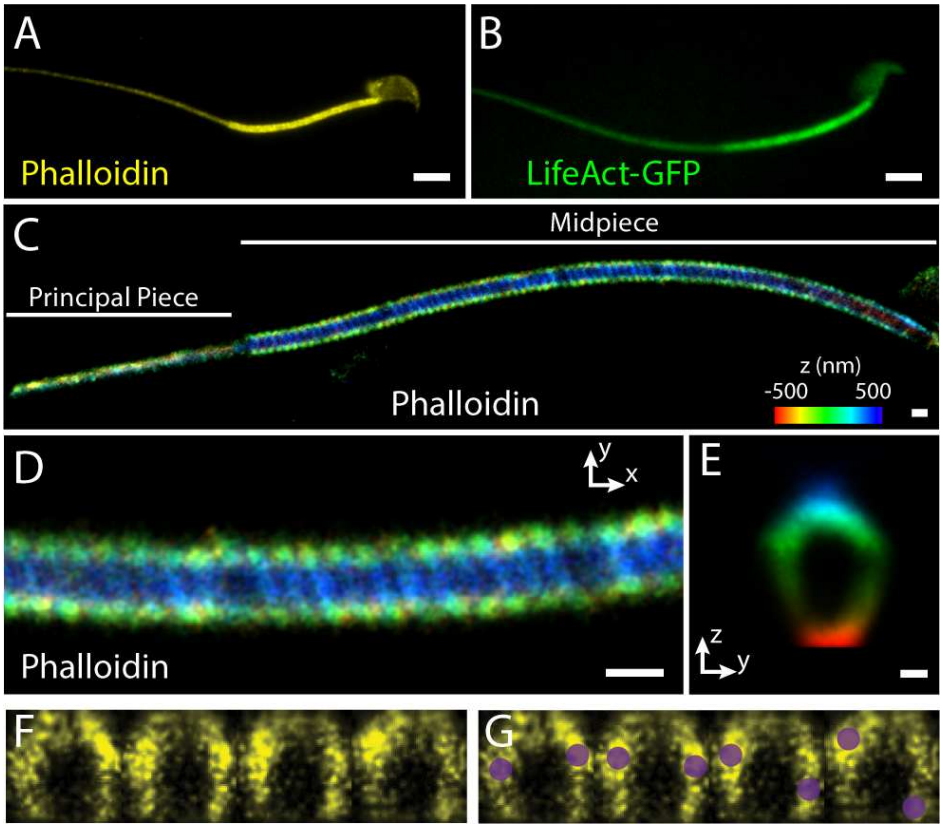

Figure 2.1: Actin structure in the sperm flagellum. (A) Widefield image of actin labeled with phalloidin AF 647 in a sperm cell from a wild-type mouse. (B) Sperm from a transgenic mouse that expresses LifeAct-GFP. (C) 3D STORM reconstruction of actin labeled with phalloidin-AF647 in the sperm tail, with the z-position information color coded. The whole midpiece and part of the principal piece are shown in the image, as labeled. The reconstruction is colored according to the localization height as indicated in the color map. (D) Magnification of part of the midpiece of the sperm shown in C. (E) Composite sum of the intensity projections of cross-sections along 7 μm of the sperm midpiece. (F) Cross-sections of the actin super-resolution image separated by 39 nm along the sperm axis. (G) Sketch of the location of the higher intensity structure overlaid on the cross-sections in panel E. Scale bars: 5 Îijm (A,B), 500 nm (C,D), 200 nm (E).

molecule localizations as found by STORM into cylindrical coordinates (r, θ, z'). Note that when working in cylindrical coordinates we refer to z' as the flagellum axis, but in Cartesian coordinates it is the direction normal to the coverslip, so that in Cartesian coordinates the sperm lies on the xy plane, as sketched in Fig. 2.2(A). Fig. 2.2(B) shows the distribution of F-actin radial localizations $P(r)$ in the midpiece for different individual cells, together with the mean distribution. The distribution of radial localizations is presented as an area density with normalization $2\pi \int_0^\infty rP(\mathbf{r})dr = 1$ and, thus, the mean radius is obtained as:

$$\langle r \rangle = 2\pi \int_0^\infty r^2 P(\mathbf{r})dr \tag{2.1}$$

The radial distribution in the midpiece (Fig. 2.2(B)) indicates that F-actin peaks at $\sim$300 nm from the center of the flagellum. A graphical representation of F-actin localization in terms of the azimuth angle θ vs axial distance z' along the midpiece shows that the periodical F-actin organization found in this region forms a helical structure (Fig. 2.2(C)). It is possible to trace an actin line in this representation from the angle 180° to âĹŠ180°, at which point the trace connects to a different line at 180Âř as expected from a helix. However, when connecting these traces, one trace is skipped; namely, we observe one continuous helix composed of traces 1, 3, 5, ... that alternates with a second helix composed of traces 2, 4, 6,..., as labeled on the top of Fig. 2.2(C). Thus, the actin structure forms two congruent helices. The distance between the F-actin helices was accurately measured cell-by-cell by using a Fourier transform method. First, the θ versus z' representation was coarse grained into bins along θ as shown in Fig. 2.2(C). Each angle $theta$ yields a series of intensities $I_\theta(z)$. Then, a power spectrum was obtained from each intensity series by means of a Fourier transform. Using an azimuthal angle bin size of 30°, we obtained 12 different power spectra in each image, which were averaged to obtain one spectrum for each cell as shown in Fig. 2.2(D). In this representative cell, the spectrum shows a single (non-zero frequency) peak at a spatial frequency f_0=3.92$\pm$0.22 μm^{-1} [peak$\pm$half width at half maximum (HWHM)]. This analysis was performed in multiple cells, with all cells yielding a similar peak in the power

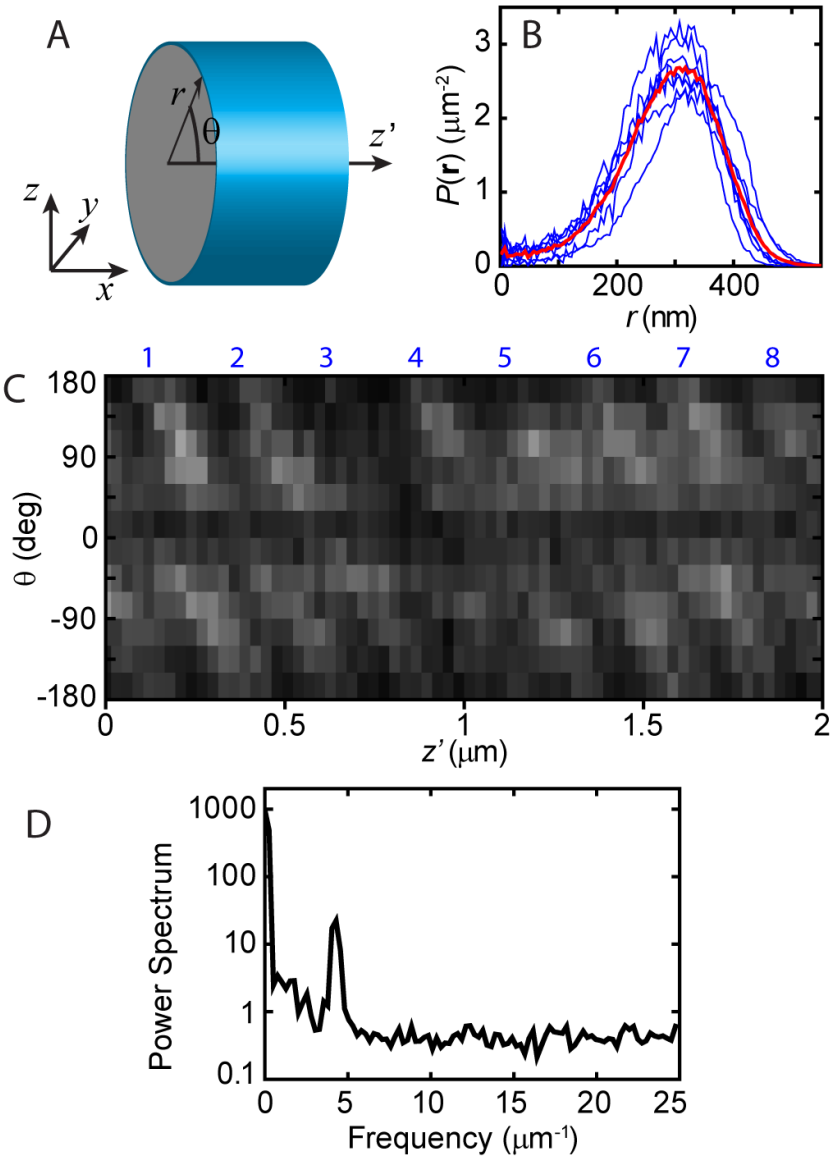

Figure 2.2: Analysis of the actin structure in the sperm midpiece. (A) Sketch of the Cartesian and cylindrical sets of coordinates used in the article in relation to the sperm flagellum geometry. (B) Radial distribution of F-actin localization in the midpiece. The blue lines are distributions from seven individual cells and the thick red line is their average. (C) Two-dimensional histogram of F-actin localization in terms of azimuth angle θ and axial position z' in the sperm midpiece, revealing stripes that follow a double helix. The blue numbers on the top of the histogram indicate gyre number as visual guides. (D) Representative single-cell power spectrum of the actin axial localization. The power spectrum is computed independently for each angle θ, and then all the power spectra from the different angles in a single cell are averaged as described in the text. A peak at 3.92$\pm$0.22 μm^{-1} (peak$\pm$HWMH) indicates the periodicity of the actin structure in this representative cell.

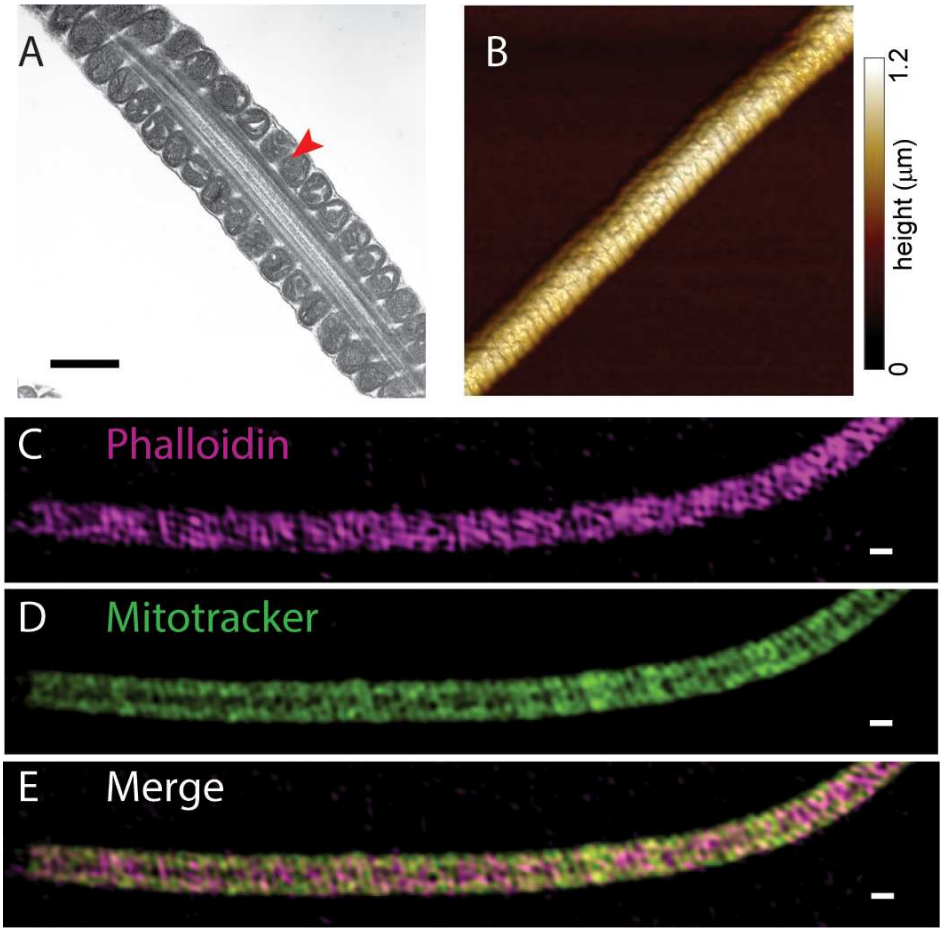

Figure 2.3: Organization of the sperm midpiece. (A) TEM image of the sperm midpiece showing the mitochondria, axoneme and plasma membrane. The red arrowhead indicates a distance of 300 nm from the center of the flagellum. (B) Surface topography of sperm midpiece as obtained by AFM. (C) SIM reconstruction of actin labeled with phalloidin-Alexa Fluor 647 in the sperm midpiece. (D) SIM reconstruction of mitochondria labeled with Mitotracker in the sperm midpiece. (E) Merge of phalloidin and mitotracker reconstructions shown in C and D. Scale bars: 500 nm.

spectrum. Namely, the mean peak corresponds to a distance between helices $1/\langle f_0 \rangle$=243.7$\pm$1.8 nm (mean$\pm$s.e.m., n=15).

Fig. 2.3(A) shows a TEM (transmission electron microscopy) image of a longitudinal section of the sperm midpiece. The mitochondrial organization, which displays a similar periodicity to the observed actin structure, is clearly visible. Thus, the helical actin structure in the midpiece follows the organization of the mitochondrial sheath. The red arrow in the figure indicates a distance of 300 nm from the center of the flagellum, which corresponds to the F-actin radius in the midpiece as found by STORM. Based on these measurements, the helical structure of actin presented a ra-

dial localization coincident with the radial center of the mitochondria, suggesting that the actin filaments are located in thin regions between mitochondria. The surface of the midpiece can also be investigated in extremely high resolution by means of AFM (atomic force microscopy). Fig. 2.3(B) shows an AFM topographic image of a sperm midpiece. Helical grooves, with the same periodicity as seen for actin, are also observed to decorate the surface. These measurements established that the midpiece surface exhibits the same pattern as that of the actin cytoskeleton. From the actin STORM reconstructions, it is possible to count the number of full helical turns (gyres) in the midpiece. We found that each of the two actin helices makes 43.7$\pm$0.25 (mean$\pm$s.e.m.; n=6 cells) full helical turns along the midpiece, which makes a total of 87 turns when considering both helices. This number is in excellent agreement with the number of mitochondria 'windings' around the flagellum. On average, the mouse sperm midpiece comprises a total of 87 mitochondria gyres arranged in a double helix [41]. We further investigated the organization of F-actin and the mitochondrial sheath by two-color SIM (structural illumination microscopy), a technique that allows an axial resolution of $\sim$120 nm. Fig. 2.3(C)-(E) shows the dual imaging of mitochondria labeled with MitoTracker Green FM and actin stained with Alexa Fluor 647-conjugated phalloidin. Consistent with our STORM results, the periodical structure of F-actin was also observed by SIM. Most importantly, the localization of F-actin appeared to generally alternate with the mitochondria arrangement (Fig. 2.3(E)).

2.2.2 Structural actin-associated proteins in the sperm midpiece

Two of the most widespread structural actin-associated proteins are spectrin and adducin. Often, actin, spectrin, and adducin form complex structures [63]. Well-known examples are found in erythrocytes [64] and neurons [51]. The specificity of the anti-spectrin and anti-adducin antibodies used here was validated by western blotting Fig. 2.4. Immunofluorescence microscopy revealed that both spectrin and adducin are present in the head and throughout the entire flagellum of mouse sperm (Fig. 2.5(A),(B)). A STORM super-resolution image of spectrin in a sperm flagellum is shown in Fig. 2.5(C), and a magnification of the midpiece is shown in Fig. 2.5(D). The cross

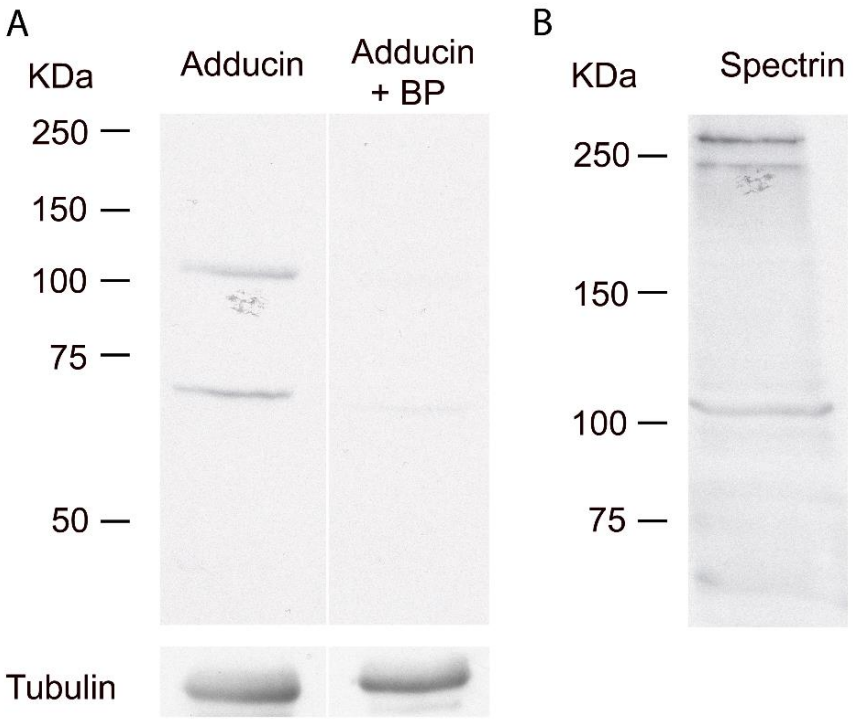

Figure 2.4: Validation of antibodies by Western blotting performed by Dr. María Gracia Gervasi. Sperm protein lysates were separated by SDS-PAGE and proteins were detected with the indicated specific antibodies. (A) Proteins were separated in 10 % gels, transfer to PVDF membranes and protein detection was done with anti-adducin specific antibody (cat. ab51130). Left panel corresponds to incubation with anti-adducin antibody alone, and right panel corresponds to incubation with anti-adducin antibody in the presence of 200 times excess of blocking peptides. Membranes were stripped and sequentially probed with anti-tubulin antibody for loading control. (B) Proteins were separated in 7 % gels, transfer to PVDF membranes and protein detection was done with anti-spectrin specific antibody (cat. s-1515). Images are representative of three independent experiments.

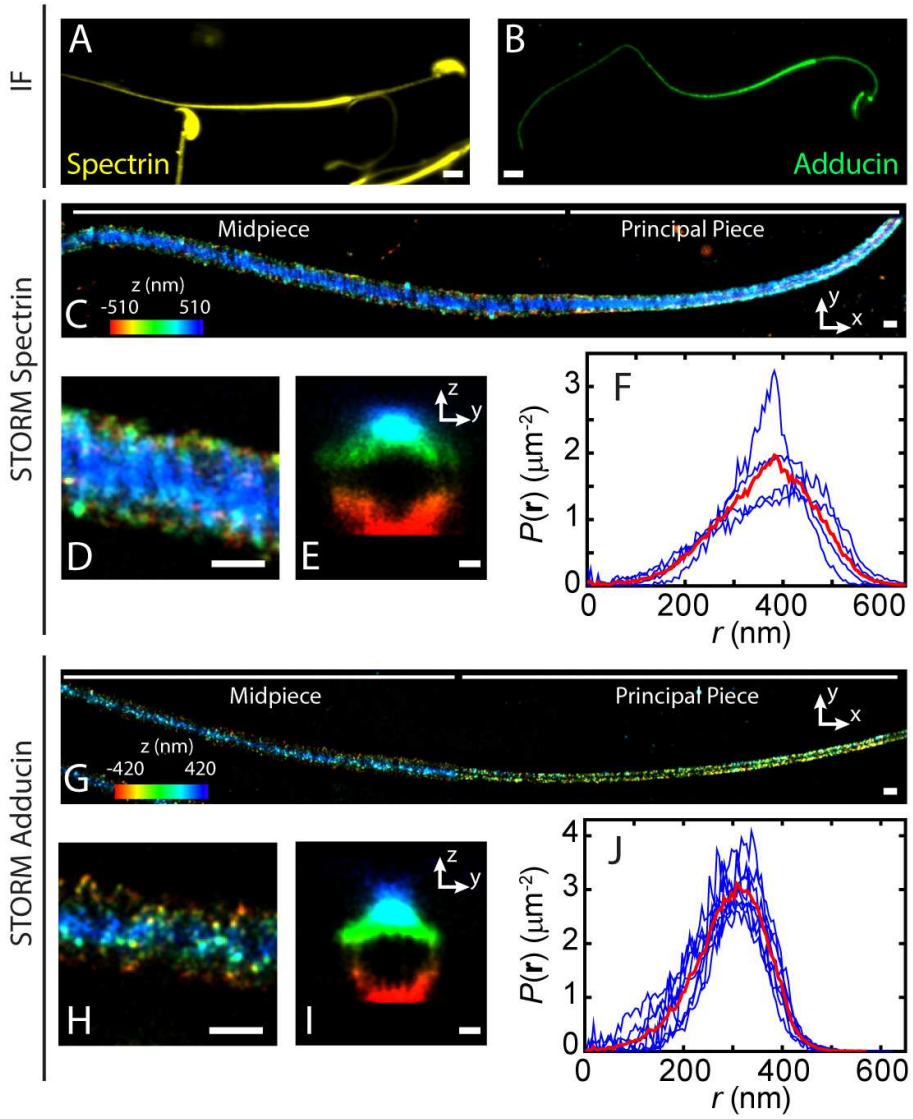

Figure 2.5: Localization of spectrin and adducin in the sperm. (A) Spectrin IF in sperm cells. (B) Adducin IF in mouse sperm. (C) 3D STORM reconstruction of spectrin in the sperm flagellum, color coded by depth, where the structure in both the midpiece and principal piece are observed. (D) Magnification of a section of the midpiece shown in C. (E) Composite sum of the intensity projections of spectrin cross sections along 8.3 μm of the sperm midpiece. (F) Radial distribution of spectrin localization in the midpiece. Blue lines are distributions from four individual cells and the thick red line is their average. (G) 3D STORM reconstruction of adducin in the sperm flagellum, color coded by depth, where the structure in both the midpiece and principal piece are observed. (H) Magnification of a section of the midpiece shown in G. (I) Composite sum of the intensity projections of adducin cross-sections along 3.4 μm of the sperm midpiece. (J) Radial distribution of adducin localization in the midpiece. Blue lines are distributions from eight individual cells and the thick red line is their average.

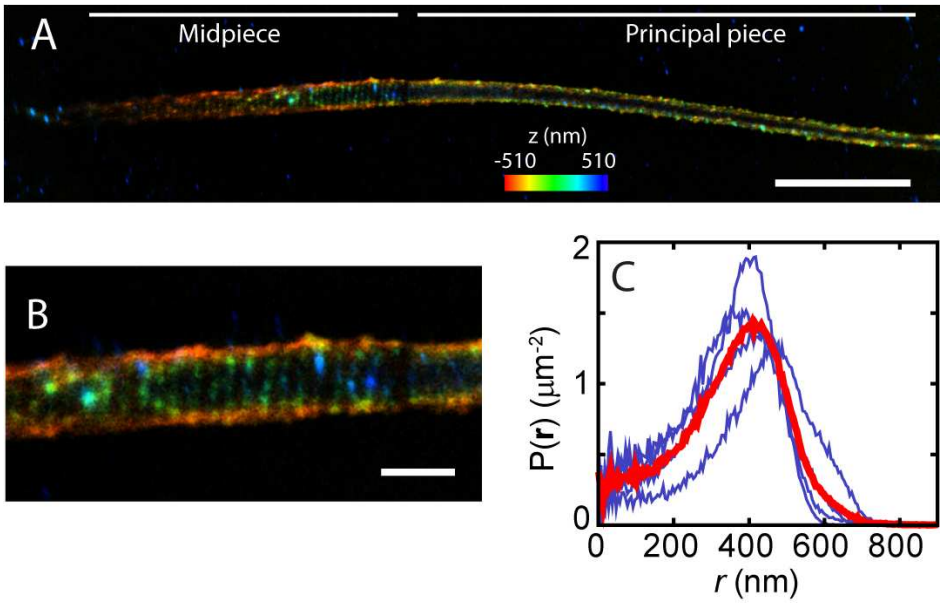

Figure 2.6: Super-resolution localization of spectrin in the sperm midpiece obtained with an alternative antibody. (A) STORM reconstruction of spectrin in the sperm flagellum where the structure in both the midpiece and principal piece are observed. (B) Zoom of a section of the midpiece of panel A. (C) Radial distribution of spectrin localization in the midpiece. Blue lines are distributions from four individual cells and the thick red line is their average. The scale bar in panel A is 5 μm, and in panel B is 1 μm. Anti-spectrin antibody used was purchased from Sigma (cat. s-1390).

section of the midpiece showed that spectrin is absent from the central axoneme (Fig. 2.5(E)). The analysis of radial localization indicated a maximum density at a radius of 410$\pm$23 nm (mean$\pm$s.d., n=4) in the midpiece (Fig. 2.5(F)), which suggests that spectrin is localized adjacent to the plasma membrane. Similar results were obtained when sperm were incubated with a different anti-spectrin antibody (Fig. 2.6).

STORM images of adducin show that this protein forms a sparse dotted structure in the midpiece and a more uniform structure along the principal piece (Fig. 2.5(G)). A magnification of the midpiece structure is shown in Fig. 2.5(H). The cross-section of the midpiece indicated that adducin is also absent from the central axoneme (Fig. 2.5(I)). The analysis of radial localization indicated that the highest density of adducin peaks at a radius of 306$\pm$16 nm (mean$\pm$s.d., n=8) in the midpiece. This localization is coincident with the localization of F-actin found in the same region.

2.2.3 Structure of the actin cytoskeleton and actin-associated proteins in the principal piece

The structural organization of the principal piece is key for sperm function and motility [30]. We evaluated the organization of the actin cytoskeleton and actin-interacting proteins in the principal piece. F-actin formed short bundles distributed throughout the principal piece (Fig. 2.7(A)). The cross section and the radial distribution analysis indicated that the maximum density of F-actin bundles is next to the axoneme and extended outwards to a radius of 300 nm (Fig. 2.7(B),(C)), independent of the distance to the annulus (Fig. 2.7(D)). Spectrin was found to be uniformly distributed along the length of the principal piece (Fig. 2.7(E)). The cross-section analysis showed that spectrin localizes in a ring-like structure (Fig. 2.7(F)). The radius was found to be largest at the annulus, where it is 305$\pm$25 nm (mean$\pm$s.d., Fig. 2.7(G)) and tapered towards the end of the flagellum (Fig. 2.7(H)). This localization was consistent with cortical localization of spectrin, as the sperm flagellum became narrower towards the end piece. Adducin localization was uniform in the principal piece (Fig. 2.7(I)). The cross-section showed that this protein also localized in a ring-like structure that extended longitudinally throughout the flagellum (Fig. 2.7(J)). The radial distribution analysis indicated that the maximum density of adducin is at a radius r=140 nm, and that this radius is independent of the distance from the annulus (Fig. 2.7(K),(L)).

2.2.4 F-actin localization in the sperm head using STORM

On top of the structural information obtained in the sperm flagellum, the F-actin localization, especially its dynamic changes in live sperm was also revealed in our collaborated work with Dr. Mariano Buffone's group (Instituto de Biología y Medicina Experimental, Buenos Aires, Argentina). By utilizing the powerful properties of SiR-actin, which is a live cell actin probe, six regions containing F-actin within the sperm head were discovered and defined as follows: (1) the perforatorium, staining in the more apical tip of the head; (2) the lower acrosome, labeling in the acrosomal region close to the anterior tip of the head; (3) the upper acrosome, staining over the entire cortical acrosomal cap; (4) a ventral, fluorescent signal in the lower edge of the head; (5)

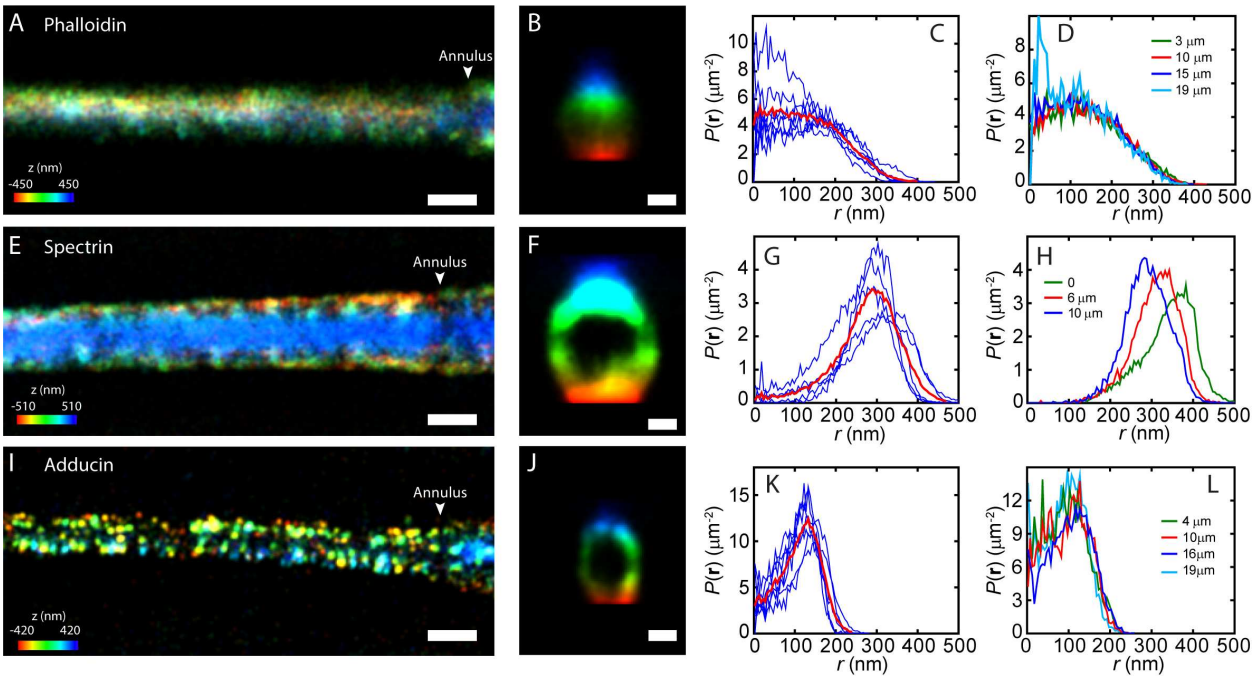

Figure 2.7: Actin-based cytoskeleton in the principal piece. (A) 3D STORM reconstruction of actin labeled with phalloidin-Alexa Fluor 647 in the sperm principal piece, color coded by depth. Part of the principal piece is shown in the image. The reconstruction is colored according to the localization height as indicated in the color map. (B) Composite sum of the intensity projections of actin cross-sections along 3.7 μm of the sperm principal piece. (C) Radial distribution of F-actin localization in the principal piece. The blue lines are distributions from seven individual cells and the thick red line is their average. (D) Radial distribution of F-actin localization in the principal piece relative to the distance from the annulus of one representative cell. (E) STORM reconstruction of spectrin in the sperm principal piece. (F) Composite sum of the intensity projections of spectrin cross-sections along 5.1 μm of the sperm principal piece. (G) Radial distribution of spectrin localization in the principal piece. Blue lines are distributions from five individual cells and the thick red line is their average. (H) Radial distribution of spectrin localization in the principal piece relative to on the distance from the annulus of one representative cell. (I) STORM reconstruction of adducin in the sperm principal piece. (J) Composite sum of the intensity projections of adducin cross-sections along 3.5 μm of the sperm principal piece. (K) Radial distribution of adducin localization in the principal piece. Blue lines are distributions from seven individual cells and the thick red line is their average. (L) Radial distribution of adducin localization in the principal piece relative to the distance from the annulus of one representative cell. Scale bars: 500 nm (A,E,I); 200 nm (B,F,J).

the septum, a clear fluorescent boundary between the equatorial and post-acrosomal segment; (6) a neck, a focused signal in the neck region. These patterns are represented in the schematic diagram along with a developed six-position binary code system shown in Fig. 2.8 [40]. Since most of the cells display two or more patterns simultaneously, the six-position binary code helps to distinguish the changes during the evolution of the capacitation process.

To investigate and further corroborate the organization of F-actin in the fixed sperm head in more detail, we applied STORM approach as mentioned before with phalloidin-AF647, owing to its optical properties. Consistently, the very similar F-actin distributions are observed as with the SiR-actin probe, shown in Fig. 2.9. This result further validates the novel F-actin structures in the sperm head revealed by SiR-actin. Also, these experiments demonstrated the advantage of using super-resolution microscopy to reveal F-actin structures in the sperm head that otherwise displayed a homogeneous distribution due to the diffraction-limited acquisition of these images.

2.3 Discussion

Similar to other cylindrical biological structures, the sperm flagellum relies on the cytoskeleton for its structural organization and specialized mechanical properties. Along its longitudinal axis, the sperm flagellum is organized in three different sections: the midpiece, the principal piece and the end piece. We used 3D STORM to study the structure of the actin cytoskeleton in the mouse sperm flagellum. Our results indicate that actin filaments and actin associated proteins are differentially organized in the midpiece and the principal piece.

In the midpiece, mitochondria are organized in a unique helical sheath enclosing the central axoneme and the ODFs [65]. The proper organization of the mitochondrial sheath is essential for sperm function and fertility [42, 44, 66]. Defects of sperm mitochondrial ultrastructure have been associated with decreased sperm motility and fertility [67]. In this work, we show that, in the midpiece, F-actin forms a double-helical structure with a periodicity of 244 nm. This actin structure is coincident with the organization of the mitochondrial sheath in mouse sperm [68]. Such a double-helix structure represents a novel actin architecture that, to the best of our knowledge, has

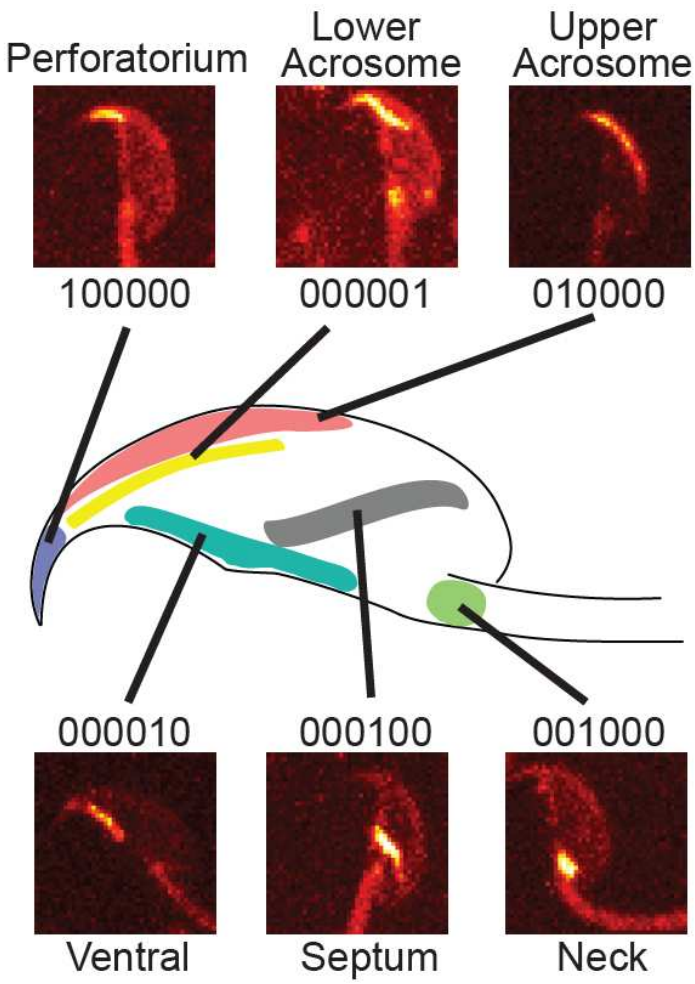

Figure 2.8: Representative diagram showing the six different F-actin structures within the live sperm head summarized by Dr. Buffone's group that they denote as the perforatorium, lower acrosome, upper acrosome, ventral, septum and neck. A representative confocal image of each pattern is displayed. A binary codewas used to determine the presence of these patterns in all the individual cells assessed. The binary code was defined as 1 (presence of signal at a given region) or 0 (absence of fluorescent signal). In addition, each position in the 6-digit code represents one of the patterns: the positions (from left to right) are assigned to perforatorium, upper acrosome, neck, septum, ventral and lower acrosome [40].

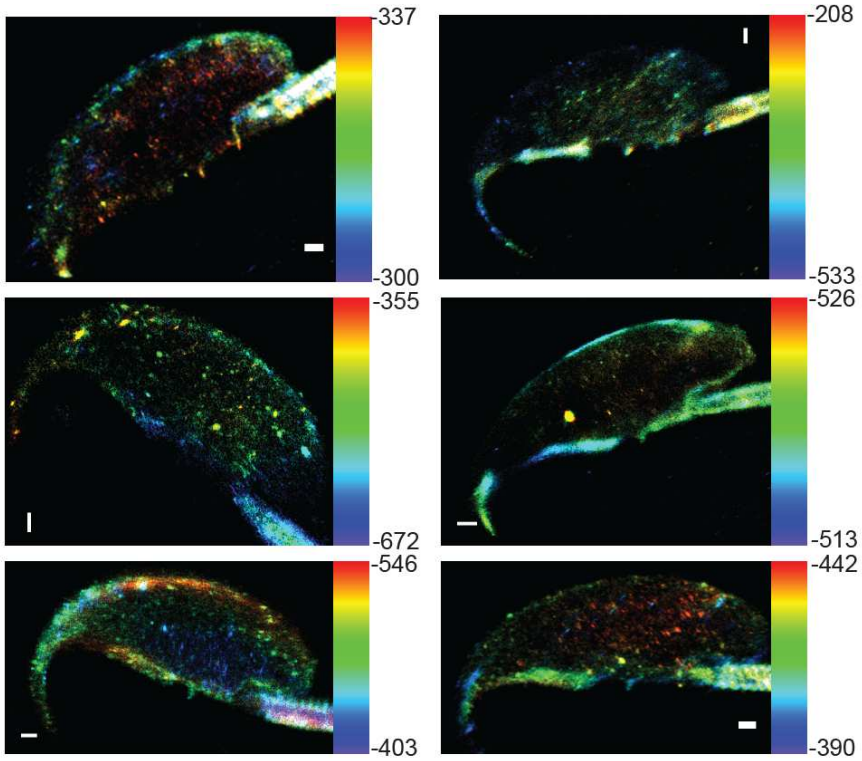

Figure 2.9: Representative images of 3D STORM super-resolution microscopy of F-actin in mouse sperm head. Scale bar: 500 nm. Non-capacitated sperm were stained with Alexa-Fluor-647 phalloidin. Six representative images revealing the distribution of F-actin in the sperm head are shown (n=13). The 3D-reconstruction is colored according to the localization height as indicated in the color map.

not been previously reported. Interestingly, it has been shown that actin forms helix-like structures in the flagellum of the protozoan intestinal parasite *Giardia intestinalis* [69]. These findings open the question whether, to some extent, flagellar helical structures are conserved among diverse species.

Previous works have shown the existence of a dense cytoskeletal structure in the midpiece that is associated with mitochondria; however, the composition of this structure has remained unknown [70, 71]. Our results place actin and its related proteins as potential components of this cytoskeletal structure. In various cell types, actin-dependent immobilization of mitochondria is critical for localization of these organelles at sites of high ATP utilization [72]. Our results suggest that the presence of F-actin structures in the midpiece is associated with the integrity of the mitochondrial sheath and the localization of mitochondria. The actin cytoskeleton could be involved in the migration of mitochondria to the midpiece during spermiogenesis and in providing a scaffold that confines mitochondria in this cellular compartment. In support of this hypothesis, genetically modified male mice lacking the actin-interacting protein nectin-2 have an unorganized mitochondrial sheath and F-actin is absent from the sperm midpiece [42]. These mice are infertile and, although sperm motility appeared to be normal, long term periods of incubation in capacitating medium led to a loss of motility in vitro and reduced migration of the sperm into the oviduct in vivo [73]. These results highlight the importance of the actin cytoskeleton in the midpiece for normal sperm function and fertility.

To have a more comprehensive understanding of the actin cytoskeletal architecture in the midpiece, we evaluated the presence and localization of the actin-associated proteins spectrin and adducin. Spectrin is a protein of high molecular mass that is part of the cortical skeleton [74]. Spectrin reversibly unfolds and refolds when subjected to forces up to 20 pN [75], acting as a molecular spring and dramatically altering the elasticity of actin-spectrin meshwork. Spectrin has been previously described in the sperm of guinea pig and bovines, where it localizes in the sperm head acrosome and along the flagellum [76, 77]. In the present work, we find that spectrin localizes in the head and flagellum of mouse sperm. In addition, our super-resolution imaging indicates

that spectrin localizes close to the flagellum plasma membrane. Before acquiring fertilization competence, sperm change their motility pattern from progressive to hyperactivated motility [78]. Hyperactivation consists of highly asymmetrical waveforms of the tail combined with an increase in the amplitude of the flagellar bending [79]. Therefore, during hyperactivated motility the sperm midpiece experiences severe bending [30]. Taking into consideration the elastic properties of spectrin, we hypothesize that this protein reinforces the structure of the mitochondrial sheath and gives the midpiece the required elasticity during sperm hyperactivation. Rigid midpieces lead to male infertility due to failure in the acquisition of hyperactivated motility [80], which emphasizes the importance of an elastic midpiece structure for sperm function. Adducin is an actin-capping protein that promotes the binding of F-actin to spectrin [81]. We found that adducin is present in mouse sperm and is localized in the acrosome as well as in the tail. Unlike what was seen for the F-actin and spectrin structure found in the midpiece, adducin presented a dotted distribution in this region. This discrete localization found at the same radius as F-actin, and close to the radius of spectrin in the midpiece suggests that adducin might be linking the F-actin and spectrin structures observed in the midpiece (see model in Fig. 2.10(A)). In contrast, the organization of these three proteins in the principal piece follows a nesting localization, shaped as a matryoshka doll: moving outwards from the axoneme to the plasma membrane, we encounter first F-actin, then an adducin shell and finally a spectrin shell (see model in Fig. 2.10(B)). Even though the localization of actin overlaps with both the localizations of spectrin and adducin in the principal piece, adducin does not appear to have any substantial overlap with the spectrin signal in this region. The separation between the adducin and spectrin localization in the principal piece contrasts the localization overlap in the midpiece and further highlights the differences between the actin-based cytoskeleton of these two domains.

In neurons, the cytoskeleton of axons is formed by periodical actin rings that intercalate with spectrin, and Na^+ channels localize following this underlying actin-spectrin-based cytoskeleton [51]. The sperm-specific CatSper Ca^{2+} channel complex organizes in four longitudinal backbones along the principal piece [62, 82]. Delocalization of these channels results in the impossibility

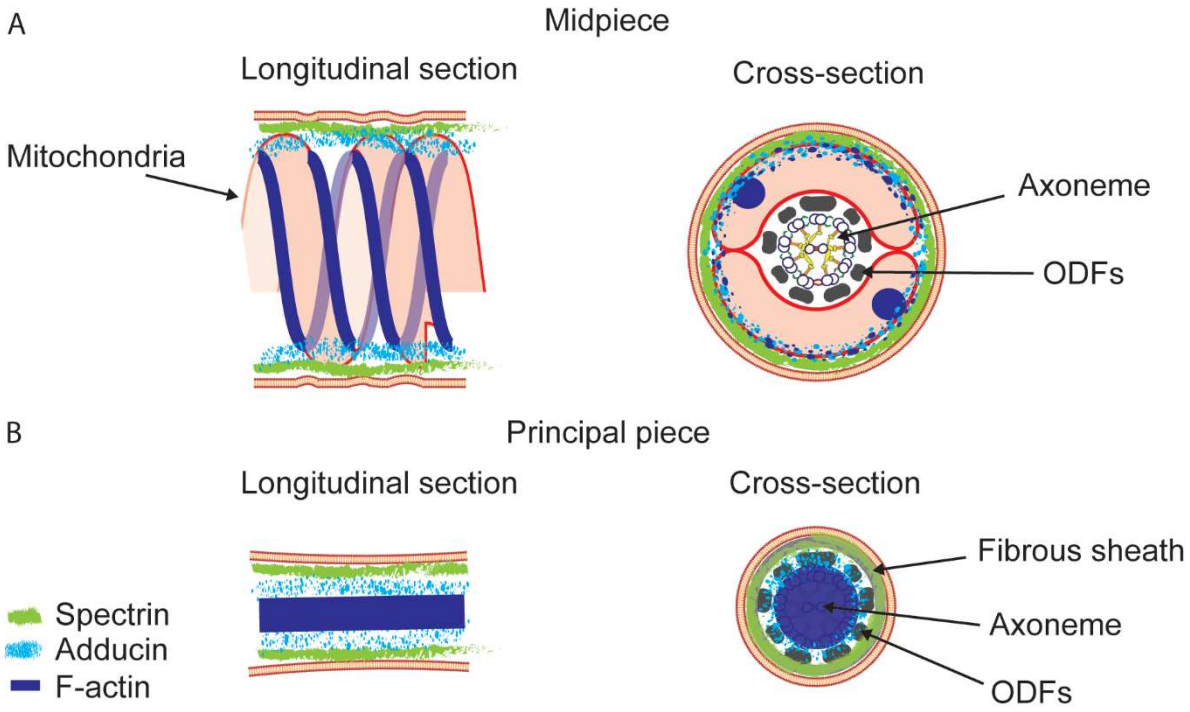

Figure 2.10: Schematic representation of the actin-based cytoskeleton in the mouse sperm flagellum. (A) Sketch of the localization of F-actin (blue), spectrin (green) and adducin (cyan) in a longitudinal section, and cross-section of the sperm midpiece. Midpiece structures such as the mitochondrial sheath, outer dense fibers (ODFs) and the central axoneme are indicated. (B) Sketch of the localization of F-actin (blue), spectrin (green) and adducin (cyan) in a longitudinal section and cross-section of the sperm principal piece. Principal piece structures such as the fibrous sheath, ODFs and the central axoneme are indicated.

of acquiring hyperactivated motility [62]. The actin-adducin-spectrin cytoskeleton of the sperm principal piece likely plays a role in maintaining highly organized structures by facilitating the arrangement of specific proteins in organized membrane domains, and thus regulating sperm function. During capacitation, the motility pattern of the sperm changes from progressive to hyperactivated [78]. Structural organization of ion channels and pumps is critical for the modulation of the dynamic processes associated with the acquisition of the asymmetrical hyperactivated motility [62].

In the same way that erythrocytes remain in the blood stream for long periods of time, sperm are exposed to different environments and can survive for days inside the female reproductive tract prior to fertilization. The structures of F-actin, spectrin and adducin suggest a role of these proteins in maintaining sperm integrity, elasticity and cell homeostasis. In line with these functions, it has been shown that mouse sperm present resistance to swelling in hypoosmotic media due to the presence of F-actin in the sperm tail [83]. The actin cytoskeleton of the principal piece could contribute to the resistance to osmotic stress.

Despite the relevance of the actin cytoskeleton in the regulation of cell physiology, its role in sperm function and its relationship with other capacitation-induced signaling processes are not well understood. In the present work, we showed that compartments of the sperm flagellum present different F-actin, adducin and spectrin organization. This highly organized cytoskeleton is expected to play a critical role in sperm function and fertility.

2.4 Materials and Methods

2.4.1 Animals and sample collection

Young adult (7-8 weeks old) CD-1 male retired breeders were purchased from Charles River Laboratories (Wilmington, MA). Genetically modified LifeAct-GFP-expressing mice were kindly donated by Santiago Di Pietro (Department of Biochemistry and Molecular Biology, Colorado State University, USA).

Animals were used and euthanized in accordance with the Animal Care and Use Committee (IACUC) guidelines of University of Massachusetts Amherst and Colorado State University. Two cauda epididymides were dissected, slightly cut and placed into 1 ml modified Krebs-Ringer medium [TYH's HEPES-buffered medium with composition: NaCl (100 mM), KCl (4.7 mM), KH_2PO_4 (1.2 mM), $MgSO_4$ (1.2 mM), glucose (5.5 mM), pyruvic acid (0.8 mM), $CaCl_2$ (1.7 mM) and HEPES (20 mM)]. Sperm were allowed to 'swim out' for 10 min at 37°C, and then the epididymides were removed and the suspension of sperm was adjusted to a final concentration of 1×10^7 - 2×10^7 cells/ml.

2.4.2 Indirect immunofluorescence

After collection, sperm were centrifuged at 800 g for 5 min, washed with 1 ml PBS, and centrifuged again at 800 g for 5 min. Sperm were fixed in solution by adding 4% (v/v) fresh PFA (paraformaldehyde) in PBS for 10 min at room temperature. Then sperm were centrifuged at 800 g for 5 min, washed with 1 ml PBS, centrifuged again at 800 g for 5 min and resuspended in 500 μl PBS. Sperm were seeded in poly-lysine-coated coverslips (Corning #1.5) and left to air dry. Non-bound cells were removed by washing with PBS. After that, cells were permeabilized with 0.5% (v/v) Triton X-100 in PBS for 5 min at room temperature and washed three times for 5 min with 0.1% (v/v) Tween-20 in PBS (T-PBS). Samples were blocked with 3% (w/v) BSA in T-PBS for 1 h at room temperature and then incubated with anti-spectrin antibody s-1515 (1:25), anti-spectrin antibody s-1390 (1:50; Fig. S1) or anti-adducin antibody (1:100) diluted in T-PBS containing 1% (w/v) BSA overnight at 4°C in a humidifier chamber. After incubation, sperm were washed three times for 5 min with T-PBS and incubated with the corresponding Alexa Fluor 488-conjugated secondary antibody (1:200) diluted in T-PBS containing 1% (w/v) BSA for 1 h at room temperature. Finally, samples were washed three times for 10 min with T-PBS and the coverslips were mounted using Vectashield H1000 (Molecular Probes, Eugene, OR). Epifluorescence microscopy was performed using a TE300 Eclipse microscope (Nikon) with an oil immersion objective (Nikon,

60ÃŮ, NA 1.4) coupled with a CMOS camera (Zyla 4.2, Andor, Belfast, UK). Negative controls using secondary antibody alone were used to check for specificity.

2.4.3 STORM sample preparation

For spectrin and adducin labeling, samples were fixed and incubated with primary antibody as described above for indirect immunofluorescence. After primary antibody incubation, cells were washed with T-PBS three times for 5 min each, and then incubated with Alexa Fluor 647-conjugated anti-rabbit-IgG secondary antibody diluted in PBS containing 1% (w/v) BSA (1:1000) for 1 h at room temperature. Cells were then washed with T-PBS three times for 5 min each. After washing, cells were immediately mounted in STORM imaging buffer [50 mM Tris-HCl pH 8.0, 10 mM NaCl, 0.56 mg/ml glucose oxidase, 34 μg/ml catalase, 10% (w/v) glucose, and 1% (v/v) β-mercaptoethanol]. For phalloidin labeling, sperm samples were seeded in poly-lysine-coated.

coverslips (Corning #1.5) and left to air dry for 15 min. Then, samples were fixed and permeabilized with 0.3% (v/v) glutaraldehyde in 0.25% (v/v) Triton X-100 in CB [Cytoskeleton buffer; MES (10 mM, pH 6.1), NaCl (150 mM), EGTA (5 mM), glucose (5 mM), and MgCl2 (5 mM)] for 1 min. Cells were then washed with CB buffer three times for 5 min each, and then incubated with 2% (v/v) glutaraldehyde in CB buffer for 15 min. Then cells were washed with CB buffer twice for 10 min each. To avoid background fluorescence caused by glutaraldehyde fixation, samples were incubated with 0.1% (w/v) sodium borohydride in PBS for 7 min. After that, samples were washed with PBS twice for 5 min each, and incubated with 0.5 μM of Alexa Fluor 647-conjugated phalloidin in PBS for overnight at 4°C in a humidifier chamber. Cells were then washed with PBS.

2.4.4 3D STORM imaging

Images were acquired using Nikon NIS-Elements 4.51 software in a custom built microscope equipped with an Olympus PlanApo 100× NA1.45 objective and a CRISP ASI autofocus system [84, 85]. Alexa Fluor 647 was excited with a 638-nm laser (DL638-050, CrystaLaser, Reno, NV) under continuous illumination. Initially the photoswitching rate was sufficient to provide a

substantial fluorophore density. However, as fluorophores irreversibly photo-bleached, a 405-nm laser was introduced to enhance photo-switching. The intensity of the 405-nm laser was adjusted in the range 0.01-0.5 mW to maintain an appropriate density of active fluorophores. Axial localization was achieved via astigmatism using a MicAO 3DSR adaptive optics system (Imagine Optic, Orsay, France) inserted into the emission pathway between the microscope and the EMCCD camera [36, 86]. This technology achieves three-dimensional localization via shaping the axial point spread function, allowing both the correction of spherical aberrations and the introduction of astigmatism. User-controlled introduction of astigmatism enabled the accurate detection of single molecules over a thickness of 1 μm and, in turn, 3D reconstruction [87]. A calibration curve for axial localization was generated with 100-nm TetraSpeck microspheres (Invitrogen) immobilized on a coverslip [34]. The images were acquired in a water-cooled, back-illuminated EMCCD camera (Andor iXon DU-888) operated at -85°C at a rate of 50 frames/s; 50,000 frames were collected to generate a super-resolution image.

2.4.5 Super-resolution image reconstruction

Single-molecule localization, drift correction using image cross correlation and reconstruction were performed with ThunderSTORM in ImageJ [38].

2.4.6 Image analysis

To find the molecular radial distributions, we selected regions of interest of the flagellum that were found to lie in a straight line. The center of the flagellar cross-section was first found by Gaussian fitting or Center of Mass circular fitting of the localizations histograms along x and y. The coordinates of the localized molecules were then transformed into cylindrical coordinates to obtain the radial position r and azimuth angle θ.

2.4.7 Atomic force microscopy

Sperm cells were placed in poly-lysine-coated glass-bottom petri dishes and mounted in PBS. AFM measurements were performed in a Bruker Resolve SPM system using the ScanAsyst mode with a ScanAsyst-Fluid+ probe (Bruker, Billerica, MA).

2.4.8 Transmission electron microscopy

Luminal fluid collected from cauda epididymides of two mice was pooled and fixed in 2% (v/v) glutaraldehyde in 0.1 M sodium cacodylate and post-fixed in osmium tetroxide. Samples were embedded in Poly/Bed812 (Polysciences; Warrington, PA). 1-μm-thick sections were cut and stained with Toluidine Blue for initial light microscopic examination and to locate areas for ultrastructural evaluation. Thin sections (60-80 nm) were cut from the identified areas, stained with uranyl acetate and lead citrate, and evaluated using a JEOL JEM 1200EX transmission electron microscope.

Chapter 3

The spatial dynamics of PKA and the revelation of its downstrean tyrosine kinase identity

3.1 Introduction

[2] Mammalian sperm require two post-testicular maturation steps to become fertile: epididymal maturation, occuring in the mail epididymis, and capacitation, occuring after ejaculation in the female tract. This process is associated with changes in the sperm motility patten known as hyperactivation, and with the preparation to undergo the acrosome reaction, and exocytotic process, upon exposure to physiological agonists [19]. Capacitation is a highly complex process orchastrated by PKA activity [2]. Its activation appears to be necessary for :1) membrane potential (*Em*) hyperpolarization [22, 89], which originates after 15 - 30 min; 2) development of hyperactivated motility after 30 - 45 min; and 3) triggering of the acrosome reaction, once capacitation is complete, *i.e.* after 60 min for mouse sperm. Even though these processes differ in their kinetics, all of them involve phosphorylation cascades initiated by PKA. Moreover, one of the first signaling pathways observed during capacitation is the HCO_3^--dependent stimulation of cAMP synthesis, which rapidly activates PKA [90].

[2]The work presented in this chapter has two parts. Part one has been performed in collaboration with Cintia Stival, Carla Ritagliati, Carolina Baró Graf, Prof. Dario Krapf (Instituto de Biología Molecular y Celular de Rosario, Rosario, Argentina), Dr. María Gracia Gervasi, Prof. Pablo Visconti (University of Massachusetts, Amherst), Dr. Guillermina M. Luque, Dr. Nicolas Torres, Prof. Mariano Buffone (Instituto de Biología y Medicina Experimental, Buenos Aires, Argentina) and José Luis De la Vega-Beltrán and Prof. Alberto Darszon (Universidad Nacional Autónoma de México (UNAM), Cuernavaca, Morelos, México). I contributed the work with super-resolution imaging of PKA and GLUT3. Part two has been performed in collaboration with Antonio Alvau, Dr. María Gracia Gervasi, Felipe A. Navarrete, Prof. ANa Maria Salicioni, Prof. Pablo Visconti (University of Massachusetts, Amherst), Maria Agustina Battistone, Dr. Vanina G. Da Ros, Prof. Patricia S. Cuasnicu (Instituto de Biología y Medicina Experimental, Buenos Aires, Argentina), Claudia Sánchez-Cárdenas, José Luis De la Vega-Beltrán, Prof. Alberto Darszon (Universidad Nacional Autónoma de México (UNAM), Cuernavaca, Morelos, México) and Prof. Peter A. Greer (QueenâĂŹs University, Kingston, Ontario, Canada). I contributed the work with super-resolution imaging of FER and pY. This chapter has been published in Journal of Biological Chemistry and Development [61, 88].

As a promiscuous Ser/Thr kinase, PKA, its precise activation at specific localizations known as discrete PKA signalosomes, is necessary [91]. However, PKA localization can vary over time, and these changes have been proposed to regulate different processes [92, 93]. PKA associates to cellular structures through AKAPs (A-kinase anchoring proteins), which form scaffolding assemblies that play a pivotal role in PKA regulation. AKAPs restrict PKA activity to specific microdomains dependent on the regulation of PKA-AKAP interaction. Most AKAPs also anchor other signaling enzymes such as cyclic nucleotide phosphodiesterases that degrade cAMP and allow PKA activation to be locally regulated in amplitude and duration. Synthetic peptides bearing an amphipathic helix domain that interacts with PKARII (PKA regulatory II subunits) impair PKA binding to AKAPs [94]. These peptides, commonly used as tools to disrupt subcellular PKA localization, contain an N-terminal modification with a stearic acid moiety that confers membrane permeability. One example of this type of amphipathic peptide is sHT31, a 24-residue peptide that binds to PKARII with high affinity [94] preventing their interaction with AKAPs.

In the first part of this chapter, 3D STORM was applied to study spatial distribution of PKA catalytic subunit α (cPKA, also known as PRKACA2) in mouse sperm. We observed that upon capacitation, the catalytic subunit redistributed within the flagellum. This movement was completely abrogated when sperm were exposed to sHT31.

Meanwhile, as addressed earlier, the increase in cAMP stimulates PKA, which activates a series of pathways and coincides with increased protein tyrosine phosphorylation [95]. Since the first reports in 1995 [23, 96], the increase in tyrosine phosphorylation has been used as an endpoint of capacitation in sperm from many species [97–102]. However, the identity of the protein tyrosine kinase(s) responsible for this signaling event has remained elusive. A list of potential candidate kinases has emerged based on pharmacological and immunological evidence. Among these candidates, the most relevant were SRC [103–105], FYN [106], ABL [107], and both members of the FAK (focal adhesion kinase) family, FAK and proline-rich tyrosine kinase 2 (PYK2; also known as PTK2B) [108, 109]. All these enzymes were shown to be present in sperm and, furthermore, the increase in tyrosine phosphorylation was reduced or completely obliterated when treated with

inhibitors against their respective activities. Pharmacological inhibitors can be excellent tools to intervene in particular cellular processes with accurate temporal precision. However, small molecule inhibitors often have off-target effects that confound identification of candidate enzymes involved in specific processes. Therefore, to identify conclusively the tyrosine kinase(s) responsible for capacitation, genetic approaches are preferred.

Among the candidates, FER has been recently shown to be phosphorylated on tyrosine residues during capacitation [62]. In the second part of this chapter, we have confirmed the true identity of tyrosine kinase to be FER from the structural localization point of view, together with the collaborated work with Dr. Visconti's group.

3.2 Results

3.2.1 PKA localization changes revealed by super-resolution imaging

To analyze PKA localization dynamics during capacitation, 3D STORM was used, enabling the study of spatial distribution of PKA catalytic subunit $\alpha 2$ (cPKA, also known as PRKACA2) in mouse sperm, which allows 3D reconstruction with resolution of $\sim$20 nm [110, 111], to study protein distribution within the narrow sperm tail, which is less than 1 μm in diameter. The spatial distribution of cPKA was determined in both noncapacitated and capacitated sperm. As shown in Fig. 3.1(A), noncapacitated sperm exhibited a dense and compact rod-like radial distribution of cPKA. The facilitative GLUT3 (glucose transporter 3), which is present throughout the flagellar plasma membrane [112], showed a continuous ring staining cross-section. This was used as a control, showing a distribution compatible with previous reports [62] (Fig. 3.1(A),(B)) and validating the structural information obtained by 3D STORM.

Interestingly, upon capacitation, cPKA localized to a broader cylinder-like distribution. Fig. 3.1(B) shows the radial localization of cPKA in capacitated and noncapacitated sperm as well as the distribution of GLUT3. The distribution of cPKA in sperm incubated in capacitating media showed a shoulder at $\sim$110 nm that was not present in noncapacitated sperm. Fig. 3.1(C) shows the distribution of cPKA for individual cells that were incubated only in capacitating media, where

the effect is much more evident. As already reported, sperm in capacitating conditions consist of two heterogeneous populations [113], half of the cells capacitated and exhibited a distribution shift from 70 to 110 nm, whereas the other half of the cells showed a distribution of cPKA that is not distinguishable from the cells in noncapacitating media. Addition of 1 μM sHT31 to capacitated sperm promoted a retraction of cPKA to its original dense and compact rod-like radial distribution, clearly showing by microscopy for the first time that disruption of PKA-AKAP interaction alters PKA localization (Fig. 3.1(D)). To further confirm sHT31 as a disruptor of PKA-AKAP interaction, PKARII immunoprecipitations from capacitated sperm in the absence or presence of sHT31 were performed. This experiment done by Dr. Krapf's lab aimed to analyze whether PKARII pulls down AKAP4, the most abundant AKAP in the principal piece where PKA localizes. As shown in Fig. 3.1(E), the amount of AKAP4 that co-immunoprecipitates with PKARII was reduced in the presence of sHT31 (Fig. 3.1(E)), further supporting that sHT31 disrupts PKA-AKAP interaction [88].

3.2.2 The identification of tyrosine kinase responsible for tyrosine phosphorylation

A commercially available inhibitor of PYK2 tyrosine kinase, PF431396, has been used to show that it blocks the capacitation-associated increase in tyrosine phosphorylation. Yet, sperm from Pyk2$^{-/-}$ mice (genetically modified PYK2 knock-out mice) displayed a normal increase in tyrosine phosphorylation, implying that PYK2 is not responsible for this phosphorylation process. Meanwhile, PF431396 has been shown that it can also inhibit FER, a tyrosine kinase known to be present in sperm. Moreover, sperm from mice targeted with a kinase-inactivating mutation in FER (Fer$^{DR/DR}$) failed to undergo capacitation-associated increases in tyrosine phosphorylation [61]. Those loss-of-function experiments, on top of the small molecule inhibitor, have been performed by our collaborator, Dr. Visconti's group, laying the groundwork for us to look into the spatial relation between FER and tyrosine phosphorylation with 3D STORM, by which the localization of proteins phosphorylated on tyrosine residues has been accurately measured. The

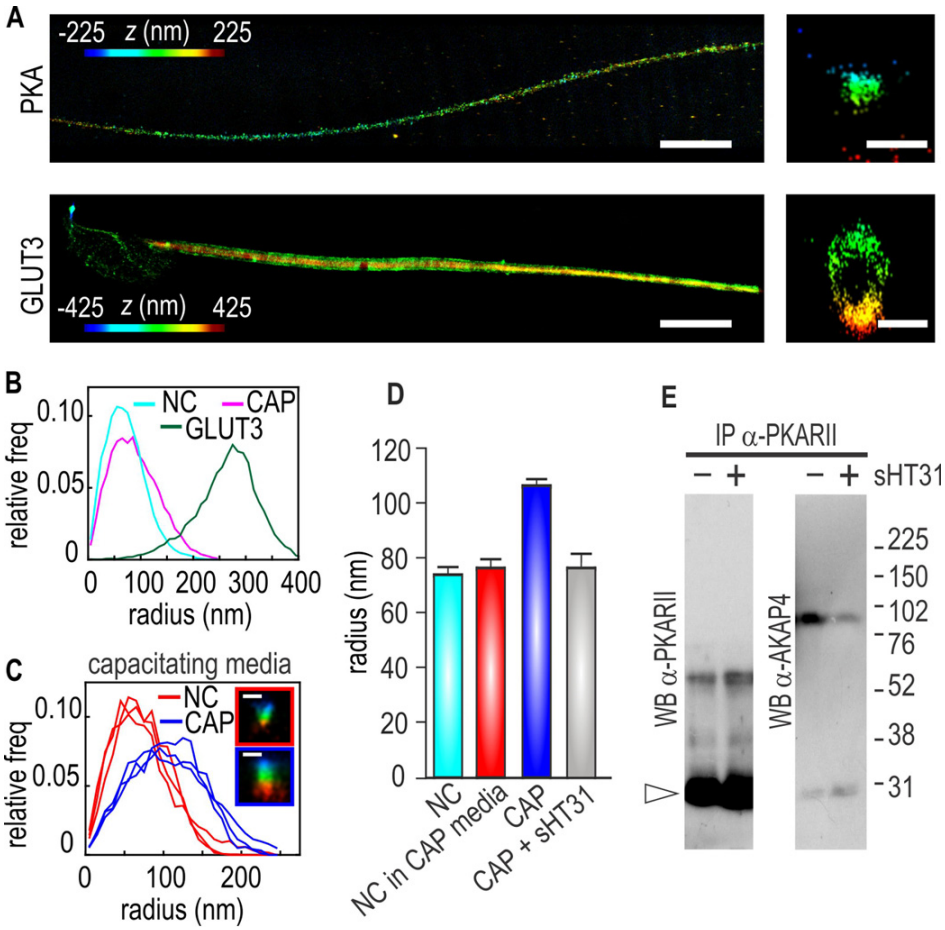

Figure 3.1: Redistribution of cPKA in mouse sperm during capacitation. (A) Representative color-coded 3D STORM reconstructions of cPKA in the principal piece and GLUT3 in the flagellum and head of capacitated cells. Scale bars: 5 μm. Right panels show the corresponding Y-Z cross-sections of the 3D STORM reconstructions. Scale bars: 500 nm. (B) Averaged radial distributions of cPKA localization in the principal piece under capacitating (CAP, cyan, n=6) and noncapacitating (NC, pink, n=6) conditions, as well as GLUT3 localization (green). (C) Radial distributions of cPKA in six individual cells under capacitating conditions, where three of them (red) show a distribution similar to noncapacitated (NC) cells and three show a significant shift (blue, CAP). See inserts for Y-Z cross-sections of representative 3D STORM reconstructions, scale bars: 200 nm. (D) Mean radius of cPKA localization in cells incubated in noncapacitating (NC) and capacitating media in the absence (CAP) or presence (CAP+ sHT31) of sHT31. Red bar represents mean radius of cPKA of cells that were incubated in capacitating conditions but PKA did not redistribute (red trace of C) (NC in CAP media). (E) Protein extracts from sperm incubated in capacitating conditions in the absence (-) or presence (+) of 3 μM sHT31 were subjected to immunoprecipitation with α-PKARII antibodies performed by Dr. Dario Krapf's group. Immunoprecipitates were analyzed by Western blots with α-PKARII (left panel) and α-AKAP4 (right panel) antibodies. The arrowhead indicates the IgG light chain [88].

measurements indicated that in the principal piece, tyrosine phosphorylation is confined to the axoneme of the sperm flagellum. Similarly, we used 3D STORM to evaluate the spatial distribution of FER within the sperm flagellum. FER was found throughout both the midpiece and principal piece (Fig. 3.2(A)). Cross-sections of the images indicated that in the midpiece, FER localized within 250 nm from the center (Fig. 3.2(B)). In the principal piece, FER had a spatial distribution restricted to the axoneme (Fig. 3.2(C)). A similar spatial distribution was observed for tyrosine phosphorylation in both sections of the flagellum (Fig. 3.2(D)-(F)). The coincident radius in the radial distributions of both signals shows that FER localization overlaps with the localization of tyrosine phosphorylation in both compartments of the sperm flagellum (Fig. 3.2(G),(H)), which answers the hypothesis that they should be in the very close proximity if they interact with each other and further confirms that FER is the real player behind the tyrosine phosphorylation.

3.3 Discussion

For many years, it has been accepted that molecules involved in cAMP signaling (*i.e.* phosphodiesterases and adenylyl cyclases), as well as its effectors and targets are carefully compartmentalized in sperm [2]. This compartmentalization helps assure a tight regulation of different sperm processes associated with capacitation. Biochemical immunolocalizations, supported by enzymatic assays, have conclusively demonstrated that PKA in mouse sperm is restricted to the flagellum [114]. Further subcompartmentalization would be allowed by local cAMP generation within independently regulated microdomains. These cAMP modules could be in turn modulated by AKAPs, which dock not only PKA but also enzymes and substrates to specific cell locations [115].

Mice sperm are endowed with the sperm-specific catalytic PKA subunit Cα2 [116], lacking myristoylated PKA catalytic subunit Cα1 [117], which targets to the plasma membrane. Absence of this isoform abolishes canonical PKA signaling events on the membrane. Then, it is possible that anchoring of PKA to different AKAPs restricts the activity of Cα2 to specific locations. Using 3D STORM we show that in noncapacitated sperm, inactive cPKA localizes to a narrow compact

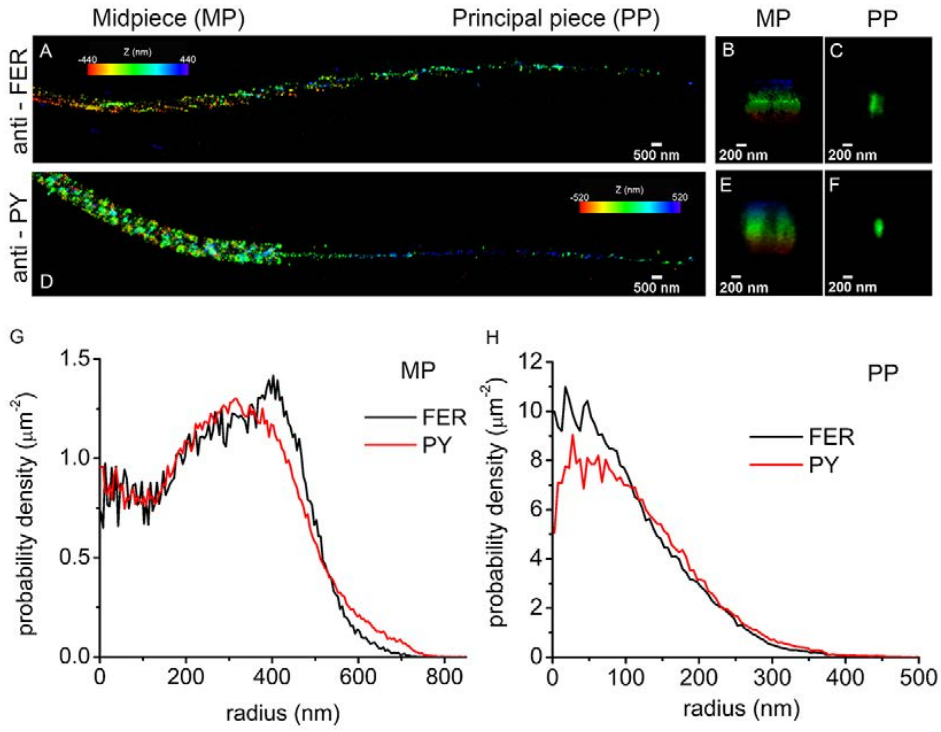

Figure 3.2: Localization of FER and tyrosine-phosphorylated proteins in mouse sperm by STORM. (A) 3D STORM images of FER in x-y projection. The color represents the relative distance from the focal plane along the z-axis. (B) FER localization in the midpiece (MP), y-z projection. (C) FER localization in the principal piece (PP), y-z projection. (D) 3D STORM images of tyrosine phosphorylation (pY) in x-y projection. The color represents the relative distance from the focal plane along the z-axis. (E) Tyrosine-phosphorylated protein (PY) localization in the MP, y-z projection. (F) Tyrosine-phosphorylated protein (PY) localization in the PP, y-z projection. (G) Radial distribution of FER and PY in the MP. (H) Radial distribution of FER and PY in the PP. Images are representative of 15 cells from three different animals for PY analysis and of nine cells from three different animals for FER analysis.

rod along the flagellum with a mean radius of 70 nm. However, after capacitation, cPKA acquired a mean radius of 105 nm. Upon disruption of the PKA-AKP interaction with sHT31 in capacitated sperm, the cPKA subunit returned to it original location, indicating that PKA anchoring to AKAP is required for re-localization of the enzyme throughout capacitation. This represents the first clear evidence that PKA localization changes during this process.

In the last 20 years, tyrosine phosphorylation has been used as a marker of capacitation in sperm from mouse and other species. Capacitation is defined as all biochemical and physiological processes that render the sperm able to fertilize [27]. We successfully evaluated the role of FER in the capacitation-associated increase of tyrosine phosphorylation through biochemical assays, which was corroborated by 3D-STORM microscopy, using anti-phosphotyrosine and anti-FER antibodies and showing consistent spatial distributions in both mid- and principal piece in capacitated sperm flagella. As $\text{Fer}^{DR/DR}$ mice are viable and fertile [118], our findings suggested that, at least in mouse sperm, the capacitation-associated increase in tyrosine phosphorylation is not required for *in vivo* fertilization. However, our *in vitro* results do not exclude the possibility that during natural mating, interactions between sperm and the female environment compensate for the lack of FER. Despite these results, $\text{Fer}^{DR/DR}$ sperm are less able to fertilize *in vitro*. Interestingly, mice lacking CRISP1 (cysteine-rich secretory protein 1) exhibited a similar phenotype. CRISP1 is expressed by the epididymal epithelium, secreted and incorporated into sperm during epididymal maturation [119]. Although these mice are fertile in vivo, their capacitated sperm have significantly lower levels of tyrosine phosphorylation in vitro [120]. Both $\text{Crisp1}^{-/-}$ and $\text{Fer}^{DR/DR}$ sperm exhibit reduced *in vitro* fertilization rates, suggesting that the functional role of tyrosine phosphorylation *in vivo* can be bypassed by yet undiscovered mechanisms. The finding that tyrosine phosphorylation plays a role in *in vitro* fertilization, together with results showing that the increase in tyrosine phosphorylation during capacitation is conserved in a variety of mammalian species, suggests that this signaling pathway could play a role in species in which sperm competition is relevant. However, direct evaluation of this hypothesis requires further investigation.

Chapter 4

The subcellular localization of CDC42 in relation to sperm calcium specific channel CatSper

4.1 Introduction

[3] Sperm acquire the ability to fertilize in the female genital tract in a process called capacitation [121, 122]. From a molecular point of view, bicarbonate (HCO_3^-) and calcium (Ca^{2+}) stimulation of the SACY leads to an increase in cAMP, PKA activity and tyrosine phosphorylation of sperm proteins [23, 61, 96].

During capacitation sperm sense the environment and undergo a change in the motility pattern called hyperactivation, which is critical for fertilization [123]. This high-amplitude, whip-like beating pattern of the flagellum enables sperm to migrate through the female tract and to overcome the oocyte surrounding layers [124, 125].

Ca^{2+}, the primary second messenger that triggers hyperactivation, enters sperm through the sperm-specific CatSper channel complex [126]. This complex comprises four homologous α subunits (CatSper 1-4) [127, 128] and auxiliary subunits: CatSper β, CatSper γ, CatSper δ [129–131], and the more recently described CatSper ξ and CatSper ζ [82]. CatSper proteins are encoded by multiple testis-specific genes and localized in the plasma membrane of the principal piece of mature sperm [132, 133], except for CatSper ζ which is a small soluble protein [82]. Mice lacking any of the CatSper1-4 genes as well as human males with CatSper loss-of-function mutations [134–136] are infertile and their sperm are unable to hyperactivate [115, 126, 130, 137]. In

[3]The work presented in this chapter has been performed in collaboration with Dr. Guillermina M. Luque, Dr. Nicolás Gilio, Dr. Tomás Dalotto-Moreno, Prof. Mariano Buffone (Instituto de Biología y Medicina Experimental, Buenos Aires, Argentina), Dr. Ana Romarowski, Dr. María Gracia Gervasi, Prof. Pablo Visconti (University of Massachusetts, Amherst), Gerardo Orta, José Luis De la Vega-Beltrán and Prof. Alberto Darszon (Universidad Nacional Autónoma de México (UNAM), Cuernavaca, Morelos, México), Cintia Stival and Prof. Dario Krapf (Instituto de Biología Molecular y Celular de Rosario, Rosario, Argentina). I contributed super-resolution imaging work. This chapter is in preparation for submission.

mammalian species, CatSper is differentially regulated by various compounds, such as steroids, prostaglandins, endocannabinoids, and intracellular pH (pH_i). Both human and mouse CatSper channels are activated by intracellular alkalinization [138, 139]. However, human CatSper activation can also be stimulated by other ligands like progesterone and prostaglandins [140], while mouse CatSper activity does not appear to be controlled by these compounds [141]. This may indicate species-specific adaptations of sperm to adjust to a distinct set of activators within the female reproductive tract [142].

With the exception of intracellular alkalinization and activation of PKA [143], little is known about the endogenous regulation of CatSper. By using 3D STORM, it was recently reported that CatSper proteins form a unique pattern of four linear "stripes" in the plasma membrane close to the fibrous sheath, along the principal piece of the flagellum [62, 82]. This segregated localization of proteins in the tail may provide the structural basis for the selective activation of CatSper and the normal development of motility. For example, recent super-resolution microscopy experiments in human sperm revealed that Hv1, the voltage-gated proton channel involved in cytoplasmic alkalinization, is distributed asymmetrically within bilateral longitudinal lines and that inhibition of this channel leads to a decrease in sperm rotation along the long axis [144]. In addition, other Ca^{2+} signaling molecules such as Caveolin-1, P-CaMKII (phosphorylated Ca^{2+}/calmodulin-dependent protein kinase II) and calcineurin (PPP3C aka PP2B) colocalize with CatSper displaying a similar spatial distribution along the principal piece in mouse sperm. Only CatSper has been shown to be critical for this segregated localization since CatSper-null mice did not display the four-column organization of these signaling molecules [62]. The mechanism by which these proteins interact and modulate CatSper function is still unknown. Thus, the characterization of this molecular complex is essential to understand the regulation of CatSper channels.

In the present work we report that, similar to CatSper, the small GTPase Cdc42 distribution in the principal piece is confined to four linear domains. Moreover, we also showed that Cdc42 is delocalized in sperm from CatSper KO (knockout) mice. Altogether, these data suggest that Cdc42 is involved in the regulation of Ca^{2+} influx in sperm through CatSper channels.

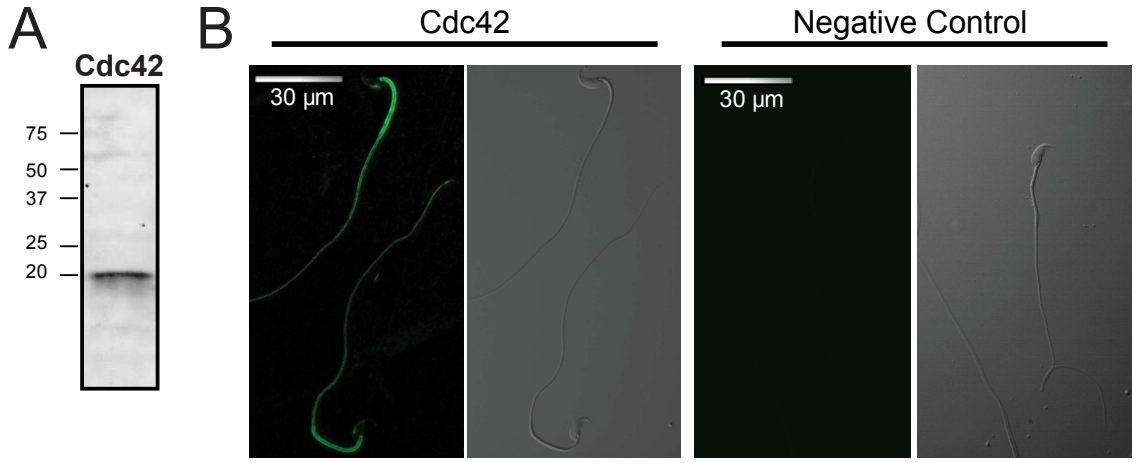

Figure 4.1: The presence of Cdc42 protein in mouse sperm examined by Dr. Buffone's group. Proteins (equivalent to 14 $\times 10^6$ sperm) were analyzed by 15% SDS-PAGE and immunoblotted using antibody against the small GTPase Cdc42. (B) Representative images of non-capacitated sperm stained with anti-Cdc42 antibody and negative control. Nonspecific staining was determined by incubating the sperm in the absence of primary antibody. An Alexa Fluor 488-conjugated goat anti-mouse was used (green) and analyzed by confocal microscopy. The corresponding phase-contrast micrographs are shown. Negative controls were performed incubating sperm with IgG.

4.2 Results

4.2.1 Cdc42 localized in four longitudinal lines along the flagellum resembling CatSper distribution pattern

For the starter, Dr. Mariano's group has verified the expression of Cdc42 in the mouse sperm. The presence of Cdc42 protein in mouse sperm was analyzed by western blotting using a specific antibody against the small GTPase. As shown in Fig. 4.1(A), a single band of the expected size for Cdc42 (21.3 kDa) was observed in mouse sperm. Immunofluorescence studies revealed the localization of Cdc42 is mainly along the flagellum as well as in the acrosome of mouse sperm (Fig. 4.1(B)).

To investigate the spatial distribution of Cdc42, 3D STORM was used, which allows 3D reconstruction with $\sim$20 nm resolution [34, 111], making it possible to study protein localization within the sperm flagellum, which is less than 1 μm in diameter. Similar to what was done by Chung et al., to calibrate our system, the localization of the axoneme, the fibrous sheath and the plasma membrane of mouse sperm were determined [62]. As controls, β-tubulin, AKAP4, and GLUT3,

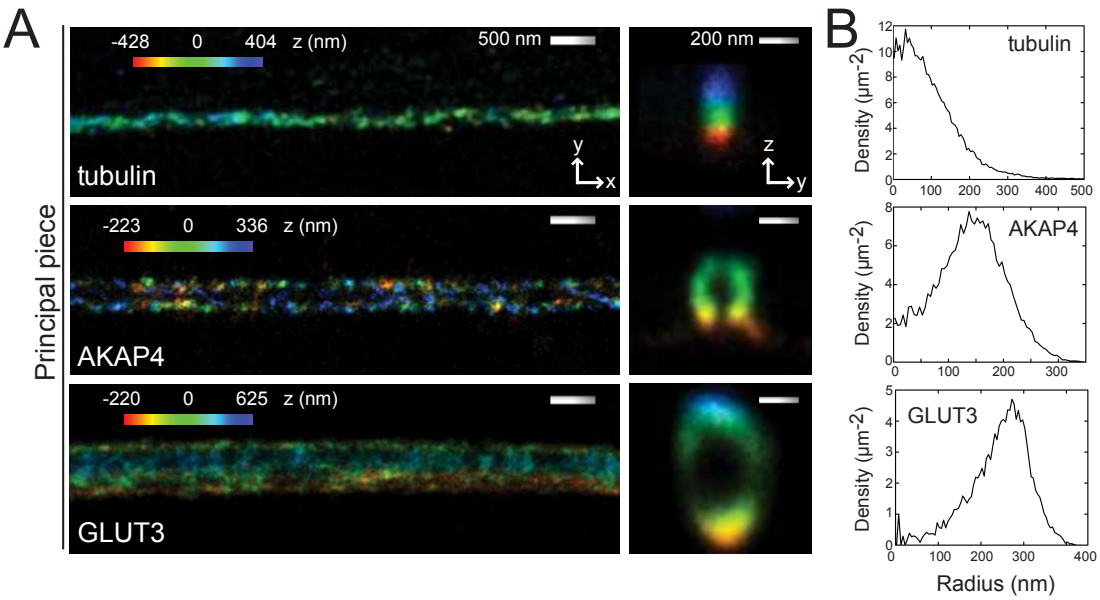

Figure 4.2: The structural information obtained by 3D STORM reproduced known protein localization in the sperm flagella. Sperm were incubated under non-capacitating (NC) conditions. Negative controls were performed incubating sperm with IgG. (A) 3D STORM images of principal piece for β-tubulin, AKAP4, and GLUT3. Left, x-y projections. Right, y-z cross-sections. (B) Radial profiles of immunostained density of β-tubulin, AKAP4, and GLUT3. The color in all x-y projections encodes the relative distance from the focal plane along the z axis.

well-known flagellar proteins, were immunolocalized with specific primary antibodies followed by Alexa647 conjugated secondary antibodies (Fig. 4.2).

Taking advantage of the cylindrical symmetry of the flagellum, the molecule localizations were converted into cylindrical coordinates $(r, \theta, z^{'})$ where $z^{'}$ represents the flagellum axis. In cartesian coordinates (x, y, z), z is the direction normal to the coverslip, so that in this coordinate system the sperm lies on the x,y plane as represented in Fig. 4.3(A). As expected, the spatial distribution of β-tubulin was axonemal and localized in the center of the flagellum, while AKAP4 localized in the fibrous sheath, and GLUT3 present throughout the flagellar plasma membrane, showed a continuous rim distribution in cross-section (Fig. 4.2, right panel). The radial distributions of β-tubulin, AKAP4 and GLUT3 in the principal piece showed that β-tubulin peaked at 23$\pm$2 nm (mean$\pm$standard error) from the center of the flagellum while AKAP4 and GLUT3 peaked at 146$\pm$1 nm and 269$\pm$1 nm, respectively (Fig. 4.2(B)). In all cases, these well studied sperm flag-

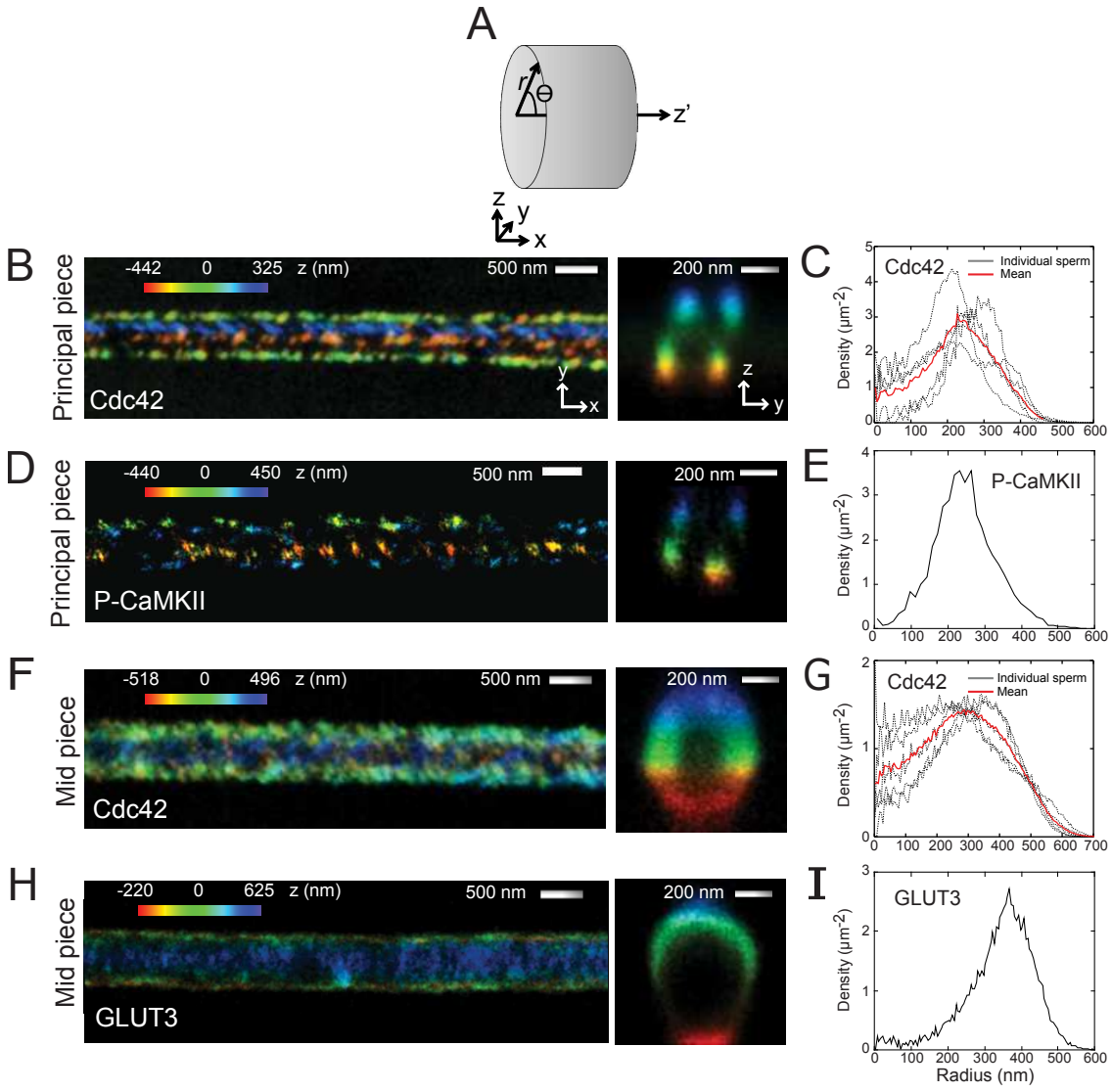

Figure 4.3: Cdc42 is localized in four longitudinal lines similar to those of the CatSper distribution. (A) Cartoon of the cylindrical coordinate system for defining the radius and angles of molecular coordinates in STORM images. The longitudinal axis (x) is placed at the flagellar center and the origin at the annulus. (B) Representative 3D STORM images showing the localization of Cdc42 in the sperm principal piece at x-y projection (left) and in y-z cross-section (right). (C) Radial profiles of Cdc42 localization in principal piece (n=4 sperm). (D) Representative 3D STORM images of principal piece P-CaMKII. Left, x-y projections. Right, y-z cross-sections. (E) Radial profiles of P-CaMKII localization in principal piece. (F) Representative 3D STORM images showing the localization of Cdc42 in the sperm mid piece at x-y projection (left) and in y-z cross-section (right). (G) Radial profiles of immunostained density of the sperm mid piece localized Cdc42. (H) Representative 3D STORM images of mid piece GLUT3. Left, x-y projections. Right, y-z cross-sections. (I) Radial profiles of immunostained density of GLUT3. The color in all x-y projections encode the relative distance from the focal plane along the z axis.

ellar proteins showed compatible distributions with previous reports [62], validating the structural information obtained by 3D STORM.

Mouse sperm exhibited a Cdc42 localization confined to four columns along the principal piece (Fig. 4.3(B)), which resembles the localization of CatSper in the same region [62]. On cross-sections of the flagellum, Cdc42 appeared as four tight puncta (Fig. 4.3(B), right panel). Similarly, P-CaMKII showed the CatSper-like distribution in the principal piece (Fig. 4.3(D)-(E) and Fig. 4.4(B)), as previously described [62]. The radial distributions of Cdc42 and P-CaMKII peaked at 238$\pm$16 nm and 235$\pm$2 nm respectively. These values are similar to those observed for GLUT3 (Fig. 4.2), indicating that both proteins localized close to the plasma membrane (Fig. 4.3(C) and (E)). A graphical representation of Cdc42 localization in terms of the azimuth angle θ vs. axial distance $z^{'}$ along the principal piece showed the four stripes along the flagellum as well as the 2D angular profiles of the surface localizations (Fig. 4.4(A)). This segregated localization of Cdc42 in the principal piece, disappeared in the flagellum midpiece, where a continuous ring staining was observed in the cross-section (Fig. 4.3(F)). The radial distribution in this section peaked at 281$\pm$25 nm (Fig. 4.3(G)) which is similar to GLUT3 in that region 323$\pm$2 nm (Fig. 4.3(H)-(I)).

Altogether, these results indicate that Cdc42 is organized in four columns in the principal piece and resembles the localization of CatSper and other signaling molecules reported in that structural domain.

4.2.2 Cdc42 delocalized in CatSper KO sperm

It has been shown that CatSper channel complex serves as an organizing structure for the four-line domains. In this respect, other molecules such as Caveolin-1 lost their localization when CatSper is abrogated [62]. Therefore, to test the extent by which Cdc42 is associated to this complex, its localization in sperm from CatSper-null mice was analyzed via western blotting and immunofluorescence imaging by Dr. Buffone's group. Levels of protein expression in CatSper KO sperm were examined (Fig. 4.5(A)). Expression of Cdc42 was detected in CatSper KO, albeit at 50% lower levels than in WT (wild type) sperm (Fig. 4.5(A), right panel). Immunofluorescence

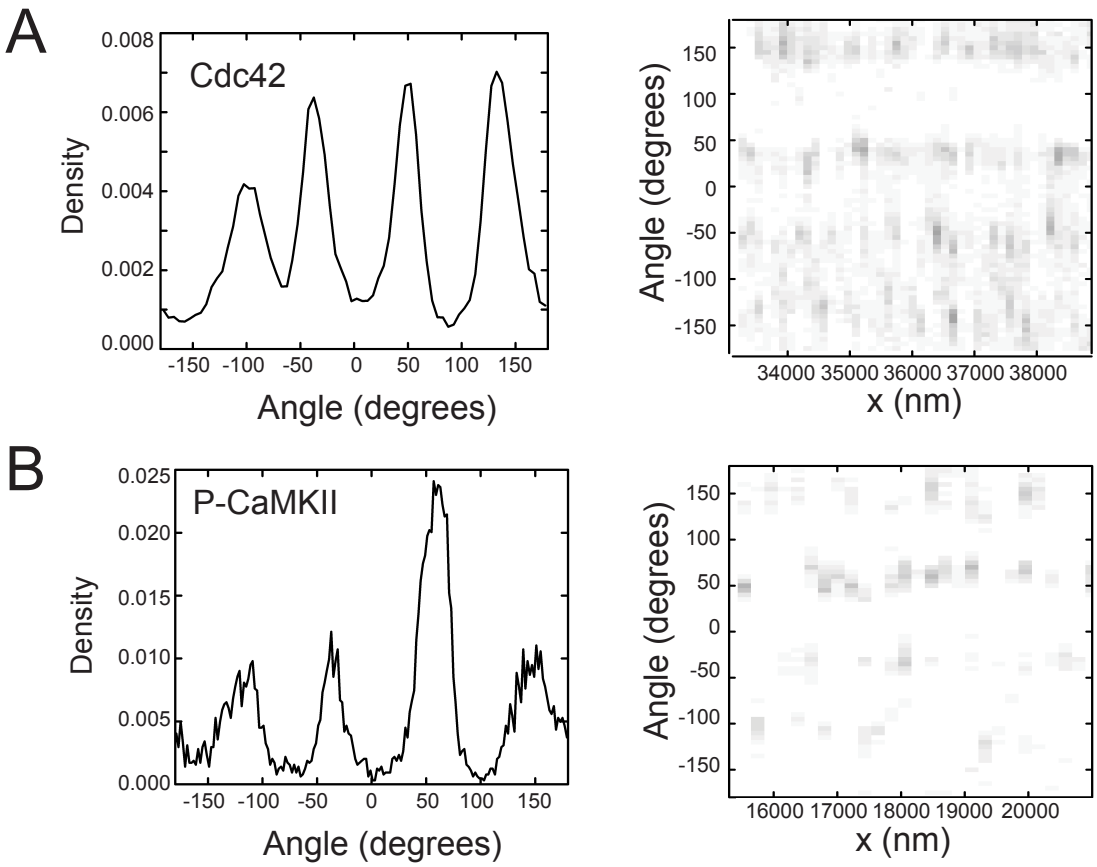

Figure 4.4: Cdc42 is localized in four longitudinal lines similar to P-CaMKII. (A) Angular distributions (right) and profiles (left) of the surface-localized Cdc42. (B) Angular distributions (right) and profiles (left) of the surface-localized P-CaMKII.

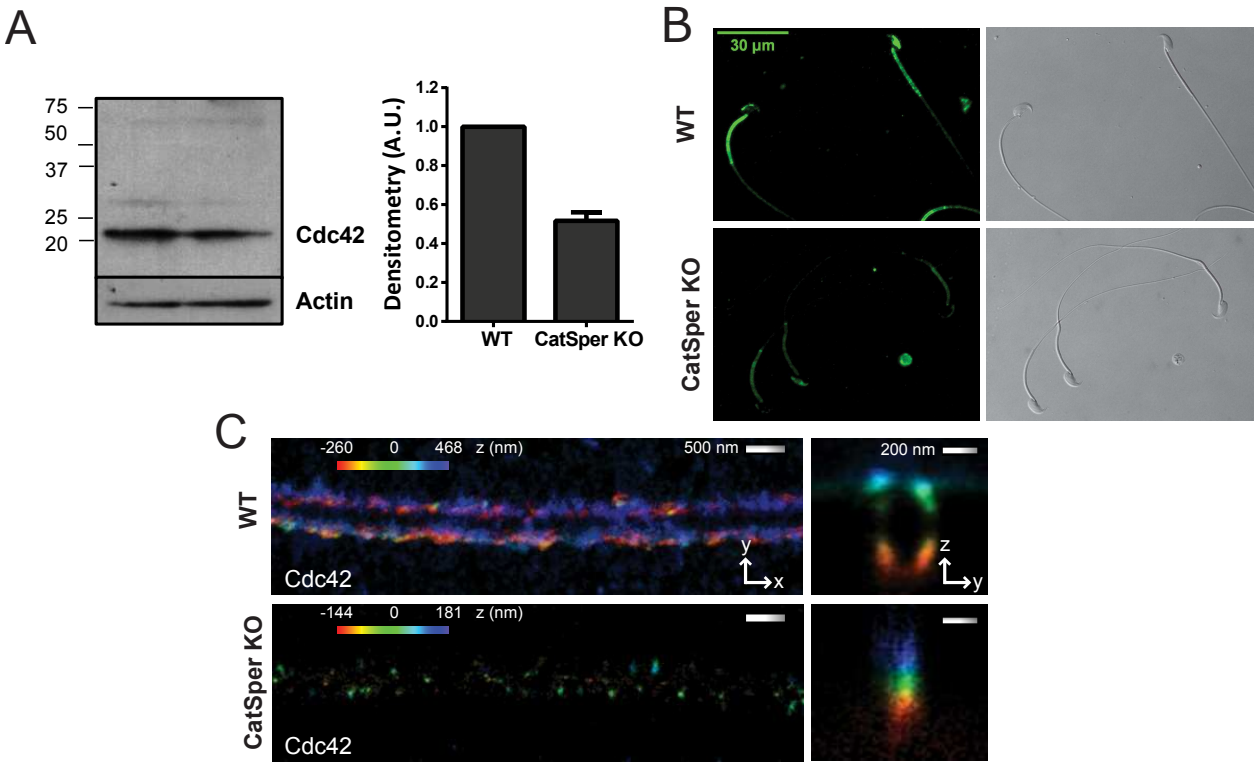

Figure 4.5: CatSper is essential for Cdc42 spatial organization and expression. (A) Proteins ($\sim 10 \times 10^6$sperm) were analyzed by 15% SDS-PAGE and immunoblotted using antibody against the small GTPase Cdc42. As a loading control, anti-Actin was used. Quantitative analysis were performed by measuring the optical density of all bands and relativized to Actin. Values represent the mean$\pm$SEM of 3 independent experiments, where normalization to the control condition (WT sperm) was used. Non-parametric Wilcoxon signed-rank test was performed (hypothetical value: 1; control condition). (B) Representative image of non-capacitated WT and CatSper KO sperm stained with anti-Cdc42 antibody and obtained by confocal microscopy. An Alexa Fluor 488-conjugated goat anti-mouse was used (green). The corresponding phase-contrast micrographs are shown. (C) Representative 3D STORM images showing the localization of Cdc42 in the principal piece of WT sperm at x-y projection (left, upper panel) and in y-z cross-section (right, upper panel); Representative 3D STORM images of CatSper KO principal piece Cdc42 (lower panel). Left, x-y projections. Right, y-z cross-sections (n=23 sperm from 3 different mice). The color in all x-y projections encodes the relative distance from the focal plane along the z axis. Negative controls were performed by incubating sperm with IgG.

studies revealed that Cdc42 was also present along the flagellum in the acrosome of CatSper KO (Fig. 4.5(B)) as in the WT sperm; although with lower fluorescence intensity, consistent with reduced protein expression (Fig. 4.5(A)). 3D STORM analyses in CatSper KO sperm were performed, but only poor quality reconstructions could be obtained due to the low number of localized fluorophores (2 ± 1 localizations/nm in CatSper KO vs. 10 ± 2 localizations/nm in WT sperm), in agreement with lower protein expression. In summary, 21 out of 23 sperm analyzed of CatSper KO sperm showed a clear Cdc42 delocalization from the quadrilateral structure in comparison with WT sperm (Fig. 4.5(C)).

4.3 Discussion

Recent studies in mouse have demonstrated that CatSper distributes longitudinally along four backbone lines, localized in the plasma membrane of the principal piece [62, 82]. Similarly, in humans, it has been reported that the newly described CatSper ξ subunit is also arranged in these segregated domains [82]. In addition to this unique structure, CatSper channels colocalize with Ca^{2+} signaling molecules such as P-CaMKII, Caveolin-1 and PP2B forming Ca^{2+} domains along the flagellum which orchestrate the timing and extent of complex phosphorylation cascades [62]. In the present work, by using super-resolution microscopy, the small GTPase Cdc42 was localized in the sperm flagellum forming four columns along the principal piece, which resembles the localization of CatSper. Considering this result, Cdc42 emerges as a new component of these highly organized Ca^{2+} domains.

CatSper scaffolds P-CaMKII, Caveolin-1 and PP2B in this defined quadrilateral structure, as sperm from CatSper1-null mice showed these proteins delocalized becoming uniformly distributed in the plasma membrane [62]. Similarly, most CatSper KO sperm displayed a disorganized Cdc42 distribution in the principal piece suggesting that this protein is associated with this signaling domain using mechanism that are similar to those used by P-CaMKII, Caveolin-1 and PP2B.

In somatic cells, Cdc42 is linked to actin cytoskeleton remodeling and exocytic processes [145, 146]. Previous reports described the involvement of Cdc42 in acrosomal exocytosis, by

its interaction with Caveolin-1. Both Caveolin-1 and Cdc42 were co-immunoprecipitated from guinea pig and mouse sperm [147]. The similar domain organization observed for both Cdc42 and Caveolin-1 may indicate possible functional interactions between these two proteins, although this needs to be further investigated.

In summary, our results suggest that Cdc42 is a key component of the highly organized signaling complex that controls $[Ca^{2+}]_i$ through CatSper channels triggering the development of hyperactivated motility. Considering that CatSper is sperm specific and has a fundamental role in hyperactivation, this channel has emerged as a potential therapeutic target in male infertility as well as in the development of contraceptive strategies. Understanding the modulation of CatSper activity and all the players involved is of great importance.

Chapter 5

Modeling of PKA-mediated sperm capacitation process

5.1 Introduction

[4] The mammalian spermatozoa, as highly polarized cells with the very unique morphology, are indispensable for new life development. They are transcriptionally silent, thus post-translational modification of proteins is the only mechanism available for signal transduction [148]. Following ejaculation, a series of major biochemical transformations, collectively termed capacitation process, are required for successful fertilization.

In the last few decades, tremendous efforts have been put into the study of sperm capacitation process. A fundamental capacitation signaling pathway derived from up-to-date experimental measurements has been proposed in the Fig. 5.1 [149]. At the molecular level, with the mutually complementary stimulation of HCO_3^{-1}, Ca^{2+} and plasma membrane cholesterol depletion factor like BSA (bovine serum albumin), SACY will be activated to raise the intracellular levels of cAMP, which rapidly activates PKA. Once activated, PKA phosphorylates various substrates to continue downstream reactions, which eventually lead to the protein tyrosine phosphorylation that is considered as the hallmark of the capacitation process [149].

Although various signal proteins have been identified in the capacitation process, the behavior of each individual molecule can not be predicted. The biological system like this falls exactly in the category of stochastic system. Molecules can be recognized as random variables and the very basic steps of every molecular reaction can be described in terms of its probability of occurrence. The modeling of the entire process becomes necessary for quantitative understanding as

[4]The work presented in this chapter has been performed in collaboration with Prof. Dario Krapf (Instituto de Biología Molecular y Celular de Rosario, Rosario, Argentina), Prof. Pablo Visconti (University of Massachusetts, Amherst), Prof. Mariano Buffone (Instituto de Biología y Medicina Experimental, Buenos Aires, Argentina), Andrew Fox, Zachary Fox, Prof. Brian Munsky (Colorado State University, Fort Collins).

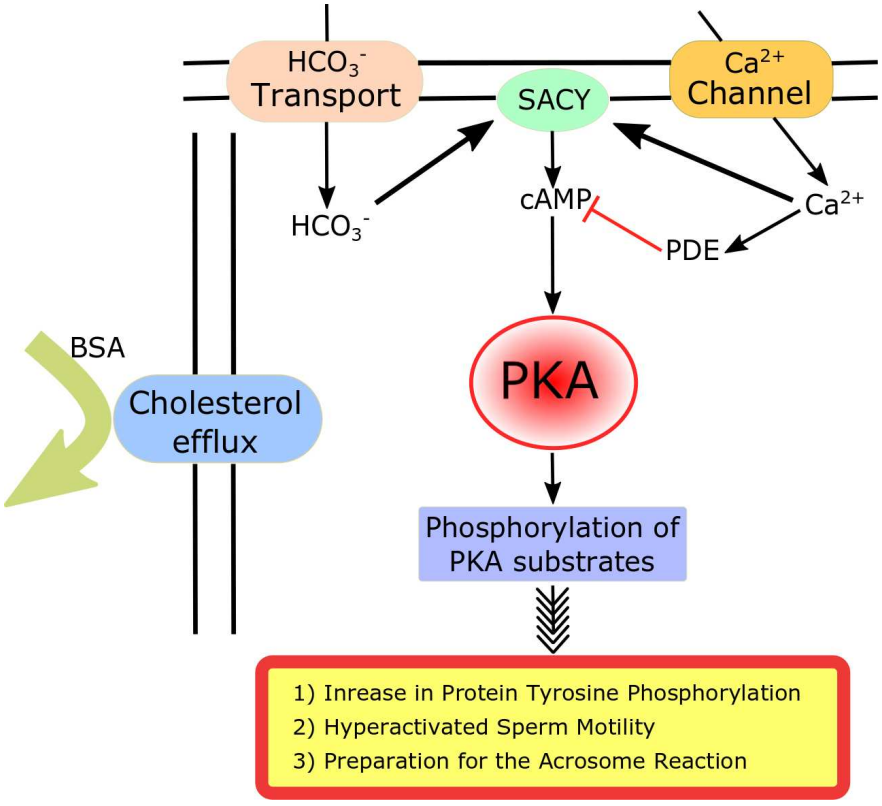

Figure 5.1: Schematic diagram of PKA-dependent sperm capacitation signaling pathway, adopted from [149].

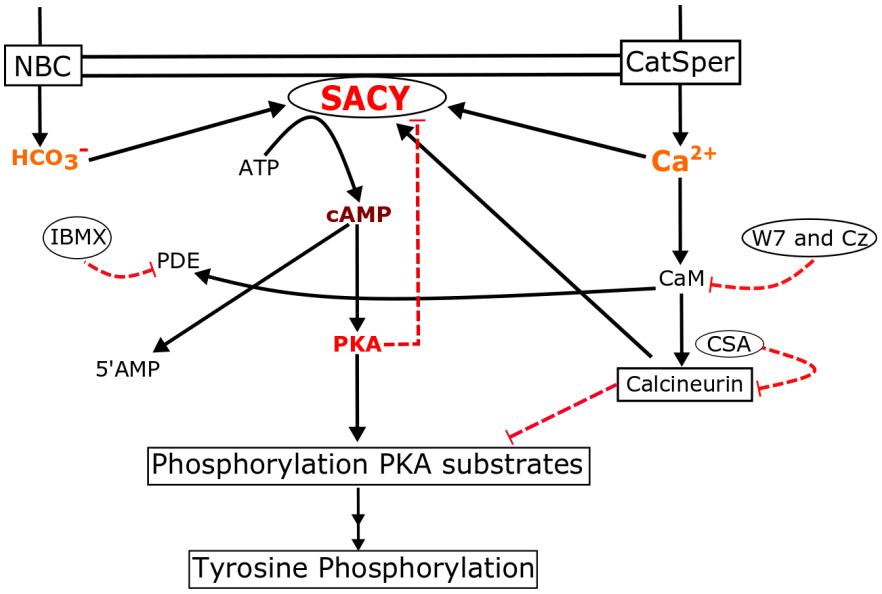

Figure 5.2: Proposed model for the crosstalk between Ca^{2+} and cAMP-dependent signaling pathway, adopted from [150]. Solid black lines: Stimulatory pathways; Red dash lines: Inhibitory pathways.

well as predicting the molecule states and concentration fluctuations since it's still missing in the field. With this being said, the goal of this project is to build a robust model for PKA-dependent capacitation signaling pathway.

5.2 Theoretical model

A simplified sketch representing the cascading events in sperm capacitation process can be illustrated in Fig. 5.2 [150]. Initially, HCO_3^- and Ca^{2+} stimulate the activation of SACY (also known as Adcyc10) to produce cAMP. cAMPs bind to PKA complex to activate catalytic subunits of PKA, which phosphorylates downstream substrates for further tyrosine phosphorylation. Meanwhile, inhibitory pathways work in concert with stimulatory pathways to coordinate the dynamics in the capacitation.

Recent discoveries revealed that Ca^{2+} exhibits a biphasic role in contributing the sperm capacitation, which means high level of tyrosine phosphorylation can be visualized at both high and extremely low concentration of Ca^{2+}, where EGTA is used as chelating agent in the second case to further reduce the concentration of Ca^{2+} in the media, as shown in Fig. 5.3 [150]. It is worth not-

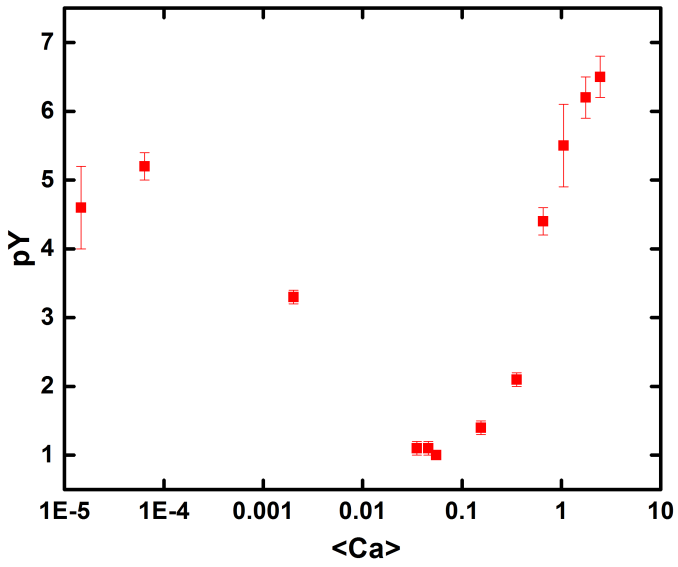

Figure 5.3: Biphasic dependence of tyrosine phosphorylation on Ca^{2+} [150]. Consolidated tyrosine phosphorylation measurements vs. Ca^{2+} titration with two different conditions: 1) Nominal Ca^{2+} with added EGTA as Ca^{2+} chelator but no added Ca^{2+} 2) Nominal Ca $^{2+}$ with added Ca^{2+} but no added EGTA.

ing that the activation of enzyme PDE (phosphodiesterase) and protein phosphatase calcineurin are mediated by the multifunctional intermediate calcium-binding messenger protein CaM (calmodulin). PDE degrades the cAMP, which later decreases the PKA phosphorylation as well as tyrosine phosphorylation. The same effect could be achieved by the inhibitory result of calcineurin. All of these cascaded reactions can be traced back to the central mediator Ca^{2+}, which indeed implies a negative feedback control leading to the increase in tyrosine phosphorylation, where calmodulin in involved. The consistent results are acquired when applying both calmodulin antagonists and inhibitors of calmodulin-dependent enzymes [150]. This biphasic feature of Ca^{2+} should be addressed when evaluating the validity of the model.

Based on the current comprehensive understanding of the sperm capacitation process, a quantitative model can be explicitly derived as pictured in Fig. 5.4. Overall, the reactions happen in three major steps.

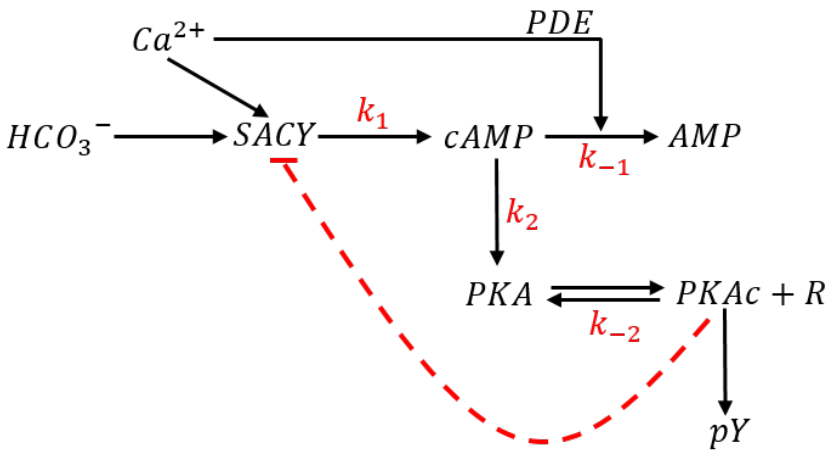

Figure 5.4: Proposed model of the regulated cAMP-dependent capacitation signaling network. SACY is activated via the combined effect Ca^{2+} and HCO_3^-, SACY catalyzes the synthesis of cAMP, in turn cAMP is degraded by PDE. cAMP binds to PKA holoenzyme to activate catalytic subunits. The activity of PKA also inhibits SACY.

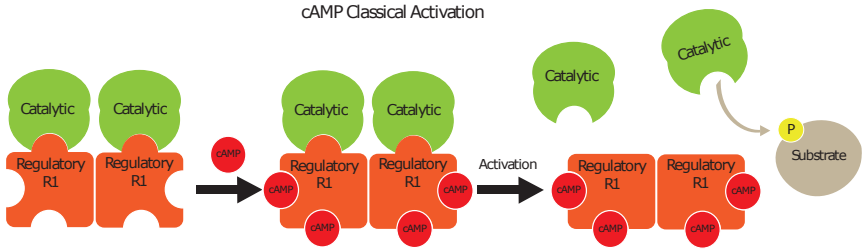

Figure 5.5: Traditional activation of PKA complex. The PKA holoenzyme consists of two regulatory and two catalytic subunits. When four cAMPs bind to the regulatory part, the catalytic subunits are released thus activated.

Step1: SACY catalyzes the conversion of ATP to cAMP with the co-stimulation of HCO_3^{-1} and Ca^{2+}.

$$\text{ATP + SACY} \xrightarrow{k_1} \text{cAMP + PPi + SACY;}$$

Step2: The degradation of cAMP through PDE.

$$\text{cAMP + PDE} \xrightarrow{k_{-1}} \text{AMP + PDE;}$$

Step3: PKA activation through the cAMP binding. Each PKA complex consists of two catalytic subunits PKAc and two regulatory subunits PKAr. Upon binding of four cAMPs, two free PKAc will be released from the PKA complex, while PKAr will remain bound on the complex as shown in Fig. 5.5 [151].

$$4\,\text{cAMP + PKA} \underset{k_{-2}}{\overset{k_2}{\rightleftharpoons}} 2\,\text{PKAc + PKAr.}$$

Let us define the total amount of PKAc as $2p_1$ and total amount of PKAr as p_2. The concentration relations can be written as in Eq. [5.1]:

$$2\,\text{PKA} + \text{PKAc} \equiv 2\,p_1 \quad ; \quad \text{PKA} + \text{PKAr} \equiv p_2. \tag{5.1}$$

where PKA represents the remained inactive PKA complex, PKAc is the free activated catalytic subunits of PKA, and PKAr is the corresponding regulatory subunits of PKA when PKAc is released. Consequently, PKA and PKAr can be expressed with p_1, p_2, and PKAc:

$$\text{PKA} = \text{p}_1 - 0.5\,\text{PKAc} \quad ; \quad \text{PKAr} = \text{p}_2 - \text{p}_1 + 0.5\,\text{PKAc}. \tag{5.2}$$

Collectively, we can formulate the process into two ODE in regard to HCO_3^{-1}, Ca^{2+}, cAMP and PKAc:

$$\frac{d[cAMP]}{dt} = \left(\frac{k_1 m_3}{m_3 + [PKAc]}\right)\left(\frac{[HCO_3^{-1}](1 + c[Ca^{2+}])}{m_1 + [HCO_3^{-1}](1 + c[Ca^{2+}])}\right) - \frac{k_{-1}[Ca^{2+}][cAMP]}{k_c + [Ca^{2+}]} \tag{5.3}$$

$$\frac{d[PKAc]}{dt} = \frac{2k_2[cAMP]^4(p_1 - 0.5[PKAc])}{m_2 + [cAMP]^4(p_1 - 0.5[PKAc]} - 0.5k_{-2}[PKAc]^2(p_2 - p_1 + 0.5[PKAc]) \quad (5.4)$$

which comprises our model, where **[ ]** means the concentration of the molecule and 11 coefficients need to be solved as listed in Table 5.1.

Table 5.1: Summary of the parameter variables

	Parameter	**Unit****	**Physical Meaning**
1	k_1	$mM \cdot min^{-1}$	cAMP synthetic rate by active SACY
2	m_3	au^*	noncompetitive inhibition dissociation constant of SACY by PKAc
3	c	mM^{-1}	Ca^{2+}dependent SACY activity enhancement constant
4	m_1	mM	Michaelis constant of SACY activation by HCO_3^-
5	k_{-1}	min^{-1}	cAMP degradation rate by Ca^{2+}dependent PDE
6	k_c	mM	PDE saturation term for excess Ca^{2+}
7	k_2	$au \cdot min^{-1}$	Association rate of cAMP into PKA and activation of PKA
8	p_1	au	Total amount of PKAc (Catalytic subunits)
9	m_2	$au \cdot mM^4$	Michaelis constant for activation of PKA
10	k_{-2}	$au^{-2} \cdot min^{-1}$	Association rate of PKAc back into PKA complex
11	p_2	au	Total amount of PKAr (Regulatory subunits)

* ***au*** *is the arbitrary unit used in normalized tyrosine phosphorylation pY measurement.*
** *Units are derived according to known measurements and dimensional analysis*

5.3 Parameters improvement

5.3.1 Experimental data

The model validation starts with the titration data, that is the steady state measurements, which are extracted from the publication and shown in Table 5.2 to solve for the parameters presented above [150].

As said before, the dimensional analysis has been applied to ensure the consistence of the units among different parameters and inputs. The data in columns “cAMP" and “cAMP sem" of Table 5.2 needs to be converted into concentration measurements. Laboratory mice commonly used are

Table 5.2: Experimental measurements of pY and cAMP vs. Ca^{2+} titration ([HCO_3^-] = 15 mM) [150]

Ca (mM)	EGTA (mM)	Ca mean (mM)	pY (au)	pY sem (au)	cAMP (fmole/1M sperm)	cAMP sem (fmole/1M sperm)
0.03	0	0.085	-	-	-	-
0.1	0	0.155	1.4	0.1	-	-
0.3	0	0.355	2.1	0.1	43	10
0.6	0	0.655	4.4	0.2	100	7
1	0	1.055	5.5	0.6	110	6
1.7	0	1.755	6.2	0.3	430	60
2.4	0	2.455	6.5	0.3	550	5
0	0.01	0.0457	1.1	0.1	-	-
0	0.3	0.03506	1.1	0.1	-	-
0	0.1	$2.01\cdot 10^{-3}$	3.3	0.1	-	-
0	0.3	$6.42\cdot 10^{-5}$	5.2	0.2	-	-
0	1	$1.47\cdot 10^{-5}$	4.6	0.6	90	3

of the species *Mus musculus* (House mouse), from which, we were able to approximate a single sperm flagellum volume as $4\cdot 10^{-14}L$ [152]. According to Eq. [5.4], PKAc values can be derived at the steady state but not pY, while only experimental pY measurements are given. Here we actually have made an estimation for PKAc that the concentration ratio between PKAc and pY is set to be 1:1. Table 5.3 shows modified titration data input and Table 5.4 shows all the inputs and their concentration ranges.

5.3.2 Fitting with pY only

The first trial of model fitting was initiated with only PKAc $vs.$ Ca^{2+} data for less heavy computation and distinct observation of Ca^{2+} biphasic behavior. Considering the number of random variables, the literature search for prior knowledge of certain parameters has been conducted for dimensionality reduction. The first lead was hidden in the Fig. 5.6, which presents the SACY activity assessed at the indicated concentration of free Ca^{2+} *in vitro*. The SACY activity was measured through the changing rate of its downstream product cAMP when increasing the ATP substrate concentration. Essentially, each single plot means a SACY reaction rate versus the substrate content, representing *Michaelis-Menton* equation. We were able to extract the kinetic information from Fig.

Table 5.3: Experimental measurements of pY and cAMP vs. Ca^{2+} titration after unit adjustment ($[HCO_3^-]$ = 15 mM)

Ca (mM)	EGTA (mM)	Ca mean (mM)	pY (au)	pY sem (au)	cAMP (mM)	cAMP sem (mM)
0.03	0	0.085	-	-	-	-
0.1	0	0.155	1.4	0.1	-	-
0.3	0	0.355	2.1	0.1	0.0011	$2.5{\cdot}10^{-4}$
0.6	0	0.655	4.4	0.2	0.0025	$1.75{\cdot}10^{-4}$
1	0	1.055	5.5	0.6	0.0028	$1.5{\cdot}10^{-4}$
1.7	0	1.755	6.2	0.3	0.0108	0.0015
2.4	0	2.455	6.5	0.3	0.0137	$1.25{\cdot}10^{-4}$
0	0.01	0.0457	1.1	0.1	-	-
0	0.3	0.03506	1.1	0.1	-	-
0	0.1	$2.01{\cdot}\ 10^{-3}$	3.3	0.1	-	-
0	0.3	$6.42{\cdot}\ 10^{-5}$	5.2	0.2	-	-
0	1	$1.47{\cdot}\ 10^{-5}$	4.6	0.6	0.0023	$7.5{\cdot}10^{-5}$

Table 5.4: Experimental measurements input range

Input	Input range	Unit
cAMP	0.0011 — 0.0137	mM
Ca^{2+}	$1.47 \cdot 10^{-5}$ — 2.455	mM
PKAc*	1.1 — 6.5	au

* *Assume [pY]:[PKAc]=1:1*

5.6 to estimate the reasonable initial guesses for parameters involved in the SACY activity [153].

$$v = \frac{k_1[HCO_3^{-1}](1 + c[Ca^{2+}])}{m_1 + [HCO_3^{-1}](1 + c[Ca^{2+}])} \tag{5.5}$$

According to these measurements, we can re-plot the SACY reaction rate as the increasing concentation of Ca^{2+} for different ATP concentrations. Recall from Eq. [5.3], the LHS (left hand side) of the equation is indeed the reaction rate and the RHS (right hand side) contains the dependence on the Ca^{2+} concentration. A simplified function can be defined as shown in Eq. [5.5] to fit into the experimental measurements provided in Fig. 5.6, where $[HCO_3^-]$=25 mM, for order of magnitude estimation of parameter k_1, c and m_1 as shown in Fig. 5.7.

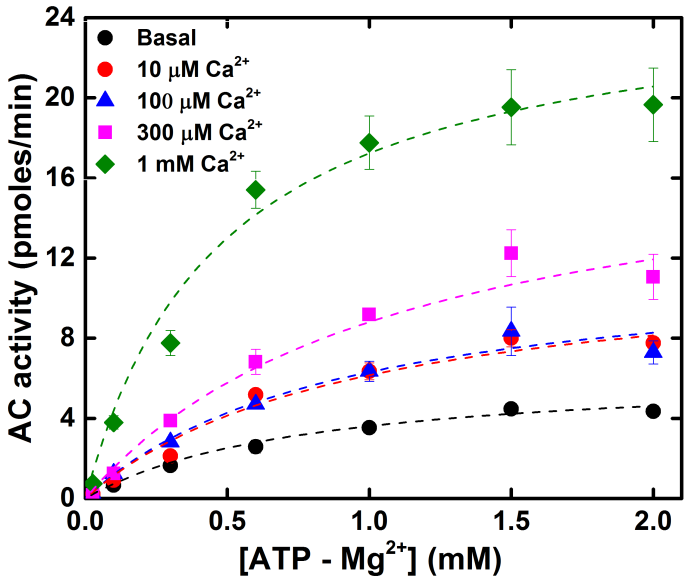

Figure 5.6: Kinetic properties of Ca^{2+}-activated SACY. The SACY activity was measured in the presence of 10 mM $MgCl_2$, 200 μM EGTA, 25 mM HCO_3^{-1} and increasing concentrations of free Ca^{2+} as a function of substrate ATP-Mg^{2+} [153].

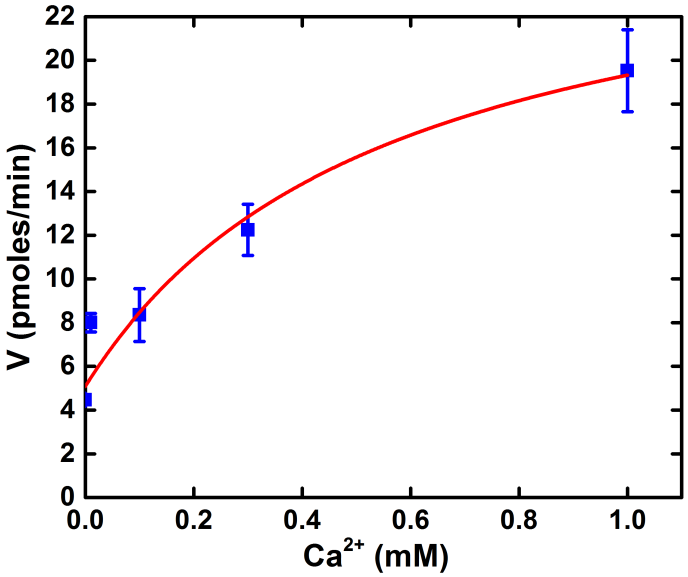

Figure 5.7: An example plot of sAC activity vs. Ca^{2+} at ATP = 1.5 mM. Blue squares are the individual data from Fig. 5.6 and red curve is the fitting of Eq. [5.5].

The values of parameters k_1, c and m_1 found through fitting in Fig. 5.7, where $k_1 = 27.3$, $c = 9.6$ and $m_1 = 109$, are used as initial guesses, while others are assigned values 0.5 for solving models and optimization, during which *MATLAB ODE Solvers* and *fminsearch* algorithm are applied. After a few cycles of iterations, the parameters will reach convergence. Afterwards, if the parameters set is not ideal, the *simulated annealing* algorithm would be integrated into the parameter searching process, in which, the random number of parameters N (N $\in [2, 8]$) will be modified to have up to two orders of magnitude change, for better chance in reaching the global optima rather than trapped in the local optima [154].

5.3.3 Fitting with both pY and cAMP

After getting a decent fitting to the model with pY only data, cAMP $vs.$ Ca^{2+} titration data has also been added into the model fitting process for higher accuracy. However, some cAMP measurements are missing for certain Ca^{2+} titration as seen in Table.5.2. In order to have consistent number of measurements in terms of both pY and cAMP, cubic spline interpolation method has been employed on top of the known measurements of cAMP to fill the blanks. The interpolation results can be visualized in Fig. 5.8 and they are assigned with mean standard errors based on maximum and minimum standard errors of the rest of measurements.

5.4 Results

5.4.1 Fitting with pY only

The best parameter set A derived by fitting only PKAc dataset to the model is shown in Table 5.5. Fig. 5.9(A) shows a good agreement between model prediction and experimental results regarding the pY measurement with Ca^{2+} titration. On the other hand, the cAMP prediction is off by two orders of magnitude in comparison to the experimental results as in Fig. 5.9(B), which also points out the significance of adding the cAMP data into the model for more accurate fitting purpose.

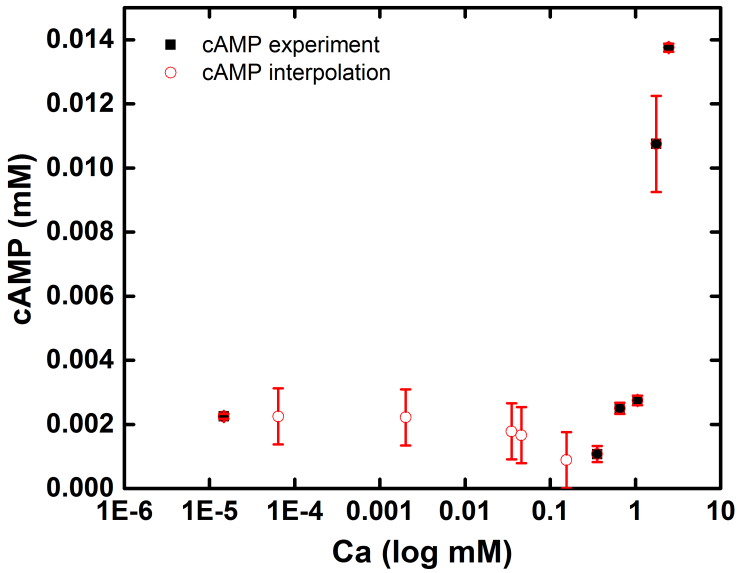

Figure 5.8: Spline interpolation of cAMP measurements. Interpolated cAMP values with standard error (red) registered with known experimental measurements (black) in semi-log plot.

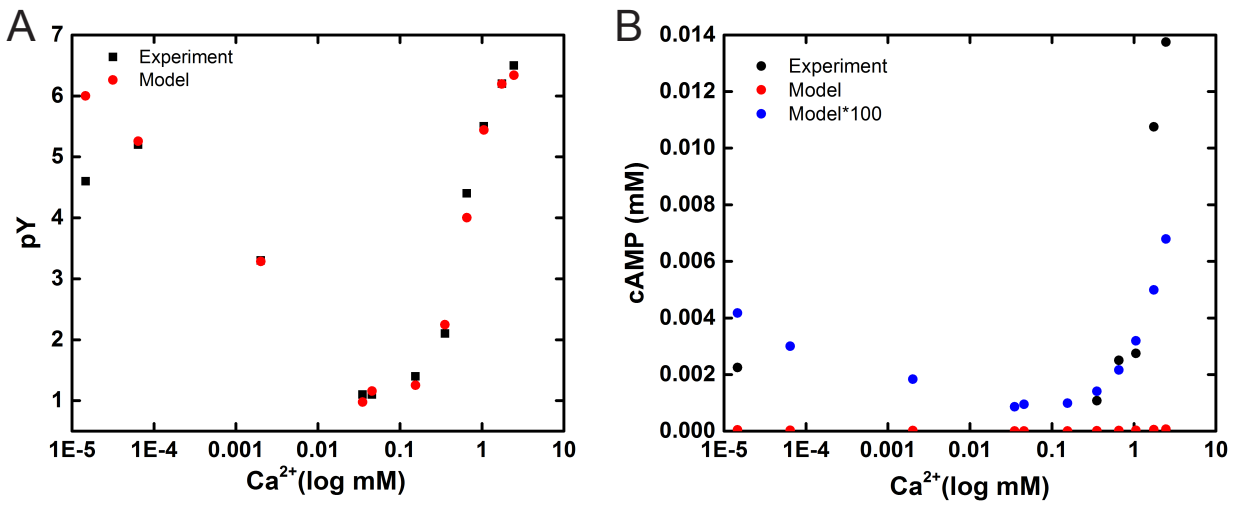

Figure 5.9: Model prediction and experimental measurements with pY group A. (A) pY vs. Ca^{2+} (red: model prediction, black: experimental results); (B) cAMP vs. Ca^{2+} (red: model prediction, black: experimental results, blue: model prediction $\times$ 100).

Table 5.5: Summary of parameter set A derived from the model by only fitting with pY

Parameter	Value	Unit	Physical Meaning
k_1	0.0286	$mM \cdot min^{-1}$	cAMP synthetic rate by active SACY
m_3	6.45 $\cdot 10^{19}$	au^*	noncompetitive inhibition dissociation constant of SACY by PKAc
c	35.622	mM^{-1}	Ca^{2+}dependent SACY activity enhancement constant
m_1	3.635 $\cdot 10^{7}$	mM	Michaelis constant of sAC activation by HCO_3^-
k_{-1}	0.0163	min^{-1}	cAMP degradation rate by Ca^{2+}dependent PDE
k_c	0.15	mM	PDE saturation term for excess Ca^{2+}
k_2	71325.526	$au \cdot min^{-1}$	Association rate of cAMP into PKA and activation of PKA
p_1	3.202	au	Total amount of PKAc (Catalytic subunits)
m_2	1.87 $\cdot 10^{-16}$	$au \cdot mM^4$	Michaelis constant for activation of PKA
k_{-2}	0.761	$au^{-2} \cdot min^{-1}$	Association rate of PKAc back into PKA complex
p_2	34.324	au	Total amount of PKAr (Regulatory subunits)

* ***au*** *is the arbitrary unit used in normalized tyrosine phosphorylation pY measurement.*

5.4.2 Fitting with both pY and cAMP

As for the case where both PKAc and cAMP measurements with Ca^{2+} titrations are introduced into the model fitting process, two parameter sets B1 and B2 have been found. Overall, the steady state concentrations predicted by both parameter sets resemble each other as well as the experimental measurements, as shown in Fig. 5.10 and Fig. 5.11. Meanwhile, despite some dramatic differences exhibited within a few parameters, a certain level of similarity among majority of parameters can be observed from Table 5.6 and Table 5.7.

5.4.3 Model order reduction

Let us re-observe our model, starting with Eq. 5.3:

$$\frac{d[cAMP]}{dt} = (\frac{k_1 m_3}{m_3 + [PKAc]})(\frac{[HCO_3^{-1}](1 + c[Ca^{2+}])}{m_1 + [HCO_3^{-1}](1 + c[Ca^{2+}])}) - \frac{k_{-1}[Ca^{2+}][cAMP]}{k_c + [Ca^{2+}]}$$

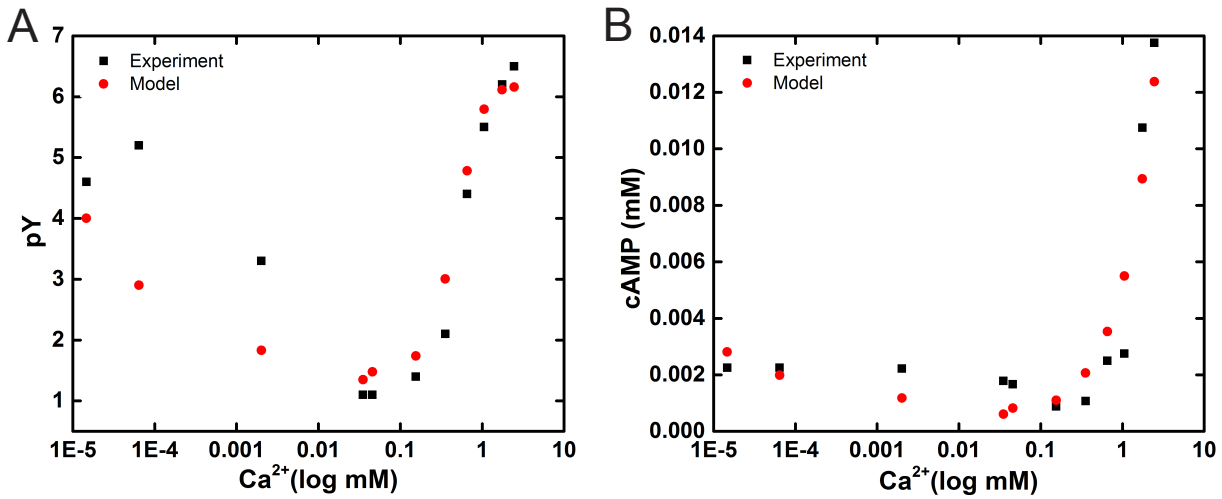

Figure 5.10: Model prediction and experimental measurements with pY and cAMP group B1, corresponding to parameters in Table 5.6. (A) pY vs. Ca^{2+} (red: model prediction, black: experimental results); (B) cAMP vs. Ca^{2+} (red: model prediction, black: experimental results).

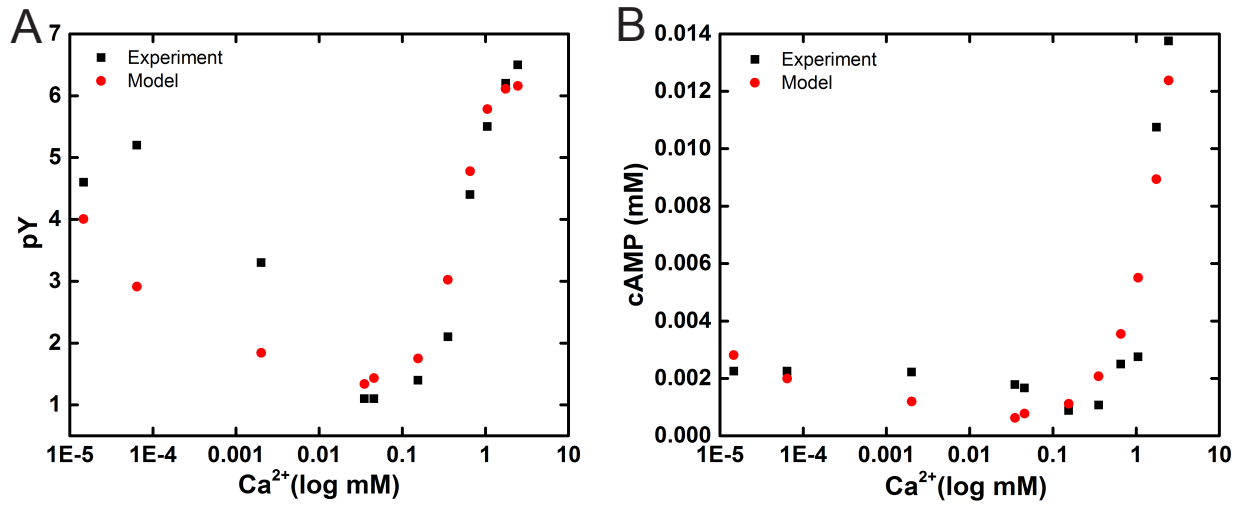

Figure 5.11: Model prediction and experimental measurements with pY and cAMP group B2, corresponding to parameters in Table 5.7. (A) pY vs. Ca^{2+} (red: model prediction, black: experimental results); (B) cAMP vs. Ca^{2+} (red: model prediction, black: experimental results).

Table 5.6: Summary of parameter set B1 derived from the model by fitting with both pY and cAMP

Parameter	Value	Unit	Physical Meaning
k_1	0.899	$mM \cdot min^{-1}$	cAMP synthetic rate by active sAC
m_3	7.864 $\cdot 10^8$	au^*	noncompetitive inhibition dissociation constant of sAC by PKAc
c	46.501	mM^{-1}	Ca^{2+}dependent sAC activity enhancement constant
m_1	1.635 $\cdot 10^7$	mM	Michaelis constant of sAC activation by HCO_3^-
k_{-1}	0.0078	min^{-1}	cAMP degradation rate by Ca^{2+}dependent PDE
k_c	0.0414	mM	PDE saturation term for excess Ca^{2+}
k_2	185.59	$au \cdot min^{-1}$	Association rate of cAMP into PKA and activation of PKA
p_1	23.899	au	Total amount of PKAc (Catalytic subunits)
m_2	4.464 $\cdot 10^{-9}$	$au \cdot mM^4$	Michaelis constant for activation of PKA
k_{-2}	7.945	$au^{-2} \cdot min^{-1}$	Association rate of PKAc back into PKA complex
p_2	23.261	au	Total amount of PKAr (Regulatory subunits)

* ***au*** *is the arbitrary unit used in normalized tyrosine phosphorylation pY measurement.*

Our parameter-searching algorithm sets the LHS $\frac{d[cAMP]}{dt} = 0$ in order to find the steady-state solutions. Mathematically, this equation can be generalized in the form:

$$0 = k_1 f - k_{-1} g; \tag{5.6}$$

where f and g are remainder functions. Then,

$$0 = k_1 (f - \frac{k_{-1}}{k_1} g). \tag{5.7}$$

Furthermore, k_1 being a positive value due to the nature of chemical reaction rate makes it only possible to acquire the steady-state solution of the ratio $\frac{k_{-1}}{k_1}$, which can be defined as K_1, the reciprocal of equilibrium constant [155].

According to Table. 5.6 and Table. 5.7, the magnitude of m_1 has order of 10^7. In Eq. 5.3, the term $[HCO_3^{-1}(1 + c[Ca^{2+}])]$ next to m_1 is comparably small and thus can be neglected, which

Table 5.7: Summary of parameter set B2 derived from the model by fitting with both pY and cAMP

Parameter	Value	Unit	Physical Meaning
k_1	0.975	$mM \cdot min^{-1}$	cAMP synthetic rate by active sAC
m_3	244539.236	au^*	noncompetitive inhibition dissociation constant of sAC by PKAc
c	54.085	mM^{-1}	Ca^{2+}dependent sAC activity enhancement constant
m_1	1.778 $\cdot 10^7$	mM	Michaelis constant of sAC activation by HCO_3^-
k_{-1}	0.00906	min^{-1}	cAMP degradation rate by Ca^{2+}dependent PDE
k_c	0.0474	mM	PDE saturation term for excess Ca^{2+}
k_2	4906.394	$au \cdot min^{-1}$	Association rate of cAMP into PKA and activation of PKA
p_1	15.479	au	Total amount of PKAc (Catalytic subunits)
m_2	2.755 $\cdot 10^{-9}$	$au \cdot mM^4$	Michaelis constant for activation of PKA
k_{-2}	209.263	$au^{-2} \cdot min^{-1}$	Association rate of PKAc back into PKA complex
p_2	14.851	au	Total amount of PKAr (Regulatory subunits)

* ***au*** *is the arbitrary unit used in normalized tyrosine phosphorylation pY measurement.*

implies that there is no Ca^{2+} saturation. Similarly, the value m_3 is much larger than its neighboring term $[PKAc]$. The neglecting of $[PKAc]$ shows no existence of PKAc inhibition to SACY activity and results in the approximation of entire term $\frac{m_3}{m_3+[PKAc]}$ to be 1. Consequently, Eq. 5.3 can be simplified as:

$$\frac{d[cAMP]}{dt} = \frac{[HCO_3^{-1}](1 + c[Ca^{2+}])}{m_1} - \frac{K_1[Ca^{2+}][cAMP]}{k_c + [Ca^{2+}]} \tag{5.8}$$

The next step is to move on to the Eq. 5.4:

$$\frac{d[PKAc]}{dt} = \frac{2k_2[cAMP]^4(p_1 - 0.5[PKAc])}{m_2 + [cAMP]^4(p_1 - 0.5[PKAc])} - 0.5k_{-2}[PKAc]^2(p_2 - p_1 + 0.5[PKAc])$$

The whole term $(p_2 - p_1 + 0.5[PKAc])$, representing the amount of free PKAr, should be non-negative. This exerts a lower bound on the value of $p_2 - p_1$. With our assumption regarding the concentration relation between PKAc and pY is 1:1, the minimal value of $[PKAc]$ is 1 and that limits $p_2 - p_1$ to be at least -0.5. We've decided to use this lower bound value -0.5 to replace $p_2 - p_1$

in the equation. In addition, we use the idea shown in Eq. [5.6-5.7] to define another equilibrium constant $K_2 = \frac{k_2}{k_{-2}}$ to further eliminate one more parameter. With that being said, the second model equation can be rewritten as:

$$\frac{d[PKAc]}{dt} = \frac{2K_2[cAMP]^4(p_1 - 0.5[PKAc])}{m_2 + [cAMP]^4(p_1 - 0.5[PKAc])} - 0.5[PKAc]^2(0.5[PKAc] - 0.5) \tag{5.9}$$

After the dimensionality reduction, the corresponding variable-reduced parameter sets can be found in Table 5.8(A) and Table 5.8(B). Surprisingly, the discrepancy exhibited in some parameters in Table 5.6 and Table 5.7 has disappeared. Two parameter sets show a good agreement between each other.

Table 5.8: Summary of re-organized parameter sets after model order reduction

(A)

Parameter	**Value**	**Unit**
K_1	8.676 $\cdot 10^{-3}$	mM^{-1}
c	46.501	mM^{-1}
k_c	0.0414	mM
K_2	23.359	au^3
p_1	23.899	au
m_2	4.464 $\cdot 10^{-9}$	$au \cdot mM^4$
m_1	1.635 $\cdot 10^{7}$	mM

(B)

Parameter	**Value**	**Unit**
K_1	9.292 $\cdot 10^{-3}$	mM^{-1}
c	54.085	mM^{-1}
k_c	0.0474	mM
K_2	23.446	au^3
p_1	15.479	au
m_2	2.755 $\cdot 10^{-9}$	$au \cdot mM^4$
m_1	1.778 $\cdot 10^{7}$	mM

Importing these two parameter sets into our model fitting algorithm gives rise to one converged parameter set, as seen in Table.5.9.

Table 5.9: The most updated parameter set C derived from the simplified model

Parameter	**Value**	**Unit**
K_1	8.21 $\cdot 10^{-3}$	mM^{-1}
c	48.729	mM^{-1}
k_c	0.0424	mM
K_2	28.339	au^3
p_1	3.159	au
m_2	2.824$\cdot 10^{-10}$	$au \cdot mM^4$
m_1	1.811 $\cdot 10^{7}$	mM

5.5 Discussion

The field of sperm capacitation study has greatly progressed in terms of the characterization of molecules involved in capacitation signaling pathways since a couple decades ago [1, 2, 122]. However, the community is still facing challenges that are difficult to tackle with the present approaches: sperm populations are heterogeneous, whereas the evaluation of the average cellular parameters does not necessarily represent the physiological state of a given cell; and individual cell studies are extremely laborious, jeopardizing the collection of statistically significant results. Thus, we seek the solution from another perspective to break these limitations by introducing the significance of quantitative modeling development that can predict cell fate and aids in the understanding of cell variability, eventually for achieving the fertilizing capacity acquisition.

Given the ODE model derived on the foundation of comprehensive understanding of current sperm capacitation studies, we were able to acquire a set of parameters to correctly reflect the behaviors of tyrosine phosphorylation and cAMP with the discrete Ca^{2+} titrations. The model should also be run on the continuous inputs so that the accurate prediction can be made with fully-validated model for any given titrations. In the current setting, we have made an assumption for PKAc concentrations that are arised from pY measurements with 1:1 ratio. To describe the model more precisely, it is better to either integrate the relation between PKAc and pY into the model or gather direct PKAc experimental measurements.

It is known that the phosphorylated PKA substrates lead to the tyrosine phosphorylation, which absolutely requires the stimulation of Ca^{2+}. On the other hand, Ca^{2+} also regulates the activation of CaM, which is responsible for activating PDE and calcineurin. Calcineurin has been shown to be involved in de-phosphorylation of Ser/Thr residues present in PKA substrates, which in turn affect the tyrosine phosphorylation [150]. It is suggested that Ca^{2+} could play a role in inhibiting the tyrosine phosphorylation production. Another possible model can be proposed on that premise as shown in Fig. 5.12. This newly added pathways can be formulated as in Eq. 5.10, which can be added as the third ODE to the model.

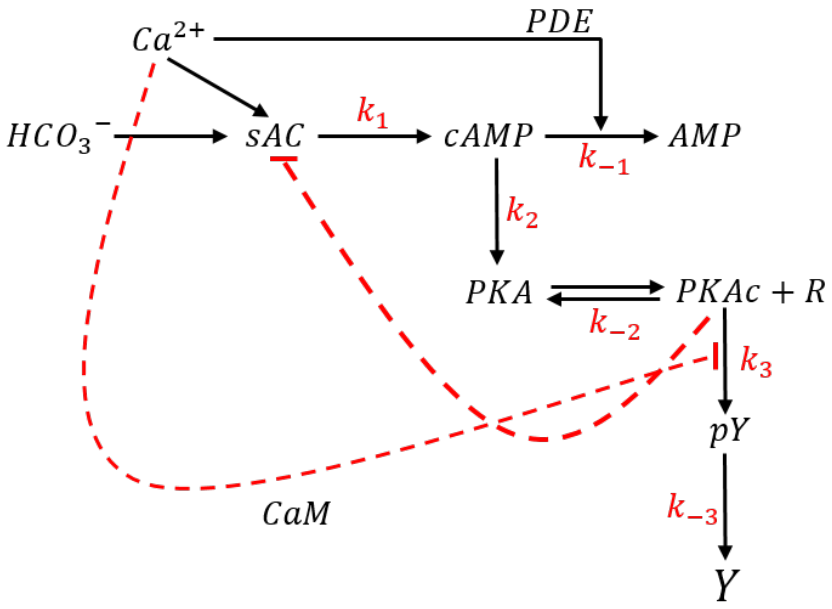

Figure 5.12: Another proposed model connecting PKAc and pY. pY production from PKAc with Ca^{2+} inhibition and pY dephosphorylation have been added, compared to the model in Fig. 5.4. k_3 is the pY production rate that's affected by [Ca^{2+}], k_{-3} is the dephosphorylation rate of pY.

$$\frac{d[pY]}{dt} = \frac{k_3}{1 + c_1[Ca^{2+}]}[PKAc] - k_{-3}[pY] \tag{5.10}$$

Once the model is solved, the validation process should be initiated with experiments in which sperm cells are incubated in a given Ca^{2+} concentrations, then average cAMP concentration and PKA activity can be measured at different incubation times. The results will be used to fit rate constants within the model. The results from steady-state measurements will be validated and if discrepancies are found, the values and model will be re-evaluated. Bootstrapping will be employed to estimate the performance of the model [156]. Namely, the robustness tested comparing model predictions to a random 30% fraction of the cells while the fitting is performed on the other 70%. Then cross-validate the model ability to make quantitative predictions by altering the temporal inputs. The model should also be tested against inhibition of specific pathways. The inhibitors IBMX, cyclosporine A and the soluble form of the protein kinase inhibitor sPKI can be employed to target PDE, calcineurin and PKA respectively [157, 158].

Chapter 6

Conclusion and future directions

In this dissertation, the super-resolution imaging and analysis of both structural and signaling proteins that are involved in the sperm capacitation process have been elaborated to further understand the underlying mechanism from the localization perspective. What's more, we took a different approach - stochatic modeling, rather than cell by cell experiments, to quantify the capacitation process in an ensemble way.

In the chapter two, the actin cytoskeleton structure consists of actin and two actin-binding protiens spectrin and adducin has been investigated in both sperm midpiece and principal piece. With the help of super-resolution imaging, the subcellular structure between compartments can be differentiated. In the midpiece, the actin forms a double helix structure with 87 gyres of helices localized in the thin region between the mitochondria. The adducin localizes very closely to the actin with a sparsely dotted ring structure, while the spectrin localizes closely to the plasma membrane with a uniformly distributed ring structure. When it comes to the principal piece, the helical-like structure of actin has disappeared. Instead, it forms a dense bundle, displaying the maxium density nearby the axoneme. Adducin and spectrin are both showing the uniformly distributed ring structures through the principal piece. A very clear difference between spectrin and the other two proteins is that spectrin radius is dependent on the location where the measurements are taken. When the spectrin is getting away from the annulus, the boundary between midpiece and principal piece, the radius is getting smaller and smaller. It's a very intuitive result considering that spectrin localizes closely to the membrane and the sperm tail tapers towards the end. From the localization wise, the actin localizes at the inner center of the sperm, spectrin is at the proximity of the plasma membrane and the adducin is in between these two proteins. We have also confirmed the six novel localization of filamentous actin in the sperm head with STORM, that are discovered by using the combination of SiR-actin and confocal micoscopy on the live sperm for the first time in Dr. Buffone's group.

We have explored the spatial dynamics of PKA and tyrosine kinase identity that's responsible for the tyrosine phosphorylation towards the end of capaciation process in the chapter three. it has been discovered that the localization of PKA has been shifted to a broader range after capacitation. After introducing the inhibitory drug sHT31 that impairs the binding between the PKA and AKAPs, this change of localization has been abrogated, indicating the importance of tight spatial regulation as well as the role of AKAPs in partially conveying the regulation of PKA activity. Based on the work done by Dr. Visconti's lab, we looked into the localization of both proposed tyrosine kinase candidate FER and phosphorylated tyrosine residues pY. It turns out that both proteins have very similar localization and FER colocalize with pY in both midpiece and principal piece.Thereby, from the spatial localization point of view, we further corroborate that FER is the PKA downstream substrate for phosphorylating the tyrosine residues.

In the chapter four, we have solved the question regarding the relation between small GTPase cdc42 and sperm specific calcium channel CatSper. Like the other Ca^{2+} signaling proteins in the sperm principal piece, cdc42 also exhibits a four-line localization, resembling the localization of CatSper. In the CatSper KO sperm, this very specialized quadrilateral structure of cdc42 gets disrupted, indicating that along with other Ca^{2+} signaling proteins, cdc42 is also a component that's part of these CatSper-dependent highly organized Ca^{2+} domain.

Finally, the last chapter explained how we use the ODEs to describe the capacitation process. We were able to construct three intertwined ODEs representing the reaction rates of cAMP, PKA and pY with the dependence on HCO_3^- and Ca^{2+} by interpreting the capacitation signaling pathway through the chemical master equation. A set of parameters were successfully obtained after iterations of fitting with optimization methods, showing the similar behavior of steady state concentrations to the corresponding discrete Ca^{2+} titration as the experimental measurements.

Through the work presented here, we have demonstrated the high resolving power of super-resolution imaging technique to unravel the subcellular localization and structure of multiple proteins highly involoved in the sperm functionailty, which help us understand more about the regulating connections among those proteins from the structual point of view. Additionally, the stochastic

modeling opens another gate to characterize the imperative capacition process of sperm and predict the cell fate as well as concentration fluctuations. However, what we have done is just a tip of the iceberg. As Albert Einstein said, "The more I learn, the more I realize how much I don't know". More questions have emerged to be investigated and answered.

We have found the tight relation between mitochondria and filamentous actin in the midpiece, implying that the mitochondria serve as the structure support for actin binding. The consistency of the number of gyres in the actin double helix structure with extremely low standard errors and the number of windings in mitochondria arrangment makes us wonder to what extent this relation is conserved among other species. For example, in the human sperm, does this relation still exist? It's known that the human sperm have much higher degree of heterogeneity compared to the mouse sperm [159]. If actin localization still follows the arrangement of mitochondria, from cell to cell, does this localizaiton vary a lot or remain constant as in the mouse sperm? It's also interesting to see if the actin structure changes when mitochrondria get disrupted. The super-resolution imaging technique along with TEM can still be employed to study those questions. Sperm from multiple species such as bull, guinea pig and human can be collected to examine both the actin and mitochondria arrangements. Dual-color super-resolution imaging of both targets as performed by using SIM are recommended. Another modified STORM technique called direct STORM for two color imaging can also be attempted to achieve the potential better resolution compared to SIM. In the direct STORM, two photoswitchable fluorescent probes Alexa Fluor 647 and Alexa Fluor 700 with great blinking optical property are used for a single laser line excitation [160]. Based on the principal of spectral demixing, the localization between two targets can be differentiated with the proper dichroics and bandpass emission filters [160]. One problem worth pointing out is that human sperm has smaller size in comparison to mouse sperm we have imaged, which poses the challenge to the resolution that's required to resolve the sub-cellular structure at even smaller scale. An optimized STORM buffer using the COT (polyunsaturated hydrocarbon cyclooctatetraene) has been validated that can significantly increase photon yields and thus double the resolution [161]. As for the disruption of mitochondria structure, a recent study reported that Glycerol kinase 2 is

essential for the proper arrangment of mitochondria during mouse spermatogenesis [162]. The Glycerol kinase 2-deficient mice can be generated with CRISPR/Cas9 system for the mitochondria structural disruption.

In vivo, sperm need to travel through quite a long distance in the female reproductive tract to eventually encounter the egg. During this journey, the continuous motion including both progressive motility and hyperactivation requires constant energy consumption. Since mitochrondria is known as the "powerhouse" of the cell, what could be the relation between the actin arrangement and the sperm motility? The super-resolution imaging of actin structure can be investigated by adding the actin inhibitors such as cytochalasin and latrunculin. Meanwhile, using the computer-assisted sperm analysis to analyze the motility change during the capacitation under actin inhibiting conditions. Why does the mitochrondria form this highly specialized helical structure at the first place? Is it related to the energy efficiency? The energy needed for the entire journey of sperm searching process seems massive. Does the mitochondria play solo in supporting the energy supply during this process? The ATP content can be measured in both wild type sperm and Glycerol kinase 2-deficient sperm through bioluminescence to initiate the study [162, 163].

Spermatogenesis is the process for sperm to finish the morphological differentiation. But they are unable to move progressively until they complete the first phase of post-testicular maturation that takes place in the epidydimis. There are two epidiydimal segments, caput and cauda, containing the immatured sperm and matured sperm respectively [164]. Is it possible that the actin cytoskeleton of sperm from these two segments exhibits a different structure due to the change of motility competence? The sperm from these two different segments can be harvested, then the super-resolution imaging of actin cytoskeleton can be initiated.

Earlier in 1992, a study has already pointed out that the human sperm quality has been going down over the past 50 years [165]. As we step into the new era, the new factors that contribute to this decline are also emerging, including the environmental pollutions, endocrine disrupting chemicals, the potential side effects of new products and changing lifestyles. Two more recent studies have addressed the issue once again. From 2002 to 2017, first study showed that the percentage

of patients with a high motile sperm count dropped from 84.7 percent to 79.1 percent, while the percentage of males with a low sperm count rose from 8.9 percent to 11.6 percent [166]. The other study analyzed the total sperm count, concentration and total motile sperm count from more than 120,000 samples over 11 years and all three measurements show the decreasing over time [167]. Taken together, those numbers are suggesting that men are experincing further decreases in viable sperm. As a result of that, the number of men seeking treatment increased 7 folds from 2002 to 2017, including the *in vitro* fertilization treatment. However, the live birth rate for each IVF cycle is not high and this succeful rate decreases with aging. The not very promising outcome exert the pressure on the infertile populations, let alone the high cost for a single IVF cycle.

Furthermore, it has been proposed that male factor infertility may serve as a biomarker of overall health status for men. The possible health risks lie in the four aspects: mental health, cardiovascular disease, diabetes as well as primary genitourinary malignancies such as testicular and prostate cancer [168]. The psychologic distress has been considered as a likely factor for causing the mental issues for infertile men. On top of that, men with infertility display decreased level of testosterone level and elevated level of cortisol and prolactin resulting in the hormonal imbalance that is associated with increased rates of anxiety and depression [168]. Meanwhile, the low testosterone level has been shown to link with the cause of worsen obesity, which leads to the negative cardiovascular effects [168]. This abnormalities of hormones also significally increase the risk to develop diabetes among infertile men [168]. Lastly, studies have found that infertile men has 52% higher risk compared to the fertile men to develop testicular cancer [169].

In 2019, The Access to Infertility Treatment and Care Act has been introduced in the House and the Senate of United States, demanding the coverage for the treatment of infertilty to be included in all health plans. Overall, the subfertility and infertility issues now have emerged as a new “public health concern”. It indeed addresses the significance and necessity to study the sperm capacitation process, a critial step for gaining the fertilization capability, for the improvement of both *in vitro* and *in vivo* treatments and furthermore the ultimate solution to this century problem.

Bibliography

[1] P. E. Visconti, Dario Krapf, and et al. Ion channels, phosphorylation and mammalian sperm capacitation. *Asian journal of andrology*, 2011.

[2] M.G. Buffone, E.V. Wertheimer, P.E. Visconti, and D. Krapf. Central role of soluble adenylyl cyclase and camp in sperm physiology. *Biochimica Et Biophysica Acta (BBA)-Molecular Basis of Disease*, 1842(12):2610–2620, 2014.

[3] M. C. Chang. Fertilizing capacity of spermatozoa deposited into the fallopian tubes. *Nature*, 168(4277):697, 1951.

[4] C. R. Austin. The 'capacitation'of the mammalian sperm. *Nature*, 170(4321):326, 1952.

[5] Susan S Suarez. Control of hyperactivation in sperm. *Human reproduction update*, 2008.

[6] R Yanagimachi. Fertility of mammalian spermatozoa: its development and relativity. *Zygote*, 1994.

[7] H.H. Chowdhury, M.R. Popoff, and R. Zorec. Actin cytoskeleton depolymerization with clostridium spiroforme toxin enhances the secretory activity of rat melanotrophs. *The Journal of physiology*, 521(2):389–395, 1999.

[8] C. Ehre, A.H. Rossi, L.H. Abdullah, K. De Pestel, S. Hill, J.C. Olsen, and C.W. Davis. Barrier role of actin filaments in regulated mucin secretion from airway goblet cells. *American Journal of Physiology-Cell Physiology*, 288(1):C46–C56, 2005.

[9] S. Gasman, S. Chasserot-Golaz, M. Malacombe, M. Way, and M.F. Bader. Regulated exocytosis in neuroendocrine cells: a role for subplasmalemmal cdc42/n-wasp-induced actin filaments. *Molecular biology of the cell*, 15(2):520–531, 2004.

[10] S. Muallem, K. Kwiatkowska, X. Xu, and H.L. Yin. Actin filament disassembly is a sufficient final trigger for exocytosis in nonexcitable cells. *The Journal of cell biology*, 128(4):589–598, 1995.

[11] Ephraim Brener, Sara Rubinstein, Gili Cohen, Keren Shternall, Joel Rivlin, and Haim Breitbart. Remodeling of the actin cytoskeleton during mammalian sperm capacitation and acrosome reaction. *Biol Reprod*, 68(3):837–845, 2003.

[12] Ana Romarowski, María A Battistone, Florenza A La Spina, Lis del C Puga Molina, Guillermina M Luque, Alejandra M Vitale, Patricia S Cuasnicu, Pablo E Visconti, Darío Krapf, and Mariano G Buffone. PKA-dependent phosphorylation of LIMK1 and Cofilin is essential for mouse sperm acrosomal exocytosis. *Dev Biol*, 405(2):237–249, 2015.

[13] B. Spungin, I. Margalit, and H. Breitbart. Sperm exocytosis reconstructed in a cell-free system: evidence for the involvement of phospholipase c and actin filaments in membrane fusion. *Journal of cell science*, 108(6):2525–2535, 1995.

[14] J. A. Cooper. Effects of cytochalasin and phalloidin on actin. *The Journal of cell biology*, 105(4):1473–1478, 1987.

[15] J. Vandekerckhove, A. Deboben, M. Nassal, and T. Wieland. The phalloidin binding site of f-actin. *The EMBO journal*, 4(11):2815–2818, 1985.

[16] B. Visegrády, D. Lorinczy, G. Hild, B. Somogyi, and M. Nyitrai. The effect of phalloidin and jasplakinolide on the flexibility and thermal stability of actin filaments. *FEBS letters*, 565(1–3):163–166, 2004.

[17] S. Kleinboelting, A. Diaz, S. Moniot, J. van den Heuvel, M. Weyand, L.R. Levin, J. Buck, and C. Steegborn. Crystal structures of human soluble adenylyl cyclase reveal mechanisms of catalysis and of its activation through bicarbonate. *Proceedings of the National Academy of Sciences*, 111(10):3727–3732, 2014.

[18] Y. Chen, M.J. Cann, T.N. Litvin, V. Iourgenko, M.L. Sinclair, L.R. Levin, and J. Buck. Soluble adenylyl cyclase as an evolutionarily conserved bicarbonate sensor. *Science*, 289(5479):625–628, 2000.

[19] C. Stival, L.D.C.P. Molina, B. Paudel, M.G. Buffone, P.E. Visconti, and D. Krapf. Sperm capacitation and acrosome reaction in mammalian sperm. *Sperm Acrosome Biogenesis and Function During Fertilization*, pages 93–106, 2016.

[20] B. M. Gadella and A. Boerke. An update on post-ejaculatory remodeling of the sperm surface before mammalian fertilization. *Theriogenology*, 2015.

[21] J.C. Chávez, P.E. Visconti, C.M. Santi, and et al. Ion permeabilities in mouse sperm reveal an external trigger for slo3-dependent hyperpolarization. *PloS one*, 2013.

[22] E.O. Hernández-González, J. Sosnik, J. Edwards, J.J. Acevedo, I. Mendoza-Lujambio, I. López-González, I. Demarco, E. Wertheimer, A. Darszon, and P.E. Visconti. Sodium and epithelial sodium channels participate in the regulation of the capacitation-associated hyperpolarization in mouse sperm. *Journal of Biological Chemistry*, 281(9):5623–5633, 2006.

[23] P.E. Visconti, J.L. Bailey, G.D. Moore, D. Pan, P. Olds-Clarke, and G.S. Kopf. Capacitation of mouse spermatozoa. i. correlation between the capacitation state and protein tyrosine phosphorylation. *Development*, 121(4):1129–1137, 1995.

[24] Sri Rama Prasanna Pavani, Michael A Thompson, Julie S Biteen, Samuel J Lord, Na Liu, Robert J Twieg, Rafael Piestun, and WE Moerner. Three-dimensional, single-molecule fluorescence imaging beyond the diffraction limit by using a double-helix point spread function. *Proceedings of the National Academy of Sciences*, 106(9):2995–2999, 2009.

[25] Jessye Wojtusik and et al. Pretreatment with cholesterol-loaded cyclodextrins prevents loss of motility associated proteins during cryopreservation of addra gazelle (nanger dama ruficollis) spermatozoa. *Cryobiology*, 2018.

[26] Katey K.and Jeremy C. Simpsonl McKayed. Actin in action: imaging approaches to study cytoskeleton structure and function. *Cells*, 2013.

[27] R. Yanagimachi. Mammalian fertilization. *The Phyisiology of Reproduction.*, 1:189–317, 1994.

[28] Melissa L. Vadnais, Angel M. Lin, and George L. Gerton. Mitochondrial fusion protein mfn2 interacts with the mitostatin-related protein mns1 required for mouse sperm flagellar structure and function. *Cilia*, 2014.

[29] E. M. Eddy and D. O' Brien. Knobil and neills physiology of reproduction. *Elsevier*, 2006.

[30] Charles B Lindemann and Kathleen A Lesich. Functional anatomy of the mammalian sperm flagellum. *Cytoskeleton*, 2016.

[31] Hiroki Otani, Osamu Tanaka, Kei-Ichiro Kasai, and Takafumi Yoshioka. Development of mitochondrial helical sheath in the middle piece of the mouse spermatid tail: regular dispositions and synchronized changes. *Anat Rec*, 222(1):26–33, 1988.

[32] A. Chandra, C.E. Copen, and E.H. Stephen. Infertility service use in the united states: data from the national survey of family growth. *National health statistics reports*, 73, 2014.

[33] Alexandros Pertsinidis, Zhang Yunxiang, and Chu Steven. Subnanometre single-molecule localization, registration and distance measurements. *Nature*, 2010.

[34] Bo Huang, Wenqin Wang, Mark Bates, and Xiaowei Zhuang. Three-dimensional super-resolution imaging by stochastic optical reconstruction microscopy. *Science*, 319(5864):810–813, 2008.

[35] X. Zhang and Z. Liu. Superlenses to overcome the diffraction limit. *Nature materials*, 7(6):435, 2008.

[36] I. Izeddin, M. El Beheiry, J. Andilla, D. Ciepielewski, X. Darzacq, and M. Dahan. Psf shaping using adaptive optics for three-dimensional single-molecule super-resolution imaging and tracking. *Optics Express*, 20(5), 2012.

[37] G. Clouvel, A. Jasaitis, and X. Levecq. Quasi-isotropic nanometric 3d resolution of palm/storm with the help of micao 3dsr. *Imagine Optics*, 2015.

[38] Martin Ovesný, Pavel Křížek, Josef Borkovec, Zdeněk Švindrych, and Guy M Hagen. ThunderSTORM: a comprehensive ImageJ plug-in for PALM and STORM data analysis and super-resolution imaging. *Bioinformatics*, 30(16):2389–2390, 2014.

[39] M.G. Gervasi, X. Xu, B. Carbajal-Gonzalez, M.G. Buffone, P.E. Visconti, and D. Krapf. The actin cytoskeleton of the mouse sperm flagellum is organized in a helical structure. *J Cell Sci*, 131(11), 2018.

[40] A. Romarowski, Á.G.V. Félix, P.T. Rodríguez, M.G. Gervasi, X. Xu, G.M. Luque, G. Contreras-Jiménez, C. Sánchez-Cárdenas, H.V. Ramírez-Gómez, D. Krapf, and P.E. Visconti. Super-resolution imaging of live sperm reveals dynamic changes of the actin cytoskeleton during acrosomal exocytosis. *J Cell Sci*, 131(21), 2018.

[41] Kiyotaka Tomshimori and Edward M Eddy. The spermatozoon. In *Knobil and Neill's physiology of reproduction, 4th edition*, volume 1, chapter 3, pages 99–148. Elsevier Academic Press, San Diego, 2015.

[42] Michael J Bouchard, Yangzhang Dong, Brian M McDermott, Du-Hung Lam, Kristy R Brown, Michael Shelanski, Anthony R Bellvé, and Vincent R Racaniello. Defects in nuclear and cytoskeletal morphology and mitochondrial localization in spermatozoa of mice lacking nectin-2, a component of cell-cell adherens junctions. *Mol Cell Biol*, 20(8):2865–2873, 2000.

[43] Héctor E Chemes, Santiago Brugo, Fernando Zanchetti, Carlos Carrere, and Juan C Lavieri. Dysplasia of the fibrous sheath: an ultrastructural defect of human spermatozoa associated with sperm immotility and primary sterility. *Fertil Steril*, 48(4):664–669, 1987.

[44] Holger Kissel, Maria-Magdalena Georgescu, Sarit Larisch, Katia Manova, Gary R Hunnicutt, and Hermann Steller. The Sept4 septin locus is required for sperm terminal differentiation in mice. *Dev Cell*, 8(3):353–364, 2005.

[45] Kiyoshi Miki, William D Willis, Paula R Brown, Eugenia H Goulding, Kerry D Fulcher, and Edward M Eddy. Targeted disruption of the Akap4 gene causes defects in sperm flagellum and motility. *Dev Biol*, 248(2):331–342, 2002.

[46] Gary E Olson, Virginia P Winfrey, Subir K NagDas, Kristina E Hill, and Raymond F Burk. Selenoprotein P is required for mouse sperm development 1. *Biol Reprod*, 73(1):201–211, 2005.

[47] Ana Romarowski, Guillermina M Luque, Florenza A La Spina, Dario Krapf, and Mariano G Buffone. Role of actin cytoskeleton during mammalian sperm acrosomal exocytosis. In *Sperm Acrosome Biogenesis and Function During Fertilization*, pages 129–144. Springer, 2016.

[48] Diego Krapf. Compartmentalization of the plasma membrane. *Current opinion in cell biology*, pages 15–21, 2018.

[49] Kenneth G Campellone and Matthew D Welch. A nucleator arms race: cellular control of actin assembly. *Nat Rev Mol Cell Biol*, 11(4):237–251, 2010.

[50] Samuel E Lux. Anatomy of the red cell membrane skeleton: unanswered questions. *Blood*, 127(2):187–199, 2016.

[51] Ke Xu, Guisheng Zhong, and Xiaowei Zhuang. Actin, spectrin, and associated proteins form a periodic cytoskeletal structure in axons. *Science*, 339(6118):452–456, 2013.

[52] Nicholas L Andrews, Keith A Lidke, Janet R Pfeiffer, Alan R Burns, Bridget S Wilson, Janet M Oliver, and Diane S Lidke. Actin restricts FcϵRI diffusion and facilitates antigen-induced receptor immobilization. *Nat Cell Biol*, 10(8):955–963, 2008.

[53] Sanaz Sadegh, Jenny L Higgins, Patrick C Mannion, Michael M Tamkun, and Diego Krapf. Plasma membrane is compartmentalized by a self-similar cortical actin meshwork. *Phys Rev X*, (7):011031, 2017.

[54] W.G Breed and C.M Leigh. Distribution of filamentous actin in and around spermatids and in spermatozoa of Australian conilurine rodents. *Mol Reprod Dev*, 30(4):369–384, 1991.

[55] Jean-Pierre Fouquet and Marie-Louise Kann. Species-specific localization of actin in mammalian spermatozoa: Factor artifact? *Microsc Res Tech*, 20(3):251–258, 1992.

[56] Haim Breitbart, Gili Cohen, and Sara Rubinstein. Role of actin cytoskeleton in mammalian sperm capacitation and the acrosome reaction. *Reproduction*, 129(3):263–268, 2005.

[57] Sarit Bar-Sheshet Itach, Maya Finklestein, Nir Etkovitz, and Haim Breitbart. Hyper-activated motility in sperm capacitation is mediated by phospholipase D-dependent actin polymerization. *Dev Biol*, 362(2):154–161, 2012.

[58] Julia Riedl, Kevin C Flynn, Aurelia Raducanu, Florian Gärtner, Gisela Beck, Michael Bösl, Frank Bradke, Steffen Massberg, Attila Aszodi, Michael Sixt, et al. Lifeact mice for studying F-actin dynamics. *Nat Methods*, 7(3):168–169, 2010.

[59] Sean P Flaherty, Virginia P Winfrey, and Gary E Olson. Localization of actin in mammalian spermatozoa: a comparison of eight species. *Anat Rec*, 216(4):504–515, 1986.

[60] Mark Bates, Bo Huang, and Xiaowei Zhuang. Super-resolution microscopy by nanoscale localization of photo-switchable fluorescent probes. *Curr Opin Chem Biol*, 12(5):505–514, 2008.

[61] Antonio Alvau, Maria Agustina Battistone, Maria Gracia Gervasi, Felipe A Navarrete, Xinran Xu, Claudia Sánchez-Cárdenas, Jose Luis De la Vega-Beltran, Vanina G Da Ros, Peter A Greer, Alberto Darszon, et al. The tyrosine kinase FER is responsible for the capacitation-associated increase in tyrosine phosphorylation in murine sperm. *Development*, 143(13):2325–2333, 2016.

[62] Jean-Ju Chung, Sang-Hee Shim, Robert A Everley, Steven P Gygi, Xiaowei Zhuang, and David E Clapham. Structurally distinct Ca^{+2} signaling domains of sperm flagella orchestrate tyrosine phosphorylation and motility. *Cell*, 157(4):808–822, 2014.

[63] Anthony J Baines. The spectrin–ankyrin–4.1–adducin membrane skeleton: adapting eukaryotic cells to the demands of animal life. *Protoplasma*, 244(1-4):99–131, 2010.

[64] William A Anong, Taina Franco, Haiyan Chu, Tahlia L Weis, Emily E Devlin, David M Bodine, Xiuli An, Narla Mohandas, and Philip S Low. Adducin forms a bridge between the erythrocyte membrane and its cytoskeleton and regulates membrane cohesion. *Blood*, 114(9):1904–1912, 2009.

[65] Don W Fawcett. The mammalian spermatozoon. *Dev Biol*, 44(2):394–436, 1975.

[66] Fumie Suzuki-Toyota, Chizuru Ito, Yoshiro Toyama, Mamiko Maekawa, Ryoji Yao, Tetsuo Noda, and Kiyotaka Toshimori. The coiled tail of the round-headed spermatozoa appears during epididymal passage in GOPC-deficient mice. *Arch Histol Cytol*, 67(4):361–371, 2004.

[67] Fiore Pelliccione, Alessandro Micillo, Giuliana Cordeschi, Anatolia DâĂŹAngeli, Stefano Necozione, Loredana Gandini, Andrea Lenzi, Felice Francavilla, and Sandro Francavilla. Altered ultrastructure of mitochondrial membranes is strongly associated with unexplained asthenozoospermia. *Fertil Steril*, 95(2):641–646, 2011.

[68] Han-Chen Ho and Shiuan Wey. Three dimensional rendering of the mitochondrial sheath morphogenesis during mouse spermiogenesis. *Microsc Res Tech*, 70(8):719–723, 2007.

[69] Alexander R Paredez, Zoe June Assaf, David Sept, Ljudmilla Timofejeva, Scott C Dawson, Chung-Ju Rachel Wang, and WZ Cande. An actin cytoskeleton with evolutionarily conserved functions in the absence of canonical actin-binding proteins. *Proc Natl Acad Sci USA*, 108(15):6151–6156, 2011.

[70] Gary E. Olson and Virginia P. Winfrey. Identification of a cytoskeletal network adherent to the mitochondria of mammalian spermatozoa. *Journal of ultrastructure and molecular structure research*, pages 131–139, 1986.

[71] Gary E. Olson and Virginia P. Winfrey. Mitochondria-cytoskeleton interactions in the sperm midpiece. *Journal of structural biology*, pages 13–22, 1990.

[72] Istvan R Boldogh and Liza A Pon. Interactions of mitochondria with the actin cytoskeleton. *BBA Mol Cell Res*, 1763(5):450–462, 2006.

[73] Steffen Mueller, Thomas A Rosenquist, Yoshimi Takai, Richard A Bronson, and Eckard Wimmer. Loss of nectin-2 at Sertoli-spermatid junctions leads to male infertility and correlates with severe spermatozoan head and midpiece malformation, impaired binding to the zona pellucida, and oocyte penetration. *Biol Reprod*, 69(4):1330–1340, 2003.

[74] Beata Machnicka, Aleksander Czogalla, Anita Hryniewicz-Jankowska, Dżamila M Bogusławska, Renata Grochowalska, Elżbieta Heger, and Aleksander F Sikorski. Spectrins: a structural platform for stabilization and activation of membrane channels, receptors and transporters. *BBA-Biomembranes*, 1838(2):620–634, 2014.

[75] Dennis E Discher and Philippe Carl. New insights into red cell network structure, elasticity, and spectrin unfolding-a current review. *Cell Mol Biol Lett*, 6(3):593–606, 2001.

[76] Enrique Othón Hernández-González, Alba Neri Lecona-Valera, Jaime Escobar-Herrera, and Adela Mújica. Involvement of an F-actin skeleton on the acrosome reaction in guinea pig spermatozoa. *Cytoskeleton*, 46(1):43–58, 2000.

[77] Ahmed Yagi and Jorma Paranko. Actin, α-actinin, and spectrin with specific associations with the postacrosomal and acrosomal domains of bovine spermatozoa. *Anat Rec*, 241(1):77–87, 1995.

[78] María Gracia Gervasi and Pablo E. Visconti. Chang's meaning of capacitation: A molecular perspective. *Mol Reprod Dev*, 83(10):860–874, 2016.

[79] Sarah D Olson, Susan S Suarez, and Lisa J Fauci. Coupling biochemistry and hydrodynamics captures hyperactivated sperm motility in a simple flagellar model. *J Theor Biol*, 283(1):203–216, 2011.

[80] Haruhiko Miyata, Yuhkoh Satouh, Daisuke Mashiko, Masanaga Muto, Kaori Nozawa, Kogiku Shiba, Yoshitaka Fujihara, Ayako Isotani, Kazuo Inaba, and Masahito Ikawa. Sperm calcineurin inhibition prevents mouse fertility with implications for male contraceptive. *Science*, 350(6259):442–445, 2015.

[81] Xiaolin Li, Yoichiro Matsuoka, and Vann Bennett. Adducin preferentially recruits spectrin to the fast growing ends of actin filaments in a complex requiring the MARCKS-related domain and a newly defined oligomerization domain. *J Biol Chem*, 273(30):19329–19338, 1998.

[82] Jean-Ju Chung, Miki Kiyoshi, Kim Doory, Shim Sang-Hee, Shi Huanan F, Hwang Jae Yeon, Cai Xinjiang, Iseri Yusuf, Zhuang Xiaowei, and Clapham David E. Catsperζ regulates the structural continuity of sperm ca^{2+} signaling domains and is required for normal fertility. *Elife*, 2017.

[83] Esther E Noiles, Kathleen A Thompson, and Bayard T Storey. Water permeability, Lp, of the mouse sperm plasma membrane and its activation energy are strongly dependent on interaction of the plasma membrane with the sperm cytoskeleton. *Cryobiology*, 35(1):79–92, 1997.

[84] Diego Krapf, Grace Campagnola, Kanti Nepal, and Olve B Peersen. Strange kinetics of bulk-mediated diffusion on lipid bilayers. *Phys Chem Chem Phys*, 18(18):12633–12641, 2016.

[85] A. V. Weigel, B. Simon, M. M. Tamkun, and D. Krapf. Ergodic and nonergodic processes coexist in the plasma membrane as observed by single-molecule tracking. *Proc Natl Acad Sci USA*, 108(16):6438–6443, 2011.

[86] G. Clouvel, A. Jasaitis, J. Sillibourne, I. Izeddin, M. El Beheiry, X. Levecq, M. Dahan, M. Bornens, and X. Darzacq. Dual-color 3d palm/dstorm imaging of centrosomal proteins using micao 3dsr. *Single Molecule Spectroscopy and Superresolution Imaging VI*, 8590, 2013.

[87] M. Marbouty, A. Le Gall, D.I. Cattoni, A. Cournac, A. Koh, J.B. Fiche, J. Mozziconacci, H. Murray, R. Koszul, and M. Nollmann. Condensin-and replication-mediated bacterial chromosome folding and origin condensation revealed by hi-c and super-resolution imaging. *Molecular Cell*, 59(4), 2015.

[88] C. Stival, C. Ritagliati, X. Xu, M.G. Gervasi, G.M. Luque, C.B. Graf, J.L. De la Vega-Beltrán, N. Torres, A. Darszon, D. Krapf, and M.G. Buffone. Disruption of protein kinase a localization induces acrosomal exocytosis in capacitated mouse sperm. *Journal of Biological Chemistry*, 293(24):9435–9447, 2018.

[89] J. Escoffier, F. Navarrete, D. Haddad, C.M. Santi, A. Darszon, and P.E. Visconti. Flow cytometry analysis reveals that only a subpopulation of mouse sperm undergoes hyperpolarization during capacitation. *Biology of reproduction*, 92(5), 2015.

[90] C. Stival, F.A. La Spina, C.B. Graf, E. Arcelay, S.E. Arranz, J.J. Ferreira, S. Le Grand, V.A. Dzikunu, C.M. Santi, P.E. Visconti, and M.G. Buffone. Src kinase is the connecting player between protein kinase a (pka) activation and hyperpolarization through slo3 potas-

sium channel regulation in mouse sperm. *Journal of Biological Chemistry*, 290(30):18855–18864, 2015.

[91] O. Torres-Quesada, J.E. Mayrhofer, and E. Stefan. The many faces of compartmentalized pka signalosomes. *Cellular signalling*, pages 1–11, 2017.

[92] X. Li, X. Wang, and M. Snyder. Systematic investigation of proteinâĂŞsmall molecule interactions. *IUBMB life*, 65(1):2–8, 2013.

[93] S.S. Taylor, R. Ilouz, P. Zhang, and A.P. Kornev. Assembly of allosteric macromolecular switches: lessons from pka. *Nature reviews Molecular cell biology*, 13(10):646, 2012.

[94] D.W. Carr, Z.E. Hausken, I.D. Fraser, R.E. Stofko-Hahn, and J.D. Scott. Association of the type ii camp-dependent protein kinase with a human thyroid rii-anchoring protein. cloning and characterization of the rii-binding domain. *Journal of Biological Chemistry*, 267(19):13376–13382, 1992.

[95] R.A.P. Harrison. Rapid pkaâĂŘcatalysed phosphorylation of boar sperm proteins induced by the capacitating agent bicarbonate. *Molecular Reproduction and Development: Incorporating Gamete Research*, 67(3):337–352, 2004.

[96] P.E. Visconti, G.D. Moore, J.L. Bailey, P. Leclerc, S.A. Connors, D. Pan, P. Olds-Clarke, and G.S. Kopf. Capacitation of mouse spermatozoa. ii. protein tyrosine phosphorylation and capacitation are regulated by a camp-dependent pathway. *Development*, 121(4):1139–1150, 1995.

[97] E. Baldi, M. Luconi, L. Bonaccorsi, and G. Forti. Signal transduction pathways in human spermatozoa. *Journal of reproductive immunology*, 53(1–2):121–131, 2002.

[98] S. Ficarro, O. Chertihin, V.A. Westbrook, F. White, F. Jayes, P. Kalab, J.A. Marto, J. Shabanowitz, J.C. Herr, D.F. Hunt, and P.E. Visconti. Phosphoproteome analysis of capacitated human sperm evidence of tyrosine phosphorylation of a kinase-anchoring protein 3

and valosin-containing protein/p97 during capacitation. *Journal of Biological Chemistry*, 278(13):11579–11589, 2003.

[99] T.W. Ijiri, A.K.M. Mahbub Hasan, and K.I. Sato. Protein-tyrosine kinase signaling in the biological functions associated with sperm. *Journal of signal transduction*, 2012.

[100] G.J. Mohanarao and S.K. Atreja. Identification of capacitation associated tyrosine phosphoproteins in buffalo (bubalus bubalis) and cattle spermatozoa. *Animal reproduction science*, 123(1–2):40–47, 2011.

[101] S.C. Roy and S.K. Atreja. Tyrosine phosphorylation of a 38âĂŘkda capacitationâĂŘassociated buffalo (bubalus bubalis) sperm protein is induced by lâĂŘarginine and regulated through a camp/pkaâĂŘindependent pathway. *International journal of andrology*, 31(1):12–24, 2008.

[102] J. Signorelli, E.S. Diaz, and P. Morales. Kinases, phosphatases and proteases during sperm capacitation. *Cell and tissue research*, 349(3):765–782, 2012.

[103] M.A. Baker, L. Hetherington, and R.J. Aitken. Identification of src as a key pka-stimulated tyrosine kinase involved in the capacitation-associated hyperactivation of murine spermatozoa. *Journal of Cell Science*, 119(15):3182–3192, 2006.

[104] D. Krapf, E. Arcelay, E.V. Wertheimer, A. Sanjay, S.H. Pilder, A.M. Salicioni, and P.E. Visconti. Inhibition of ser/thr phosphatases induces capacitation-associated signaling in the presence of src kinase inhibitors. *Journal of Biological Chemistry*, 285(11):7977–7985, 2010.

[105] G. Varano, A. Lombardi, G. Cantini, G. Forti, E. Baldi, and M. Luconi. Src activation triggers capacitation and acrosome reaction but not motility in human spermatozoa. *Human reproduction*, 23(12):2652–2662, 2008.

[106] J. Luo, V. Gupta, B. Kern, J.S. Tash, G. Sanchez, G. Blanco, and W.H. Kinsey. Role of fyn kinase in spermatogenesis: defects characteristic of fyn-null sperm in mice. *Biology of reproduction*, 86(1):22–1, 2012.

[107] M.A. Baker, L. Hetherington, B. Curry, and R.J. Aitken. Phosphorylation and consequent stimulation of the tyrosine kinase c-abl by pka in mouse spermatozoa; its implications during capacitation. *Developmental biology*, 333(1):57–66, 2009.

[108] M.A. Battistone, A. Alvau, A.M. Salicioni, P.E. Visconti, V.G. Da Ros, and P.S. Cuasnicu. Evidence for the involvement of proline-rich tyrosine kinase 2 in tyrosine phosphorylation downstream of protein kinase a activation during human sperm capacitation. *Molecular human reproduction*, 20(11):1054–1066, 2014.

[109] L. González-Fernández, B. Macías-García, S.C. Loux, D.D. Varner, and K. Hinrichs. Focal adhesion kinases and calcium/calmodulin-dependent protein kinases regulate protein tyrosine phosphorylation in stallion sperm. *Biology of reproduction*, 88(6):138–1, 2013.

[110] B. Huang, S.A. Jones, B. Brandenburg, and X. Zhuang. Whole-cell 3d storm reveals interactions between cellular structures with nanometer-scale resolution. nature methods. *Nature methods*, 5(12):1047, 2008.

[111] M.J. Rust, M. Bates, and X. Zhuang. Sub-diffraction-limit imaging by stochastic optical reconstruction microscopy (storm). *Nature methods*, 3(10):793, 2006.

[112] I.A. Simpson, D. Dwyer, D. Malide, K.H. Moley, A. Travis, and S.J. Vannucci. The facilitative glucose transporter glut3: 20 years of distinction. *American Journal of Physiology-Endocrinology and Metabolism*, 295(2):242–253, 2008.

[113] F. Narciandi, B. Fernandez-Fuertes, I. Khairulzaman, H. Jahns, D. King, E.K. Finlay, K.H. Mok, S. Fair, P. Lonergan, C.O. Farrelly, and K.G. Meade. Sperm-coating beta-defensin 126 is a dissociation-resistant dimer produced by epididymal epithelium in the bovine reproductive tract. *Biology of reproduction*, 95(6):121–1, 2016.

[114] E. Wertheimer, D. Krapf, L. JosÃl', C. SÃąnchez-CÃąrdenas, F. Navarrete, D. Haddad, J. Escoffier, A.M. Salicioni, L.R. Levin, J. Buck, and J. Mager. Compartmentalization of distinct camp signaling pathways in mammalian sperm. *Journal of Biological Chemistry*, 288(49):35307–35320, 2013.

[115] H. Qi, M.M. Moran, B. Navarro, J.A. Chong, G. Krapivinsky, L. Krapivinsky, Y. Kirichok, I.S. Ramsey, T.A. Quill, and D.E. Clapham. All four catsper ion channel proteins are required for male fertility and sperm cell hyperactivated motility. *Proceedings of the National Academy of Sciences*, 104(4):1219–1223, 2007.

[116] M.A. Nolan, D.F. Babcock, G. Wennemuth, W. Brown, K.A. Burton, and G.S. McKnight. Sperm-specific protein kinase a catalytic subunit cα2 orchestrates camp signaling for male fertility. *Proceedings of the National Academy of Sciences*, 101(37):13483–13488, 2004.

[117] T.H. Hereng, P.H. Backe, J. Kahmann, C. Scheich, M. Bjørås, B.S. Skålhegg, and K.R. Rosendal. Structure and function of the human sperm-specific isoform of protein kinase a (pka) catalytic subunit cα2. *Journal of structural biology*, 178(3):300–310, 2012.

[118] A.W. Craig, R. Zirngibl, K. Williams, L.A. Cole, and P.A. Greer. Mice devoid of fer protein-tyrosine kinase activity are viable and fertile but display reduced cortactin phosphorylation. *Molecular and cellular biology*, 21(2):603–613, 2001.

[119] V.G. Da Ros, M.W. Muñoz, M.A. Battistone, N.G. Brukman, G. Carvajal, L. Curci, M.D. Gómez-Elías, D.J. Cohen, and P.S. Cuasnicú. From the epididymis to the egg: participation of crisp proteins in mammalian fertilization. *Asian journal of andrology*, 17(5):711, 2015.

[120] V.G. Da Ros, W.D. Maldera, J.A. amd Willis, D.J. Cohen, E.H. Goulding, D.M. Gelman, M. Rubinstein, E.M. Eddy, and P.S. Cuasnicu. Impaired sperm fertilizing ability in mice lacking cysteine-rich secretory protein 1 (crisp1). *Developmental biology*, 320(1):12–8, 2008.

[121] M.C. Chang. Fertilizing capacity of spermatozoa deposited into the fallopian tubes. *Nature*, 168(4277):697, 1951.

[122] C. R. Austin. The âĂŸcapacitationâĂŹof the mammalian sperm. *Nature*, 170(4321):326, 1952.

[123] S. S. Suarez and H. C. Ho. Hyperactivation of mammalian sperm. *CELLULAR AND MOLECULAR BIOLOGY-PARIS-WEGMANN*, 49(3):351–356, 2003.

[124] R.P. Demott and S.S. Suarez. Hyperactivated sperm progress in the mouse oviduct. *Biology of reproduction*, 46(5):779–785, 1992.

[125] C.R. Stauss, T.J. Votta, and S.S. Suarez. Sperm motility hyperactivation facilitates penetration of the hamster zona pellucida. *Biology of reproduction*, 53(6):1280–1285, 1995.

[126] D. Ren, B. Navarro, G. Perez, A.C. Jackson, S. Hsu, Q. Shi, J.L. Tilly, and D.E. Clapham. A sperm ion channel required for sperm motility and male fertility. *Nature*, 413(6856):603, 2001.

[127] Y. Kirichok and P.V. Lishko. Rediscovering sperm ion channels with the patch-clamp technique. *MHR: Basic science of reproductive medicine*, 17(8):478–499, 2011.

[128] B. Navarro, Y. Kirichok, J.J. Chung, and D.E. Clapham. Ion channels that control fertility in mammalian spermatozoa. *The International journal of developmental biology*, 52:607, 2008.

[129] J. Liu, J. Xia, K.H. Cho, D.E. Clapham, and D. Ren. Catsperβ, a novel transmembrane protein in the catsper channel complex. *Journal of Biological Chemistry*, 282(26):18945–18952, 2007.

[130] J.J. Chung, B. Navarro, G. Krapivinsky, L. Krapivinsky, and D.E. Clapham. A novel gene required for male fertility and functional catsper channel formation in spermatozoa. *Nature communications*, 2:153, 2011.

[131] H. Wang, J. Liu, K.H. Cho, and D. Ren. A novel, single, transmembrane protein catsperg is associated with catsper1 channel protein. *Biology of reproduction*, 81(3):539–544, 2009.

[132] A.E. Carlson, T.A. Quill, R.E. Westenbroek, S.M. Schuh, B. Hille, and D.F. Babcock. Identical phenotypes of catsper1 and catsper2 null sperm. *Journal of Biological Chemistry*, 280(37):32238–32244, 2005.

[133] J. Jin, N. Jin, H. Zheng, S. Ro, D. Tafolla, K.M. Sanders, and W. Yan. Catsper3 and catsper4 are essential for sperm hyperactivated motility and male fertility in the mouse. *Biology of reproduction*, 77(1):37–44, 2007.

[134] M.R. Avenarius, M.S. Hildebrand, Y. Zhang, N.C. Meyer, L.L. Smith, K. Kahrizi, H. Najmabadi, and R.J. Smith. Human male infertility caused by mutations in the catsper1 channel protein. *The American Journal of Human Genetics*, 84(4):505–510, 2009.

[135] N. Avidan, H. Tamary, O. Dgany, D. Cattan, A. Pariente, M. Thulliez, N. Borot, L. Moati, A. Barthelme, L. Shalmon, and T. Krasnov. a human autosomal nonsyndromic male infertility gene. *European Journal of Human Genetics*, 11(7):497, 2003.

[136] J.F. Smith, O. Syritsyna, M. Fellous, C. Serres, N. Mannowetz, Y. Kirichok, and P.V. Lishko. Disruption of the principal, progesterone-activated sperm ca^{2+} channel in a catsper2-deficient infertile patient. *Proceedings of the National Academy of Sciences*, 110(17):6823–6828, 2013.

[137] T.A. Quill, S.A. Sugden, K.L. Rossi, L.K. Doolittle, R.E. Hammer, and D.L. Garbers. Hyperactivated sperm motility driven by catsper2 is required for fertilization. *Proceedings of the National Academy of Sciences*, 100(25):14869–14874, 2003.

[138] Y. Kirichok, B. Navarro, and D.E. Clapham. Whole-cell patch-clamp measurements of spermatozoa reveal an alkaline-activated ca^{2+} channel. *Nature*, 439(7077):737, 2006.

[139] P.V. Lishko, I.L. Botchkina, A. Fedorenko, and Y. Kirichok. Acid extrusion from human spermatozoa is mediated by flagellar voltage-gated proton channel. *Cell*, 140(3):327–337, 2010.

[140] P.V. Lishko, I.L. Botchkina, and Y. Kirichok. Progesterone activates the principal ca 2+ channel of human sperm. *Nature*, 471(7338):387, 2011.

[141] M.R. Miller, S.A. Mansell, S.A. Meyers, and P.V. Lishko. Flagellar ion channels of sperm: similarities and differences between species. *Cell calcium*, 58(1):105–113, 2015.

[142] P.V. Lishko and N. Mannowetz. Catsper: a unique calcium channel of the sperm flagellum. *Current opinion in physiology*, 2:109–113, 2018.

[143] G. Orta, J.L. de la Vega-Beltran, D. Martín-Hidalgo, C.M. Santi, P.E. Visconti, and A. Darszon. Catsper channels are regulated by protein kinase a. *Journal of Biological Chemistry*, 293(43):16830–16841, 2018.

[144] M.R. Miller, S.J. Kenny, N. Mannowetz, S.A. Mansell, M. Wojcik, S. Mendoza, R.S. Zucker, K. Xu, and P.V. Lishko. Asymmetrically positioned flagellar control units regulate human sperm rotation. *Cell reports*, 24(10):2606–2613, 2018.

[145] S. Gasman, S. Chasserot-Golaz, M. Malacombe, M. Way, and M.F. Bader. Regulated exocytosis in neuroendocrine cells: a role for subplasmalemmal cdc42/n-wasp-induced actin filaments. *Molecular biology of the cell*, 15(2):520–531, 2004.

[146] A.K. Nevins and D.C. Thurmond. Caveolin-1 functions as a novel cdc42 guanine nucleotide dissociation inhibitor in pancreatic β-cells. *Journal of Biological Chemistry*, 281(28):18961–18972, 2006.

[147] R. Baltiérrez-Hoyos, A.L. Roa-Espitia, and E.O. Hernandez-Gonzalez. The association between cdc42 and caveolin-1 is involved in the regulation of capacitation and acrosome reaction of guinea pig and mouse sperm. *Reproduction (Cambridge, England)*, 144(1):123–134, 2012.

[148] W.S. Ward and A.O. Zalensky. The unique, complex organization of the transcriptionally silent sperm chromatin. *Critical Reviews^{TM} in Eukaryotic Gene Expression*, 6:2–3, 1996.

[149] P E Visconti. Understanding the molecular basis of sperm capacitation through kinase design. *Proceedings of the National Academy of Sciences*, 2009.

[150] Felipe A. Navarrete and et al. Biphasic role of calcium in mouse sperm capacitation signaling pathways. *Journal of cellular physiology*, 2015.

[151] A. I. C. Calejo and K Taskén. Targeting protein protein interactions in complexes organized by a kinase anchoring proteins. *Frontiers in pharmacology*, 2015.

[152] J. M. Cummins and P. F. Woodall. On mammalian sperm dimensions. *Journal of Reproduction and Fertility*, 1985.

[153] B. S. Jaiswal and M. Conti. Calcium regulation of the soluble adenylyl cyclase expressed in mammalian spermatozoa. *Proceedings of the National Academy of Sciences*, 2003.

[154] S. Kirkpatrick, C. D. Gelatt, and M. P Vecchi. Optimization by simulated annealing. *science*, 1983.

[155] H. Lodish, A. Berk, S. L. Zipursky, P. Matsudaira, D. Baltimore, and J Darnell. *Molecular cell biology. Vol.3*. New York:WH Freeman, 1995.

[156] B. Efron and R. Tibshirani. Improvements on cross-validation: the 632+ bootstrap method. *Journal of the American Statistical Association*, 92(438):548–560, 1997.

[157] C. Ritagliati, G.M. Luque, C. Stival, C.B. Graf, M.G. Buffone, and D. Krapf. Lysine acetylation modulates mouse sperm capacitation. *Scientific reports*, page 8, 2018.

[158] D. Krapf, E. O'Brien, P.M. Maidagán, E.S. Morales, P.E. Visconti, and S.E. Arranz. Calcineurin regulates progressive motility activation of rhinella (bufo) arenarum sperm through dephosphorylation of pkc substrates. *Journal of cellular physiology*, 229(10):1378–1386, 2014.

[159] A.P. Sousa, A. Amaral, M. Baptista, R. Tavares, P.C. Campo, P.C. Peregrín, A. Freitas, A.and Paiva, T. Almeida-Santos, and J. Ramalho-Santos. Not all sperm are equal: functional mitochondria characterize a subpopulation of human sperm with better fertilization potential. *PloS one*, 6(3), 2011.

[160] C.M. Winterflood, E. Platonova, D. Albrecht, and H. Ewers. Dual-color 3d superresolution microscopy by combined spectral-demixing and biplane imaging. *Biophysical journal*, 109(1):3–6, 2015.

[161] N. Olivier, D. Keller, P. G´onczy, and S. Manley. Resolution doubling in 3d-storm imaging through improved buffers. *PloS one*, 8(7), 2013.

[162] K. Shimada, H. Kato, H. Miyata, and M. Ikawa. Glycerol kinase 2 is essential for proper arrangement of crescent-like mitochondria to form the mitochondrial sheath during mouse spermatogenesis. *Journal of Reproduction and Development*, 2019.

[163] G. Perchec, C. Jeulin, J. Cosson, F. Andre, and R. Billard. Relationship between sperm atp content and motility of carp spermatozoa. *Journal of cell science*, 108(2):747–753, 1995.

[164] M.G. Gervasi and P.E. Visconti. Molecular changes and signaling events occurring in spermatozoa during epididymal maturation. *Andrology*, 5(2), 2017.

[165] E. Carlsen, A. Giwercman, N. Keiding, and N.E. SkakkebÃęk. Evidence for decreasing quality of semen during past 50 years. *Bmj*, 305(6854), 1992.

[166] A.W. Tiegs, J. Landis, N. Garrido, R. Scott, and J. Hotaling. Total motile sperm count trend over time across two continents: evaluation of semen analyses from 119,972 infertile men. *Fertility and Sterility*, 110(4), 2018.

[167] S. Chang, T.G. Nazem, D. Gounko, J. Lee, N. Bar-Chama, J.M. Shamonki, C. Antonelli, and A.B. Copperman. Eleven year longitudinal study of us sperm donors demonstrates declining sperm count and motility. *Fertility and Sterility*, 110(4), 2018.

[168] S. Keihani, B. Hanson, and J.M. Hotaling. Male factor infertility: an opportunity to investigate individual and family health. *BJOG: an international journal of obstetrics & gynaecology*, 126(2):149–151, 2019.

[169] B.M. Hanson, M.L. Eisenberg, and J.M. Hotaling. Male infertility: a biomarker of individual and familial cancer risk. *Fertility and sterility*, 109(1):6–19, 2018.

[170] Y. Toyoda. Studies on the fertilization of mouse eggs in vitro. i. in vitro fertilization of eggs by fresh epididymal sperm. *Jpn. J. Anim. Reprod.*, 16:147–151, 1971.

Appendix A

Protocols

This appendix provides protocols used for the experiments presented in this thesis, including setup alignment and sample preparation. Protocols A.1 and A.6 are modified from Aubrey Weigel's thesis.

A.1 TIRF microscope alignment

Most of experiments presented in this thesis were performed in our custom-built TIRF (total internal reflection fluorescence) setup. The setup needs to be properly aligned before each experiment in order to obtain the best quality images of the sample.

1. Turn on lasers
2. Check beam alignment before the last telescope. Make sure it is centered on each mirror, lens, scope, and is not being clipped. Do this for each laser being implemented if necessary.
3. All lasers need to be co-aligned at the last telescope
4. Choose one laser in order to align the last two stirring mirrors and the focusing lens so that the laser is enters the objective centered and perpendicular
5. Remove focusing lens from path
6. Untighten main adjustment mirrors (S1 and S2)
7. Place an iris on last stand of scope before S1. Close the iris to reduce beam size to allow for easier beam alignment
8. Attach alignment tube to threads by which the objective attaches
9. Close bottom iris of the alignment tube, adjust S1 such that the highest beam brightness on ceiling is achieved.

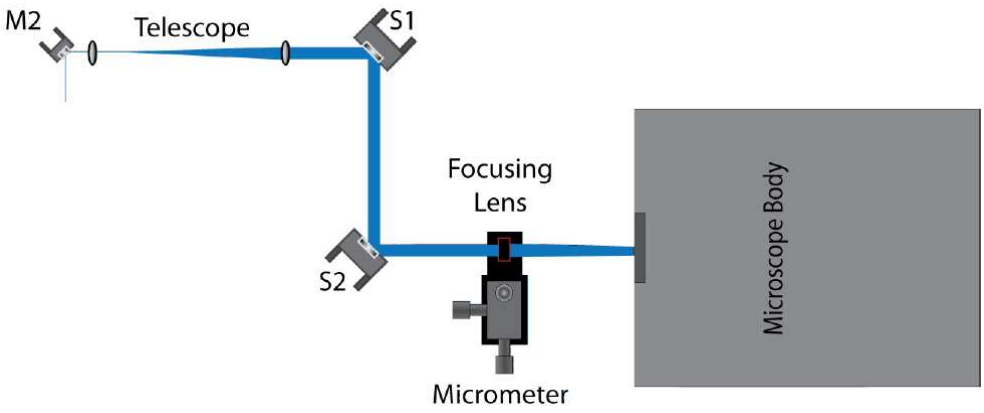

Figure A.1: General schematic of TIRF microscope. Mirrors S1 and S2 steer the beam into the focusing lens and then into the microscope. The focusing lens is on a micrometer for fine tune adjusting.

10. Open bottom iris and close the top iris of the alignment tube. Adjust S2 such that the highest beam brightness is achieved.

11. Continue alternating the adjustment between tube irises and corresponding mirrors until an optimal brightness is achieved with both iris closed.

12. Remove alignment tube, center the cross-hair on the ceiling to aligned beam as a marker for later steps. Do not touch the steering mirrors until after the focusing lens is in place.

13. Replace the focusing lens back in its positions.

14. Make sure that the reflection of the beam off the focusing lens aligns to the original beam on mirror S2

15. Use an aperture on the focusing lens and make sure the beam passes through the center using only the micrometer (do not use the steering mirrors)

16. Mount the objective. If using the objective heater you can put this on the objective now as well.

17. Re-center the laser on the ceiling using S2

18. Adjust mirror S1 to center the beam on the lens

19. Repeat steps 17 and 18 until the beam is going through the center of the focusing lens and aligned to the cross-hair on the ceiling

20. Tighten the screws on the mirror adjustment knobs to hold mirror placement. Be careful not shift the beam or mirror position while doing this

21. Remove irises

22. Check filter box to ensure the proper dichroic and filters are in place for the experiment

A.2 Mice sperm handling, capacitating and non-capacitating media

In all the experiments that sperm are needed, non-capacitating media is always required to maintain the viability of sperm before fixation and staining. Capacitating media is used to induce sperm capacitation process.

Table A.1: Reagents and corresponding concentrations for modified Toyoda-Yokoyama-Hosi sperm stock media [170]

Reagent	**[Final] mM**	**g/100 mL**
NaCl	119.3	0.6972
KCl	4.7	0.0350
KH_2PO_4	1.2	0.0163
$MgSO_4{*}7\ H_2O$	1.2	0.0296
Glucose	5.56	0.1
$CaCl_2{\cdot}2H_2O$	1.71	0.0251
HEPES	20	0.477
Gentamicin (10 mg/ml)	10 μg/ml	100 μl
Phenol Red (0.05%)	2 μl/ml	200 μl

1. Prepare 100 ml of modified sperm stock media

   (a) Dissolve all reagents (according to Table A.1) in 100 ml Milli-Q water in a beaker

Table A.2: Addition of reagents for modified 2X capacitating media

Reagent	**[Final] mM**	**in 3 ml CAP media**	**Vendor**	**Product No.**
BSA*	10 mg/ml	30 mg	Sigma	A0281
HCO_3^{-}* (e.g. $NaHCO_3$)	30 mM	7.56 mg	–	–

* *BSA and HCO_3^- are for capacitation media only! Add them the day of the experiment*

(b) Filter the mixed solution with 0.22 μm syringe filter into aliquots with 10 ml in 15 ml conical-bottom sterile centrifuge tubes

(c) Seal aliquots with parafilm, then store at 4°C. Once the conical is opened, diacard the unused media

2. other solutions preparations (on the day of harvesting sperm)

(a) Prepare sodium pyruvate solution

i. Add 15 mg $C_3H_3NaO_3$ (Sigma, P5280) in 170 μl of Milli-Q water

ii. Store at 4°C for up to 1 week

(b) Prepare NaOH solution

i. 200 mg/ml NaOH in Milli-Q water

ii. Do not store

3. Prepare non-capacitating and capacitating media for experiments of the day

(a) Non-capacitating media (7 ml)

i. Pipette 7 ml of stock media into 15 ml conical

ii. Add 1 μl/ml sodium pyruvate solution into conical

iii. Adjust pH to 7.2 - 7.4 with freshly prepared NaOH carefully

iv. Incubate in the water bath at 37°C

(b) 2X Capacitating media (3ml)

i. Pipette 3 ml of stock media into 15 ml conical

ii. Add 1 μl/ml sodium pyruvate solution into conical

iii. Add 7.56 mg $NaHCO_3$

iv. Add 30 mg BSA

v. Dissolve added reagents by gently inverting conical up and down. Do not vortex

vi. Adjust pH to 7.2 - 7.4 with freshly prepared NaOH carefully

vii. Incubate in the water bath at 37°C

4. Harvest sperm cells

(a) Pipette 1 ml non-capacitating media into 1.5 ml centrifuge tube (for 1 mouse, 2 epididymides)

(b) Place harvest epididymides into the media and make 3-4 cuts. Incubate 10 min at 37°C to allow sperm swim out

(c) Remove the epididymides from the media

5. Prepare aliquots of sperm for fixation

(a) Non-capacitated sperm

i. Pipette 300 μl non-capacitating media into 1.5 ml centrifuge tube

ii. Pipette 100 μl of sperm into the tube

iii. Incubate at 37°C for 1 hour

(b) Capacitated sperm

i. Pipette 200 μl 2X capacitating media and 100 μl non-capacitating media into 1.5 ml centrifuge tube

ii. Pipette 100 μl of sperm into the tube

iii. Incubate at 37°C for 1 hour

A.3 Mice sperm fixation and staining

Centrifuge sperm at 1250 rpm (1k - 2k rpm) for 5 min. Avoid disturbing the pellet of cells and discard the supernatant. Pipette 600 μl pre-warmed Non-CAP media into each tube, then centrifuge again at same speed for another 5 min. Similarly, discard the supernatant without disturbing the pellet of cells. Add 100 200 μl pre-warmed Non-CAP media into the tube, resuspend cells by tapping the tube and follow the fixation protocols described as below.

A.3.1 Phalloidin staining

1. Add 50 μl sperm onto coverslip (poly-lysine coated coverslips are recommended), incubate 10 min for surface binding

2. Aspirate the media, fix and permeabilize the sperm using 100 μl of 0.3% glutaraldehyde (EMS, 16220) and 0.25% Triton X-100 in CB (10mM MES, 150mM NaCl, 5mM EGTA, 5mM Glucose and 5mM $MgCl_2$, pH 6.1)) for 1 - 2 min

3. Wash with CB 3 times for 5 min

4. Add 2% Glutaraldehyde in CB

5. Wash with CB 2 times for 10 min

6. Treat samples with 100 μl of 0.1% $NaBH_4$ (freshly prepared in PBS) for 7 min to reduce background fluorescence

7. Wash with PBS 2 times for 5 min

8. Prepare diluted Phalloidin staining solution right before use. Dilute 30 μl of the Alexa 647-Phalloidin stock solution into 400 μl PBS and apply proper amount to each coverslip

9. Place the stained samples in aluminum foil wrapped container to protect from light. Incubate at 4 °C for overnight

10. Briefly wash once with PBS, then mount the sample with imaging buffer

A.3.2 Immunostaining

1. Add 50 μl sperm onto coverslip (poly-lysine coated coverslips are recommended), incubate 10 min for surface binding
2. Aspirate the media, fix the cells with 100 μl of 4% PFA (EMS, 15710) in PBS for 10 min
3. Wash with PBS 3 times, each time allowing for 5 min incubation
4. Permeabilize the cells with 100 μl 0.5% Triton X-100 in PBS for 5 min
5. Wash with PBS 3 times, each time allowing for 5 min incubation
6. Add 3% BSA blocking buffer and incubate for 1 hour
7. Remove the blocking buffer and without washing, add 100 μl of primary antibody in 1% BSA (See Table A.3 for detailed concentration)
8. Place the samples in aluminum foil wrapped container to protect from light. Incubate overnight at 4 °C
9. Aspirate the solution and add 100 μl of secondary antibody in 1% BSA (Sigma, A7906, See Table A.3 for detailed concentration)
10. Incubate for 1 hour
11. Wash with 0.1% T-PBS 2 times, each time allowing for 5 min incubation, then mount the sample with imaging buffer

A.4 STORM imaging

For 3D STORM imaging, make sure that the MicAO system is turned on and mirror shape with astigmatism has been applied to the system.

Table A.3: Table of primary and secondary antibodies

Target	**Host Species**	**[Primary Antibody] in 1 % BSA**	**[Secondary Antibody] in 1 % BSA (Alexa-647 conjugated)**	**Vendor**	**Product No.**
Spectrin	Rabbit	1:25	1:1000	Sigma	s1515
Adducin	Rabbit	1:100	1:1000	Abcam	ab51130
PKAc	Mouse	1:200	1:500	BD	610980
FER	Mouse	1:50	1:500	Cell Signaling	4268
pY	Mouse	1:1000	1:1000	Millipore	05-321
Cdc42	Mouse	1:100	1:500	Santa Cruz	sc-8401
P-CaMKII	Rabbit	1:50	1:1000	Cell signaling	3361/12716
GLUT3	Rabbit	1:100	1:1000	Millipore	AB1344
AKAP4	Mouse	1:300	1:500	BD	611564
Tubulin	Mouse	1:100	1:1000	Hybridoma Bank	E7

1. Once the sperm samples are stained and ready to image, immediately mount the sample for STORM imaging with GLOX imaging buffer. GLOX imaging buffer preparation:

   (a) Prepare buffer A (10 mM Tris (pH 8.0) + 50 mM NaCl) and buffer B (50 mM Tris-HCI (pH 8.0) + 10 mM NaCl + 10 % Glucose)

   (b) Prepare Glox solution (250 μl):

      i. 14 mg Glucose Oxidase (Sigma, G2133) + 50 μl Catalase (17 mg/ml, Sigma, C40) + 200 μl Buffer A

      ii. Vortex to dissolve Glucose Oxidase

      iii. Spin down 14,000 rpm

      iv. Only use supernatant

      v. Store at 4°C for up to 2 weeks

      vi. In case of reusing, spin down at 14,000 rpm again

(c) On ice, mix 7 μl GLOX, 7μl β-mercaptoethanol (14.3M, Fisher Scientific, 60-24-2) and 690 μl Buffer B in a centrifuge tube, then take the appropriate amount to mount the sample

2. A continuous illumination of 638 nm laser, full power, is used to excite the Alexa Flour 647

3. if the density of blinking fluorophores is not adequate use violet laser, with ND2 usually, to excite more fluorophores

4. Collect 50,000 frames of images for each cell

A.5 3D STORM calibration

This calibration protocol is used to both MicAO optical optimization and Z LUT (lookup table) for 3D STORM imaging.

1. Dilute TetraSpeck beads (Thermo Fisher, T7279) with PBS at concentration 1:500 in 1.5 ml centrifuge tube

2. Perform 5 min sonication to the sample

3. Put parafilm on the bottom surface of a petri dish, then put the coverslip on top of the parafilm

4. After sonication, pipette all the beads solution onto the coverslip, incubate for another 5 min for surface binding without interruption

5. Aspirate the solution and briefly wash the surface once with PBS

6. Use forceps to grab the coverslip and put it on a glass slide, making sure that the sample side is facing towards slide. The coverslip should be placed at the center of the slide. Then mount it with nail polish until dried

7. Use red laser (647 nm, the same laser for STORM experiments) to excite the beads sample. In order to reduce the photobleaching effect on beads while maintaining relatively high SNR (signal to noise ratio), it is recommended to use ND 0.5 filter for laser power reduction

A.5.1 MicAO PSF optimization and astigmatism introduction

1. Open MicAO software (MicAO 3DSR, Imagine Optic), select local mode
2. Find a single isolated bead with imaging acquisition software (here we use Nikon Element), reduce the ROI (region of interest) to be 50X50 to include only one bead
3. Reduce the exposure time to 100 ms and set the gain to be a small value between 5 and 10
4. Make sure the images are saved as individual tiff file when start running the imaging protocol
5. Make sure a Macro called “Auto-capture.mac" (provided by the MicAO) is executed when imaging
6. Back to MicAO software, go to “Advanced setup"
7. In “Optimization” tab, set the delay to be 0.5 and in “Image & Z position" tab, set the directory to find tiff files as same as the images will be saved during timelapse acquisition
8. Start automatic timelapse capture
9. Click “Diagnostics manager" to visualize bead PSF
10. Click “optimization"
    (a) Keep search limit at 0.05
    (b) Select all 7 lower-order optical aberration correction options: Astigmatism at 0°; Astigmatism at 45°; Coma at 0°; Coma at 90°; D 3th order spherical aberration; Trefoil at 0°; Trefoil at 90°
11. Press the run button to initiate the optimization iteration process
    (a) There are two values “Initial contrast” and “contrast” determining the number of iterations of this process

(b) If the "Contrast" value $>$ "Initial contrast", accept the optimization correction by clicking the check button

(c) If the "Contrast" value $<$ "Initial contrast", click the cross button to reject the correction, then optimization finishes

12. Abort the timelapse acquisition. PSF optimization is done for 2D and save the mirror shape function

13. Click "open loop" in MicAO for introducing astigmatism and click run button to activate the panel function

14. In "Astigmatism at 0°" option, change the increment to "0.010", then set the astigmatism value at "0.060" to introduce 60 nm astigmatism.

15. Move piezo up and down to see if PSF with astigmatism looks good

(a) If the PSF is tilted, which means that there existing astigmatism at 45°, manually add/minus more "Astigmatism at 45°" to cancel out the tilting effect

(b) Similarly, if other aberrations exist, by playing with other correction options manually to improve the PSF

(c) A perfect PSF shows up a dark hole at a defocus of plus and minus 150 nm

(d) A perfect 60 nm PSF astigmatic PSF shall start splitting into two at $\pm$ 100nm of focus as shown in Fig. A.2

A.5.2 Z LUT acquisition

1. Enable the Z scanning feature of the imaging acquisition software (e.g. Nikon Element)

2. Enable the auto-scale so that the beads can be viewed

3. Find the focal plane of the sample with good density of beads around on the plane

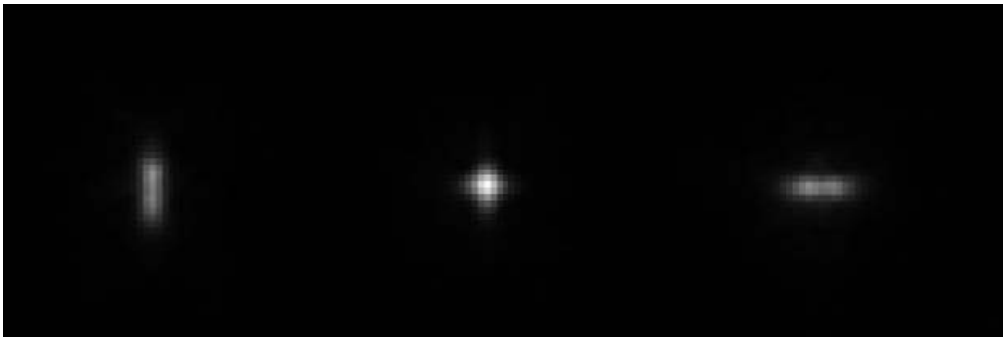

Figure A.2: Astigmatic PSF defocused by -100, 0 and 100 nm [37].

4. Set the exposure time to be 50 ms and the gain between 0 and 10

5. Set the Z scanning amplitude 2 μm with step size 10 nm, then initiate the Z scanning process. Make sure the scanning from one end to another end with the focal plane right in the middle (e.g. from -1 μm to 1 μm)

6. Repeat the scanning process after moving into a new region with good density of beads, until 6 - 10 movies are acquired

A.6 HeLa cell culture media and imaging saline

This protocol describes the methods for preparing both culture media and imaging saline for HeLa cells. All work should be performed inside the biosafety cabinet.

A.6.1 Preparing cell media

1. Heat shock 50 ml Aliquot of FBS. Let the FBS sit in water bath at 37°C for $\sim$ 1 hour after being thawed

2. Thaw antibiotic. Do not let thawed antibiotic remain unfrozen for an extended amount of time

3. Once FBS is thawed and heat shocked, add to DMEM

4. Pass DMEM + FBS + antibiotic solution through a bottle top filter into a sterile glass bottle

Table A.4: Materials of HeLa cell culture media

Material	Volume (ml)	Vendor	Product No.
FBS	50	Atlas Biologicals	EF-0500-A
DMEM (with phenol red)	500	Thermo Fisher Scientific	SH3002201
100X Antibiotic (Streptomycin/Penicillin)	50	Thermo Fisher Scientific	15140122
Sterile glass bottle	500	–	–
Bottle top filter	–	Life Science	CT-229717

5. Filter DMEM first, then add antibiotic. Add FBS at the end

6. Label bottle with description, initials and date

7. Store media in fridge

A.6.2 Splitting cells

Please take extreme care to be as clean and sterile as possible. Always make sure to warm all solutions in water bath at 37°C before beginning the procedure.

Table A.5: Materials for splitting HeLa cells

Material	Vendor	Product No.
Cell culture media	–	–
Trypsin	Thermo Fisher Scientific	25200114
Serological pipettes	–	–
35mm Delta T culture dish	Bioptechs	04200417B
100mm tissue culture dish	Life Science	CT-229620

1. A dish with confluent cells should be ready to split before running this protocol

2. Label new dishes with initials, date, cell type and amount of cells

3. UV all the culture dishes that cells will be split into for 30 min in the biosafety cabinet

4. Add 10 ml cell culture media from protocol A.6.1 into each new 100 mm dish
    (a) if live cell imaging is needed, also add 1 ml culture media into 35 mm Delta T dishes
5. Place all dishes in the incubator until ready
6. Aspirate media from dish with confluent cells
7. Pipette 4 ml of Trypsin into the dish, and put it back to the incubator for about 3 min
8. Once cells have lifted from bottom of dish, gentle tap the dish to help with cell lifting
9. Add another 6 ml culture media into the dish
10. Centrifuge at 200g speed for 2 min
11. Aspirate the supernatant and resuspend the cell pellet with 5 ml culture media
12. Pipette proper amount of cells into each new dish, then put them back in the incubator

A.6.3 HeLa cell imaging saline

HeLa imaging saline is a buffer that keep the pH stable for the cells. This way while imaging (without CO_2) the cells remain healthy.

1. Begin by measuring out $\sim$ 900 ml of Milli-Q water, since we need to adjust the osmolarity by adding water later
2. Add reagents with indicated amounts in Table A.6 to water, use a stir plate to keep the solution constantly mixing
3. Once everything is dissolved, check osmolarity of the solution. Add water until solution reaches 346 mOs
4. Check the pH of the solution. Adjust the pH to 7.4 by using HCl or NaOH
5. Pass the complete solution through a bottle top filter into a 1 L glass bottle
6. Store in fridge

Table A.6: Materials of HeLa cell imaging saline (1 L)

Material	Concentration (mM)	Amount (g)
NaCl	146	8.53
KCl	4.7	0.35
$CaCl_2 \cdot 2H_2O$	2.5	0.36
$MgSO_4$	0.6	0.072
NaH_2PO_4	0.15	0.02
Ascorbic acid	0.1	0.0176
Glucose	8	1.44
HEPES	20	4.76
Milli-Q water	–	–
NaOH	–	–
HCl	–	–
1L bottle top filter	–	–
1L sterile glass botte	–	–
Stir plate	–	–
pH meter	–	–
Osmolarity meter	–	–

A.7 HeLa cell beads loading, drug treatments and DNA staining

This protocol describes the beads loading technique to introduce QDs (Quantum dots) into the cell for observing the diffusive behavior during the mitosis process. The drug treatments include the usage of Nocodazole for mitosis metaphase synchronization and other actin inhibiting drugs as well as Nocodazole for cytoskeleton breakdown. DNA staining of the live HeLa cell is the key for better identification of cells in the metaphase.

A.7.1 Beads loading

1. Assemble the bead loader with the mesh woven filter and glass beads if needed, as shown in Fig. A.3

   (a) Push the glass of the glass bottom cell culture petri dish from inside out gently to remove it

Table A.7: Materials for beads loading

Material	Concentration	Vendor	Product No.
Glass beads	–	Sigma	G4649
Polypropylene Spectra Mesh Woven Filter	–	Spectrum laboratories	148496
Carboxylated QD655	3:10^4 in 1% BSA (Sigma, A7638) with PBS	Thermo Fisher Scientific	Q21321MP
35 mm cell culture petri dishes	–	–	–
Tape	–	–	–

(b) Tape all four sides of the filter to the outside of the dish (make sure there is no gap, which causes the leakage of glass beads)

(c) Pour some glass beads into the dish

(d) Put the lid of the dish upside down and on top of the dish

(e) Seal the lid and the dish with the tape

(f) Another dish lid is used for loader to rest on when not in use

* Keep the bead loader in the glass vacuum desiccator container when not in use

2. Aspirate the culture media out of the 35 mm Delta T dish, where HeLa cells are plated, as clean as possible

3. Pipette 4$\sim$8 μl of QDs onto the cells

4. Align the bead loader and dish together so that either of them is not tilted. Tap once lightly to ensure there is a monolayer of glass beads on top of the cells.

5. Tap the dish for 4-7 times from 4-5 cm high

6. Gently pipette the culture media into the dish. Incubate at 37°C for at least 45 min to let the cells recover

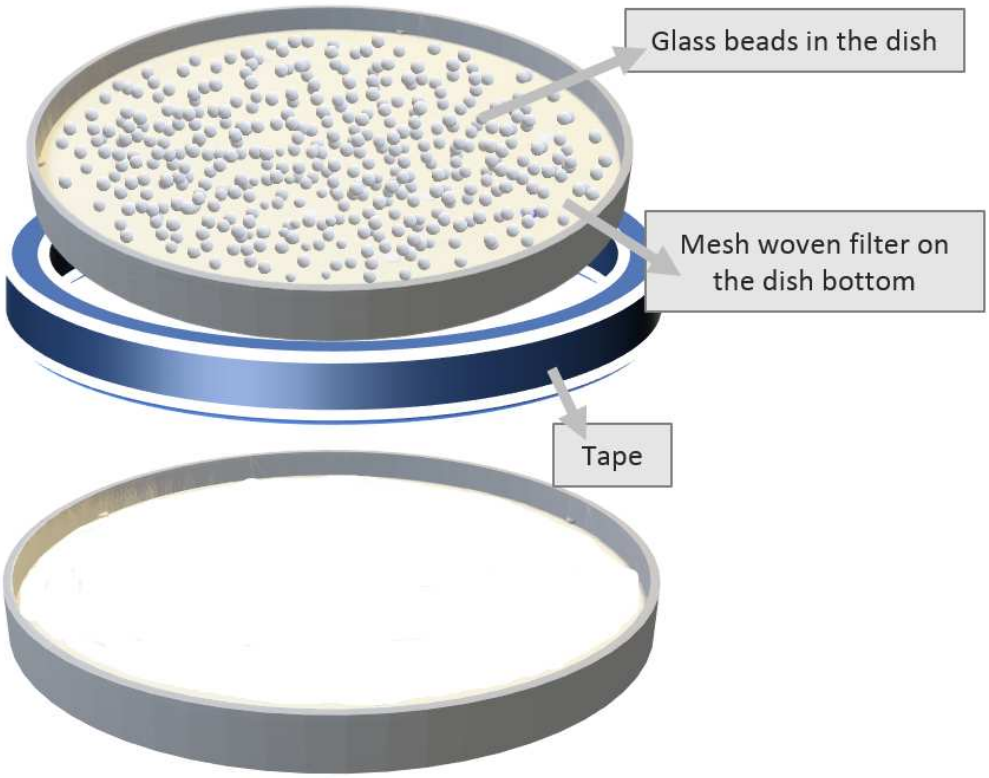

Figure A.3: Bead loader assembly.

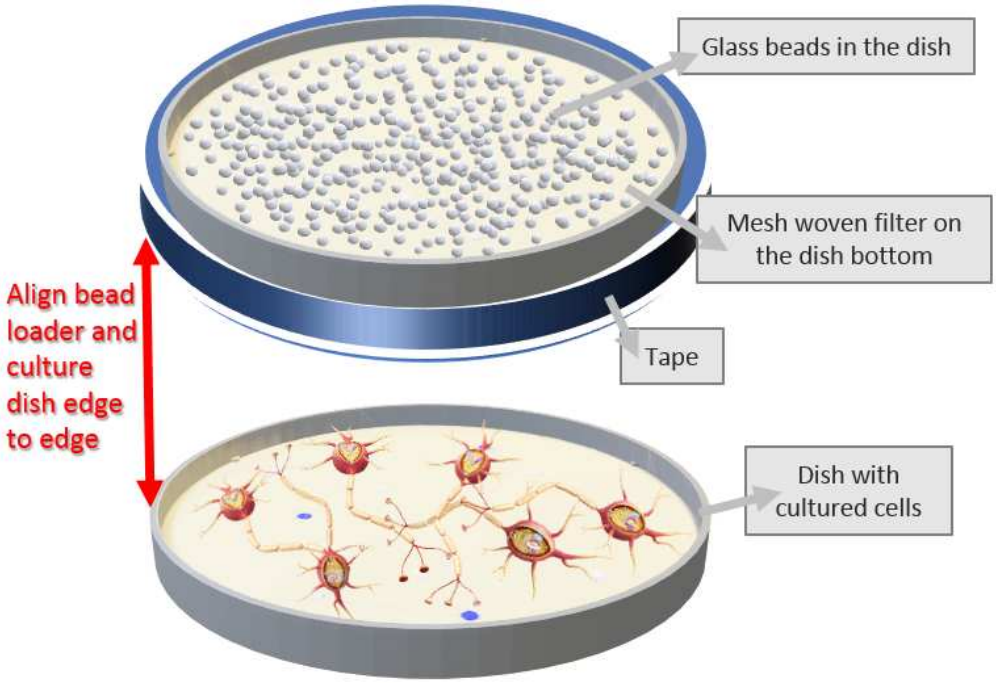

Figure A.4: Bead loader and dish alignment.

7. Aspirate the media after incubation. Wash away the extracellular unimported QDs gently with PBS for 1-2 times. Then switch to the imaging saline for further imaging

A.7.2 Drug treatments and DNA staining

1. Mitosis metaphase synchronization in HeLa cells

   (a) Prepare a stock of 3 μg/ml of Nocodazole (Sigma, M1404) in DMSO

   (b) Add 5 μl of Nocodazole stock solution into the 1 ml cell culture media and vortex

   (c) Replace this mixed media with the media in the chosen dish with HeLa cells

   (d) Incubate at 37°C overnight for synchronization. The incubation time should be between 12-18 hours

   (e) Before imaging, the synchronization media with Nocodazole should be removed and fill the dish with normal culture media to incubate at 37° for another 30-45 min recovery

2. Cytoskeleton breakdown in HeLa cells

   - Prepare 0.2 μM Latrunculin A with cell culture media, then add it to the cells for 30 min incubation at 37°C
   - Prepare 2 μM Cytochalasin D with cell culture media, then add it to the cells for 30 min incubation at 37°C
   - Prepare 10 μM Nocodazole with cell culture media, then add it to the cells for 10 min incubation on ice first, followed by 15 min incubation at 37°C

3. DNA staining in HeLa cells

   - Prepare 5-10 μg/ml Hoechst 33342 with cell culture media. Add it to the cells for 30 min incubation at 37°C

A.8 HeLa cell maintenance

There are two major parts for hela cell line maintenance: freezing cells and thaw cells.

A.8.1 Freeze Hela cells

1. Make sure two cell culture dishes with at least 90% confluent HeLa cells are ready for freezing
2. Prepare 5 ml freezing medium, containing 90% FBS and 10% DMSO
3. Prepare three 1.5 ml sterile centrifuge tubes
4. Either use cell scrapers or Trypsin (same method as in protocol "Splitting cells") to remove cells from the culture dish surface. Then pipette them all into the 10 ml centrifuge tube
5. Centrifuge at 200g speed for 2 min
6. Aspirate the supernatant and resuspend the cell pellets with 3 ml of freezing medium as mentioned above
7. Split into three centrifuge tubes, then store at -80°C

A.8.2 Thaw Hela cells

1. Remove one tube of the HeLa cell stock from -80°C freezer and put it in the 37°C water bath for rapid thawing
2. Take the tube out of the water bath just before the last bit of frozen medium thaws
3. Once it's completely thawed at the room temperature, pipette 100 μl of cells into a culture dish with 10 ml pre-warmed HeLa cell culture medium
4. Let the cells attach for overnight in the incubator.
5. If necessary, the next day, the medium in the culture dish can be replaced with fresh culture medium to get rid of the DMSO residue

A.9 Reproducing fractional Brownian motion

This protocol describes how to use the agarose gel to reproduce the fractional Brownian motion. The quality of agarose powder is critical in this experiment. Usually, agarose gelling temperature is below 37°C, which means above this temperature, the agarose solution should still remain liquid form. If the gelling temperature is 37°C according to datasheet, but the agarose starts gelling at 42°C, then a new batch of agarose powder should be used instead.

Table A.8: Materials for reproducing fractional Brownian motion

Material	Concentration	Vendor	Product No.
Agarose	1% or 1.5% in PBS	Apex BioResearch	20-102GP
PBS	0.01 M	–	–
Carboxylated polystyrene microspheres	1:10 (final, in agarose)	Bangs Laboratories	PC02N/13136
0.5% Tween20	1:12 (final, in agarose)	–	–

1. Measure agarose powder and pour it into a 50 ml conical, then add PBS. Loosely seal the conical with cap and put it into a beaker filled with water. The water level should be higher than the PBS level inside the conical to prevent burning

2. Put the beaker and conical in the microwave. Microwave for 2-3 min until the agarose dissolve completely.

    * It is suggested to microwave for a short time period, stop and swirl, and then continue towards a boil

3. Take out $>$ 1 ml of agarose solution into a pre-heated 1.5 ml centrifuge tube, leave it in a heating stage for 60 min incubation at 60°C

4. Leave the rest of agarose solution with water filled beaker on a hot plate heater, maintaining the water temperature around 60°C for future use

5. Mix beads solution and 0.5% Tween20 in a centrifuge tube. Pre-heat the beads mixture for at least 3 min at 60°C to prevent local gelling when adding cold beads solution into agarose solution

6. Measure agarose solution from 60min-incubated 1 ml agarose solution, then mix it with beads mixture in a new centrifuge tube. Gently tap the tube and leave it inside the heater for another 15 min for better mixing

7. Meanwhile, prepare a piece of aluminum foil and petri dish. Leave the aluminum foil on the heater with petri dish on top of the foil. Quickly add the beads/agarose mixture into the petri dish after 15 min incubation. Then wrap the dish with the aluminum foil. Take them off the heater and wait for gel formation

8. After gel forms, unwrap the foil and study the sample on a microscope

Appendix B

Software

This appendix provides protocols used for the data analysis presented in this thesis, including STORM reconstruction, localization analysis and particle tracking.

B.1 3D STORM Z calibration LUT generation

STORM LUT generation and reconstruction are done in imageJ/Fiji. Fiji is recommended to use due to more flexible and advanced features. The experiment movies are usually saved as nd2 files from Nikon Element software, which can be imported into Fiji through Bio-Formats plugin.

1. Install ThunderSTORM plugin if needed (*http://zitmen.github.io/thunderstorm/*)
2. Load the calibration movie acquired from protocol A.5.2 into the Fiji, but only from frame 30 to frame 170
3. Click the "3D Calibration $\rightarrow$ Cylindrical lens calibration" from "ThunderSTORM" plugin
4. Change the parameters
   (a) Camera setup: For our system (Krapf Lab, TIRF setup with 100X objective)
      i. Pixel size [nm]: 130
      ii. Photoelectrons per A/D count: 16.23773
      iii. Base level [A/D counts]: 6.437
      iv. EM gain: Gain value used during calibration experiment
   (b) Image filtering: Keep the default (Wavelet filter with B-spline order 3 and scale 2.0)
   (c) Approximate localization of molecules
      i. Method: Local maximum
      ii. Peak intensity threshold: 1$\cdot$ std(Wave.F1)

* *The peak intensity can be adjusted to number·std(Wave.F1),*
  for example: 2·std(Wave.F1) to ensure only real bead signals are detected not the background noise

iii. Connectivity: 8-neighbourhood

(d) Sub-pixel localization of molecules

i. Method: Elliptic Gaussian w/angle

ii. Fitting radius [px]: 6

iii. Fitting method: Least squares

iv. Initial sigma [px]: 0.93

* *The fitting radius should be adjusted based on different degree of introduced astigmatism. The initial sigma value can be calculated by*
  sigma[px] = $\frac{0.25\lambda_{emission}}{NA \cdot Pixel\ size}$

(e) 3D defocusing options: ThunderSTORM

(f) Additional options:

i. Z stage step [nm]: 10

ii. Z range limit [nm]: 550

5. Run the calibration. Repeat the steps until the best calibration curve is found through all the collected movies and save the calibration as txt file.

B.2 3D STORM reconstruction

1. Install ThunderSTORM plugin if needed (*http://zitmen.github.io/thunderstorm/*)
2. Open the STORM movies in imageJ/Fiji
3. open the ThunderSTORM plugin (Plugins→ThunderSTORM→Run Analysis)
4. Click “Camera setup” at the top of “Run Analysis”, and choose the correct EM Gain for the analysis

5. In the “Run Analysis” tab, make sure the correct parameters are chosen

   (a) Wavelet filter is recommended with order 3 and scale 2. âĂIJGaussianâĂİ is chosen for sub-pixel localization of molecules. For connectivity 8-neighbourhood is recommended

   (b) 3D box is checked if running 3D reconstruction. Colorized z-stack box is checked if colorized reconstructed image with color-coded z height is preferred

   (c) Z range: The value here is only for visualization preview. Range from -500 nm to 500 nm is a good start. Step size is based on the pixel size and magnification. If pixel size is 130 nm and magnification shown in the graph is 10, then the step is 130 nm/10 = 13 nm

   (d) Calibration file: Be sure that 3D calibration file is ready before running reconstructions. Choose the appropriate calibration file for corresponding movies

6. After all of the Run Analysis settings are configured, hit OK at the bottom to start reconstruction. (Depending on RAM usage, this could take anywhere from 20 to 40 minutes)

7. After the initial reconstruction is finished, a results table should appear with options at the bottom. These are settings that are used in post processing, and some will be utilized. Before any post processing is done, “Export” the original data table to the desired folder.

   * File format: XLS (tab separated) but with .txt extension

8. The first step in post processing is to “remove duplicates” from the data. The distance threshold that is used is “uncertainty”

9. If a 3D reconstruction is being processed, the next step is to filter out the images that have too less localizations to the final 3D reconstruction and are not within the calibration accuracy region, otherwise skip this step

(a) Use the visualization with “Auto size by results’ to check the current reconstruction. By sliding the progress bar of image stacks, the reconstruction at each height can be viewed. This helps to eliminate the unwanted height information

(b) Use the command "z>lower bound & z<upper bound" for z filtering

(c) Consider the calibration accuracy (normally is around the range -550 nm to 550 nm) and the localization density of the reconstruction after coarse z filtering, refine the values of filtering bounds and re-filter the results to get better reconstruction.

10. Then drift correction, which is under the “Drift Correction” tab

(a) When correcting the drift, either “Cross correlation” or “Fiducial marker” method is used. “Cross correlation” if there are no fidicual markers in the movie and âĂIJFiducial markersâĂİ if you have

(b) With cross correlation selected, select “>>” just to the right, and a tab will appear. This is used to select the number of bins for drift correction and the magnification used in reconstruction. Hit “Apply” and observe the change of the preview of reconstruction which displays automatically after the drift correction. Sometimes, there are some artifacts occur even though you have right drift curve. In that case, then try other bin values, otherwise avoid any drift correction

(c) With fiducial markers method selected, select “>>” just to the right, and a tab will appear. “Max distance” controls the lateral tolerance for identification of a marker. “Min marker visibility ratio” controls the fraction of frames wherein the molecule must be detected to be considered as a fiducial marker. “Trajectory smoothing factor” controls smoothness of the drift trajectory. Typical values for these three parameters are 50, 0.1, 0.25 separately

11. The final post processing step is to merge the data. This is simply done by hitting the “Merge” tab and selecting Merge

12. Now, export this post-processed results table. The nomenclature for this second export is "result_z from *filter lower bound* to *filter upper bound_Number of bins* bins_RFDM" or "result_z from *filter lower bound* to *filter upper bound*_fiducial marker_RFDM"

    * RFDM stands for (R)emove duplicates, (F)ilter, (D)rift correct, (M)erge if applicable
    * File format: XLS (tab separated) but with .txt extension

13. After the second export, hit "Visualization" on the bottom of your post-processed results table

14. Save the image

    - For 2D reconstruction, just save the tiff image produced by "Visualization"
    - For 3D reconstruction
        i. Make sure "3D" and "Colorized z stack" are selected before running the visualization
        ii. Save the generated stack of tiff images first
        iii. Change the units in the image properties if necessary.
        iv. Change the format of images to RGB (Image→Type→RGB)
        v. Create a single frame super-resolution image by overlaying stacks of images (Image→Stacks→Z Project→Projection type: Sum Slices)

15. 3D Cross section images generation (optional)

    (a) Select a ROI for viewing the cross sections or use the entire window
    (b) Then choose "Image→Stacks→Reslice". Select the preferred scanning direction, usually "Start at Left", click Ok to run the reslice
    (c) save the newly generated stack of cross section view images

16. 3D rotation (optional)

- Load the stacks of images from 3D reconstruction, and open the “plugin→3D Viewer” (cross section view stacks usually give better 3D rotation movie)

B.3 3D STORM localization analysis

This protocol describes the radial and angular distribution analysis used in this thesis for signaling proteins in sperm capacitation process. For actin structure in midpiece, power spectrum analysis is applied as well. Generally, a ROI within the localizations that lie in a straight line would be chosen for analysis.

B.3.1 Radial and angular distribution analysis

1. Localize the ROI for analysis

   (a) Import the results table from 3D reconstruction into the imageJ/Fiji through ThunderSTORM plugin (ThunderSTORM→Import/Export→Import Results)

   (b) Visualization

      i. Click the “Auto size by results”, focus on the values of the starting visualization points: left top x and left top y, as well as width and height

      ii. Set the left top x and y values to be 0, change the width and height accordingly: new width = old width + old left top x; new height = old height + old left top y

      iii. Convert the unit of length from μm to nm in the image properties

      iv. Locate a desired ROI where the localizations lie straight

   (c) Use “straight line" function in the ImageJ/Fiji to draw a line along with the orientation of the ROI. The rotation angle between the ROI and the horizontal line can be read from the ImageJ/Fiji task bar when drawing the line

   (d) Put the cursor close to the beginning and ending point of ROI to read the starting point (x_1, y_1) and ending point (x_2, y_2)

(e) Use the bounds (x_1, x_2) and (y_1, y_2) to crop the ROI in the similar way as in z filtering: $x>x_1 \& x<x_2$ and $y>y_1 \& y<y_2$

(f) Save the updated cropped results table

* File format: XLS (tab separated) but with .txt extension

2. Rotate the cropped ROI:

MATLAB code: Rotate_results_table_from_ThunderSTORM_Shift_XY_to_positive.m

```
%REMOVE THE HEADERLINES OF STRING FROM RESULTS TABLE
%OPTION1 TAP SEPARATED
filename = 'result 4 times_z from -169 to 611_25 bins_RFDM_x
from 47203 to 52234 and y from 12311 to 15275.txt';
delimiterIn = '\t';
headerlinesIn = 1;
M = importdata(filename,delimiterIn,headerlinesIn);
A = M.data;
%SET ROTATION MATRIX
R_ang = 18.89;
R_ang_rad = ((R_ang)/180)*pi;
R = [cos(R_ang_rad), -sin(R_ang_rad); sin(R_ang_rad),
cos(R_ang_rad)];
%CONVERT(X,Y) TO (X',Y') THROUGH MULTIPLYING ROTATION MATRIX
XY = (A(:,3:4)).'; % Read column of x and y, and transpose
R_XY = (R*XY).'; % Apply rotation matrix multiplication.
R_A = A;
R_A(:,3:4) = R_XY; % Replace with rotated x and y.
%SHIFT X TO POSITIVE VALUE
minX = min(R_A(:,3));
if (minX < 0)
```

```
22          R_A(:,3) = R_A(:,3)-minX;
23  else
24  end
25  %SHIFT Y TO POSITIVE VALUE
26  minY = min(R_A(:,4));
27  if (minY < 0)
28          R_A(:,4) = R_A(:,4)-minY;
29  else
30  end
31  %ADD HEADERLINE
32  fid = fopen('Rotated results_MP.txt', 'w');
33  fprintf(fid,'%2s\t%5s\t%6s\t%6s\t%6s\t%12s\t%12s\t%12s\t%12s\
        t%12s\t%12s\t%12s\t%12s\n','id','frame','x [nm]','y [nm
        ]','z [nm]','sigma1 [nm]','sigma2 [nm]','intensity [photon
        ]','offset [photon]','bkgstd [photon]','chi2','uncertainty
         [nm]','detections');
34  fprintf(fid,'%f\t%f\t%f\t%f\t%f\t%f\t%f\t%f\t%f\t%f\t%f\t%f\t
        %u\n',R_A');
35  fclose(fid);
36  clear
```

(a) filename = name of updated cropped results table

(b) R_ang = rotation angle from above

(c) After running the code, the rotated result will be automatically saved as "Rotated results.txt"

3. Minimize the ROI

(a) Import the rotated results table into the ImageJ/Fiji

(b) Visualize the rotated images, Set the left top x and y values to be 0, change the width and height accordingly: new width = old width + old left top x; new height = old height + old left top y

(c) Convert the unit of length from μm to nm in the image properties

(d) Zoom in the visualization images with ROI centered

(e) Use "rectangular selection' function" to draw a rectangle tightly around the ROI in order to manually eliminate outside noise as much as possible

(f) Read the boundary of the rectangle (x_1, y_1) and (x_2, y_2)

(g) Crop the results table again for ROI minimization

(h) Save the updated results table

* File format: XLS (tab separated) but with .txt extension

4. Check the Y-Z cross section shape

(a) Import the minimized ROI results table

(b) Visualize with "Auto size by results"

(c) Convert the unit of length from μm to nm in the image properties

(d) Reslice the visualization to see the Y-Z cross section

i. select the entire window

ii. Image→Stacks→Reslice

(e) Sum stacks of resliced visualization images (Image→Stacks→Z projection)

(f) Check the shape of the Y-Z cross section overlaid image

- If it is a complete circular shape or elliptical shape, go to step (5)

- otherwise, go to step (6)

5. Find the center of Y and Z (Gaussian Peak Fitting)

   (a) Import the results table from step (3) into OriginLab

   (b) Right click on the column "y [nm]', choose "Frequency count", set bin size to 5 to run

   (c) in the new window including the count data, choose the column "Counts (Y)" and click the "Scatter" plotting function

   (d) If a single peak plot is shown

      i. Analysis→Fitting→Nonlinear Curve Fit→ Open Dialog→Category: Peak Functions→Function: GaussAmp

      ii. Click "1 iteration' a few times, then click "Fit until converged"'

      iii. Click "Fit" and read the xc value, which is the center of Y

   (e) If multiple peaks are shown

      i. Analysis→Peaks and Baseline→Multiple Peak Fit→Open Dialog →Peak Function: Gauss

      ii. Follow the instructions to pick peaks, then click "Open the NLFit'

      iii. Click "1 iteration" a few times, then click "Fit until converged"

      iv. Click "Fit" and read the multiple xc values, calculate the average xc value, which is the center of Y

   (f) Repeat step (b)-(e) for column "Z [nm]" to find the center of Z

6. Find the center of Y and Z (Circular Fitting)

   (a) Import the results table from step (3) into ImageJ/Fiji

   (b) Visualize the ROI images with the left top x and y set to be 0 as well as modified width and height as explained before

   (c) Convert the image type to 8 bit

   (d) Convert the unit of length from μm to nm

(e) Reslice the visualization images for the entire window

(f) Sum stacks of resliced visualization images

(g) Save this single image as tiff file

(h) MATLAB code: Singlecirclefit_for_averaged_resliced_images.m

```
%%The intensity value in the images should be larger than
    1. If not, convert to 8 bit.
%% Read in images
I = imread('SUM_Reslice of Averaged_MP.tif');
thr=1;          %threshold value
[xt,yt]=find(I>=thr);

A=zeros(size(xt));
for i=1:size(xt)
    A(i)=I(xt(i),yt(i));  %intensities
end

tot=sum(A);
cc=cumsum(A);
z=zeros(tot,1);
y=zeros(tot,1);

temp=1;
for i=1:size(xt)
    z(temp:cc(i))=xt(i);
    y(temp:cc(i))=yt(i);
    temp=cc(i)+1;
end
```

```
[zc,yc,R] = circfit(z,y);
```

(i) Run the code then fitted center values of Y and Z in pixel can be read. Multiply values by pixel size. For fitted center value of z, shift the value for a distance of lower bound of visualization images to get the real center value of z

* *e.g. fitted center value of z is 100 nm from the code, but the stack of visualization images is from -500 nm to 200 nm. Then the actual center value of z is 100 nm + (-500 nm) = -400 nm*

7. Transform results table in Cartesian coordinate to cylindrical coordinate

MATLAB code: Angular_and_Radial_distribution_with_circlefit_center.m

```
% HAVE CENTER VALUE OF Y AND Z READY BEFORE USING THIS CODE
% LOAD ROI RESULT TABLE
filename = 'Rotated results_MP_x from 41236 to 44005 and y
from 28847 to 29653.txt';
delimiterIn = '\t';
headerlinesIn = 1;
M = importdata(filename,delimiterIn,headerlinesIn);
A = M.data;
[n,m] = size(A); % n = row, m = column
X = A(:,3);
Y = A(:,4);
Z = A(:,5);
yc1 = 29251.3; % center of y
zc1 = 191.6603; % center of z

Y1 = Y - yc1;
Z1 = Z - zc1;
```

```
18
19 [theta1 ,r1] = cart2pol(Y1,Z1);
20
21 theta1_ang = (theta1./pi).*180;
22
23 B(:,1) = r1;
24 B(:,2) = theta1_ang;
25 dlmwrite('radial and angular result with circle fit_MP.txt',
26 B,'\t');
27
28 clear
```

8. Radial and angular distribution

   (a) Import the results from step (7) into OriginLab

      i. Column 1: radius

      ii. Column 2: angles

   (b) Find the frequency count as did in step (5)(b) to both columns

   (c) In the new window of frequency count of radius, add another column, set column values with expression "$\frac{\text{Col("Count")}}{2\pi\text{Col("Bin Center")}\cdot\text{Bin size}\cdot\text{Total Counts}}$", which gives the probability density and then plot the distribution with "Line" function

   (d) In the new window of frequency count of angles, add another column, set column values with expression "$\frac{\text{Col("Count")}}{\text{Bin size}\cdot\text{Total Counts}}$", which gives the probability density and then plot the distribution with "Line" function

B.3.2 Power spectrum analysis

A periodic structure of actin in the midpiece of mouse sperm has been observed. We use power spectrum analysis to extract the periodicity of this pattern of actin.

1. Generate 2D histogram data

   (a) Both the results table from step (3) and step (7) in section B.3.1 are required

   (b) Compose a new data table, including a column of displacement "x [nm]" from step (3) and a second column of angle "theta" from step (7)

   (c) Select both columns:
   Statistics→Descriptive Statistics→2D Frequency Count/Binning→Open Dialog

   (d) Parameters:

   - Bin size: The same bin size will be used as the "Time interval" when plotting power spectrum. e.g. 20-100, values vary for different cases
   - Minimum Bin Beginning: Check the "Auto" box
   - Maximum Bin End: Check the "Auto" box
   - When checked, "Image Plot" can be checked to view the 2D distribution plot

   (e) Save 2D histogram data as txt file

2. Average power spectrum

   (a) LabVIEW code: PowerSpectrum all columns.vi
   Path: Eric1:\STORM\Analysis\PowerSpectrum all columns.vi

   (b) Parameters

   i. Input: 2D histogram data from step (1)

   ii. Window: Hanning

   iii. Time interval: Bin size of x from step (1)

   (c) Save the power spectrums for all columns as txt file

   (d) Import this txt file into OriginLab

   (e) Statistics→Descriptive Statistics→Statistics on Rows→Open Dialog

   (f) select the data range for averaging

(g) Plot the averaged power spectrum in log-log scale

B.4 Particle tracking using TrackMate

This protocol is used to track the diffusion of QDs in the HeLa cells.

1. Load images into Fiji
2. Select a region without cells, calculate background from this region
3. Subtracted calculated background from the whole image
4. Calculate mean Delta t (lag time) from meta files
5. Enhance contract (Process→Enhance contrast) if necessary
6. Apply Gaussian Blur (Process→Filters→Gaussian Blur) if necessary, typical value: 1.2
7. Open TrackMate (Plugins→Tracking→TrackMate)
8. Select Laplacian of Gaussian detector
9. Estimated blob diameter = 4 pixels. Threshold = 200, which can be adjusted until the preview of localizations looks good. Select the median filter and sub-pixel localization
10. Hit next until the simple LAP tracker, which is used for best results
11. Set the linking max distance, gap-closing max distance and gap closing max frame all to be 2, this can be changed from case to case
12. Set filters on tracks. Select all tracks with N$\geq$50, number of gaps$\leq$5. Discard corrupted tracks, discard tracks that are close to the borders because of tracking errors
13. Analysis→ save track statistics
14. Export tracks as XML file, then convert via MATLAB

Appendix C

Additional publications

This appendix lists additional publications that are not included in this thesis.

C.1 Additional publications

1. Krapf, D., Marinari, E., Metzler, R., Oshanin, G., Xu, X. and Squarcini, A., "Power spectral density of a single Brownian trajectory: what one can and cannot learn from it". *New Journal of Physics*, 20(2), p.023029, 2018.

2. Krapf, D., Lukat, N., Marinari, E., Metzler, R., Oshanin, G., Selhuber-Unkel, C., Squarcini, A., Stadler, L., Weiss, M. and Xu, X., "Spectral content of a single non-Brownian trajectory". *Physical Review X*, 9(1), p.011019, 2019.